SIMULATION AND THEORETICAL STUDY OF SWIMMING AND RESISTIVE FORCES WITHIN GRANULAR MEDIA

A Thesis
Presented to
The Academic Faculty

by

Yang Ding

In Partial Fulfillment
of the Requirements for the Degree
Doctor of Philosophy in the
School of Physics

Georgia Institute of Technology
December 2011

SIMULATION AND THEORETICAL STUDY OF SWIMMING AND RESISTIVE FORCES WITHIN GRANULAR MEDIA

Approved by:

Dr. Daniel I. Goldman, Advisor
School of Physics
Georgia Institute of Technology

Dr. Harold Kim
School of Physics
Georgia Institute of Technology

Dr. Kurt Wiesenfeld
School of Physics
Georgia Institute of Technology

Dr. Predrag Cvitanović
school of Physics
Georgia Institute of Technology

Dr. David Hu
School of Mechanical Engineering
Georgia Institute of Technology

Date Approved: 31st October 2011

To my parents and wife, who always support me

ACKNOWLEDGEMENTS

TABLE OF CONTENTS

LIST OF TABLES

LIST OF FIGURES

SUMMARY

One way to investigate the physics of a medium is to study the forces on intruders moving through the media. A special case of intruders moving in media is the locomotion of organisms. Locomotion within fluids (flying in air and swimming in water) has been extensively studied and the complexity of interaction between intruders and fluids is well recognized. Locomotion within yielding substrates like sand, soil and debris that display both solid and fluid-like behavior has been less studied and is therefore less understood than to locomotion within fluids or on solid ground. In such materials, validated theories for describing the flow and resistive forces on intruders have not reached the levels of those for fluids.

As a representative case of subsurface locomotion in granular media, we study on the undulatory sand-swimming of the sandfish lizard (*Scincus scincus*), a small (~ 10 cm) desert-dwelling lizard. We use numerical simulations and theoretical models of the interactions between granular media and simple objects, biological and robotic systems to reveal principles of undulatory locomotion in granular media. We also use the models to investigate the resistive forces on intruders with different orientations and shapes, which is essential for the understanding of locomotion ability and performance of locomotors. Previous experimental work using high speed x-ray imaging showed that the sandfish lizard swims within dry granular media without limb use by propagating a single period traveling sinusoidal wave along its body. The wave efficiency η, the ratio of the forward speed to the traveling wave speed, was approximately 0.5, independent of the packing state of the media (close and loose). To explain these results, we develop a resistive force model with empirical force laws to explain the swimming speed observed in the animal experiment. We show that the higher wave efficiency reached by the sandfish compared to the low Re swimmers (~ 0.2) was because of the different functional form of the resistive forces on a rod dragged in granular media. We vary the ratio of undulation amplitude (A) to wavelength (λ) and demonstrate that an

optimal waveform $A/\lambda \approx 0.2$ for sand-swimming exists, which results from the competition between η and λ. To test assumptions in RFT and to study more detailed mechanics of sand-swimming, we developed a numerical model of the sandfish coupled to a discrete element method simulation of the granular medium. The numerical model confirmed that inertial forces are negligible and that the forces on the animal can be approximated by the forces on rods dragged at constant speed in granular media. The wave efficiency predicted by simulation qualitatively matched both the RFT model and the prediction of the optimal A/λ; However, the simulation revealed that the RFT over predicted the swimming speed because the reduction in magnitude of the resistive forces during velocity reversal was not considered. The RFT model and simulation helped the development of a sand-swimming robot, and the robot verified predictions from the RFT model and the simulation, such as the value of the wave efficiency, the actuator torque, and the effect of varying kinematic parameters including A/λ and number of periods. Inspired by the shovel-shaped head of the sandfish lizard, we studied the drag induced lift in granular media. We found that when a submerged intruder moves at a constant speed within a granular medium it experiences a lift force whose sign and magnitude depend on the intruder shape. We demonstrated that the lift forces and hence vertical position of the sand-swimming robot as it moves forward within granular media can be controlled by varying its head shape. The models together with robots explained biological observations of the kinematics of the animal and provide a hypothesis for the morphological adaptation (head shape) of the animal as well as guidance for building biophysically inspired robot that could explore challenging environments. The principles learned about the resistive forces can also help the design of the other machines that interact with granular media. My studies have given new insights into localized intrusion of simple and complex/composite shapes in granular media.

CHAPTER I

INTRODUCTION

Granular media, collections of macroscopic particles, are common in natural environments (Fig. 1). Sand, an example of a granular medium, covers 6-10% of land surface [41] on earth and most of the surface of several solid celestial objects [14, 56, 89]. Many everyday foods, such as rice and sugar, are in the form of granular media. Granular media also play important roles in many industries; it is the second-most manipulated material in industry (according to [102]).

One way to investigate the physics of a medium is to study the forces on intruders moving through the media. A special case of intruders moving in media is locomotion of organisms [4]. Animal locomotion, including running, swimming, flying, is the result of the interactions between multiple degree of freedom musculo-skeletal systems of organisms and the external media (Fig. 2). Locomotion often plays an key role in some tasks that are essential for the survival of the animal, such as finding foods or mates, migrating and escaping predators. To accomplish each of these tasks, different qualities of locomotion may be required, such as maximal speed, acceleration, stability and energetic efficiency. To move in a medium or on the interface of media, animals manipulate the reaction forces such as thrust, drag or lift to propel themselves as well as to overcome the gravity in many cases. To generate the forces required to move in diverse media and on various surfaces,

Figure 1: Examples of granular media. A: Martian sand. B: Soil. C: Coffee beans.

Figure 2: Animal locomotion in various media. A: Whales swimming in water. B: A bird flying in the air. C: An earthworm moving in soil.

specialized structures on bodies and appendages are involved in creating favorable physical interactions over a range of length scales. For example, billions of hairs on the feet of gecko lizards allow adhesion to smooth surfaces through van der Waals interactions [119], while the legs of water striders generate specialized vortices to propel themselves forward [60].

To discover principles of locomotion, an integrative approach, which include animal experiments [37, 91, 55, 43], theoretical modeling [12, 58, 77], numerical modeling [88, 111, 39], and robotic approaches [26, 68, 74, 40], is often required. Such studies have produced understandings of locomotion biomechanics in a range of terrestrial, aquatic, and aerial environments [13, 123, 5, 23] as well as improved understanding of the physics of the media (e.g. [78, 30, 9]). Such insights may lead to biologically inspired robots that can locomote in the real world with desirable properties of biological organisms, such as adaptivity, robustness, versatility, and agility [98]. Locomotion performance of robots can be improved with bio-inspired design and possibly outperform the animal(s) that inspired the design because of the absence of some anatomical and physiological limitations[116].

1.1 Background of sand-swimming

1.1.1 Locomotion in fluids and in granular media

Locomotion within fluids (flying in air and swimming in water) has been extensively studied, and the complexity in interaction with the fluid is well recognized [123]. Because the fundamental constitutive equations for fluids (i.e. the Navier-Stokes equations) are available, in principle the thrust or lift in such fluids can be determined by solving the constitutive

equations with moving and deforming boundaries. Since buoyancy in air is usually is insufficient to overcome gravitational forces on animals and man-made vehicles, lift forces from the air are often generated by wings or wing-like structures. Understanding of how shape and the orientation of intruders moving at constant speed affect the lift and drag forces are essential in designs of airfoils. For insects who fly by flapping wings, shape deformation of wings and leading edge vortex are important in thrust and lift generation [112]. Vortices also play key roles in locomotion in water at high Reynolds (Re), ranging from undulatory swimming of fishes to water jetting of jellyfishes [72, 27]. Measurements of flows in fluids are facilitated by visualization techniques such as particle image velocimetry (PIV) (e.g. [72]). Locomotion within yielding substrates like sand, soil and debris that display both solid and fluid-like behavior has been less studied and is less understood compared to locomotion within fluid or on solid ground [4, 111, 81, 34, 54, 94]. In such materials, validated theory at the level of fluids does not exist, and visualization techniques like PIV are nearly non-existent.

Subsurface locomotion is particularly relevant to desert organisms like scorpions, snakes and lizards. Because vegetation is sparse in deserts, animals need to escape heat or predators, or hunt for prey [7, 124]. Studying subsurface locomotion of organisms may also lead to discoveries about their environment because locomotion can change the states of the physical, chemical, and microbiological properties of the media in which they live. This is known as bioturbation [87, 28]. Because the media animals burrow into are opaque, most studies that describe the behavior of burrowing animals have relied on direct observation of above surface locomotion [90, 7]. Due to the lack of detailed subsurface observations, previous models of locomotion in granular media were largely based on speculated mechanisms (e.g. [111]). Recently, the visualization of subsurface locomotion has become possible due to advances in, and the affordability of, high speed nuclear magnetic resonance (NMR) and X-ray imaging technologies [81, 10, 45].
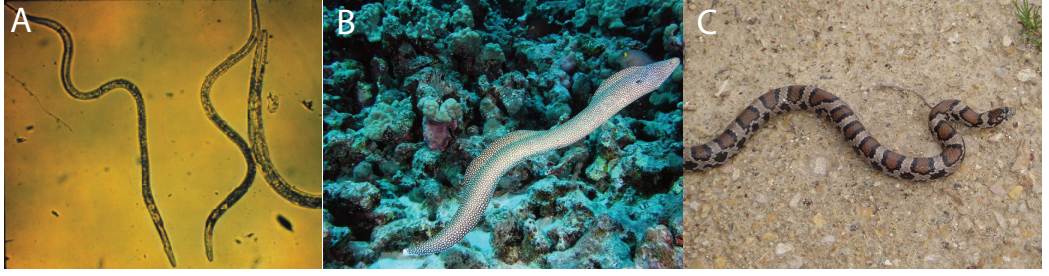
Figure 3: Undulatory locomotion in water and on the surface of the ground. A: Nematodes swim in water at low Reynolds number. B: An eel swims in water at high Reynolds number. C: A snake crawls on the surface of the ground.

1.1.2 Undulatory locomotion

Undulatory locomotion is widely used by organisms living in water [52, 67] and on the surface of the ground [54, 61] (Fig. 3). However, the dynamics can be very different because the reaction forces depend on the environment. Small organisms such as nematodes and spermatozoa live in fluids where viscous forces dominate and inertia is not important [52, 53]. Larger swimmers in water propel themselves with forces mainly come from accelerating or decelerating water. For terrestrial locomotion, frictional forces associated with the ground reaction forces usually provide thrust. The animals that use undulatory gaits often pass traveling waves posteriorly along the body although the exact waveform differs [54, 61, 52, 67].

A frequently used measure to characterize the performance of swimmers in deformable media is the wave efficiency η, defined as the ratio between the forward speed and the speed of the traveling wave [52, 46]. This number can take values between zero and unity (see Fig. 4); Wave efficiency cannot reach one because in that case the swimmer follows a trajectory of the traveling wave without deformation of the media and thus no thrust can be generated. The wave efficiency is usually near 0.2 for low Reynolds (Re) (a measure of the ratio of inertial forces to viscous forces) swimmers and is between 0.4 and 0.8 for high Re swimmers [46]. For a nematode moving on an agar-air interface, or a snake moving on solid surface using undulatory gait, the wave efficiency can reach above 0.8 [61, 53].

For low Reynolds number swimmers like nematodes and spermatozoa that use undulatory gaits, the swimming performance can be predicted by the resistive force theory (RFT),
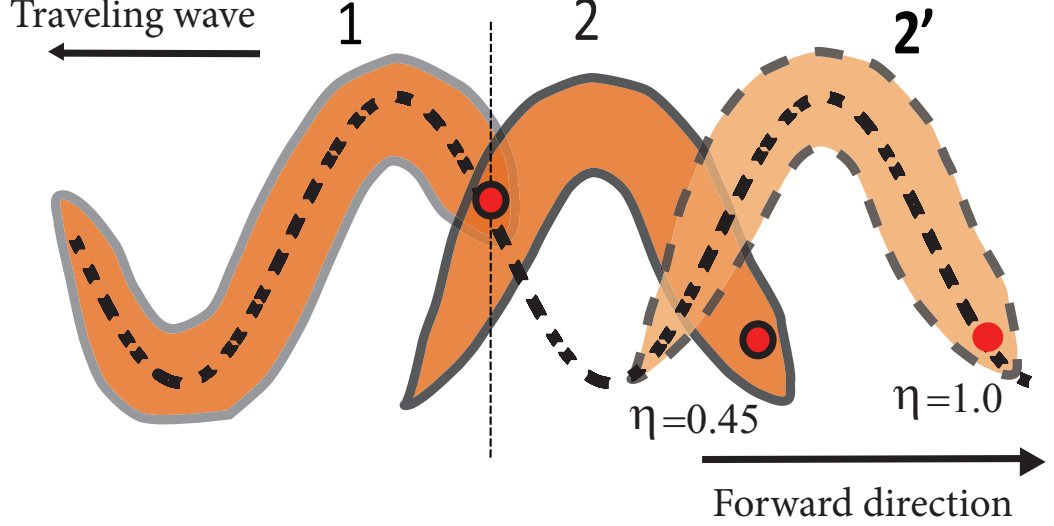
Figure 4: Diagram illustrating the concept of the wave efficiency (η)to describe the movement of an undulatory swimmer. Initial position of the swimmer is shown with a gray outline. The swimmer moves forward (right) as the traveling wave goes backward. For two representative cases $\eta = 1$ and $\eta = 0.45$, the final positions are indicated with dashed gray and black outlines, respectively.

which was first proposed by Gray [52] and Taylor [118]*et al.*. In the RFT, the body of the swimmer is divided into infinitesimal segments and interactions between segments are neglected. The net force on an organism can be obtained by integrating the local forces on each segment and the speed of the organism then can be predicted by solving force balance equations. However, for swimmers in high Re number fluids, the forces on a segment may be influenced by other segments because the flow generated by one segment may persist and interact with other segments. Therefore, models using the overall momentum and energy transfer between the body and water have been proposed to predict the swimming performance in high Re fluids [77]. Although theoretical models give insight into the basic mechanics of swimming in a fluid, the flow assumed by the theories is often over-simplified, especially for swimmers in high Re fluids. To accurately capture the complex flow of the media and realistic body deformation of the animals, computational fluid dynamics (CFD) methods are widely used (e.g. [122, 121, 127, 18]).
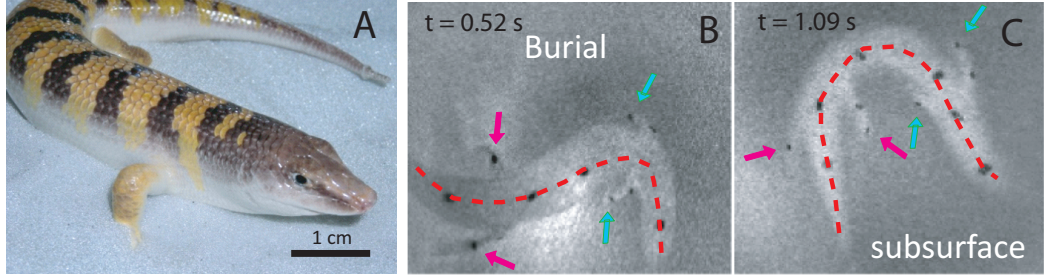
Figure 5: A: The sandfish lizard on 0.3 mm glass particles. B & C: Representative x-ray images of the sandfish as it buried into and move within the media with high amplitude oscillations. The green and magenta arrows indicate the location of the opaque markers on the fore and hind limbs of the animal respectively. The red dashed curve corresponds to the mid-line of the animal.

1.1.3   Sand-swimming of the sandfish lizard

Because dry sand is simpler compared to soil or debris and subsurface locomotion in sand is common among the animals living in the desert, we focused on swimming in sand. We study the sand-swimming of the sandfish, a small (10 cm) desert-dwelling lizard from the Saharan desert of Africa. We investigated how rheological features and how the resistive forces of the material influence the locomotor mode and performance of the animal[*]. Based on above-surface observations, previous researchers hypothesized that the sandfish used an undulatory gait to propel itself forward [7]. In our group's experiment, a fluidized bed (21.5 $\times$21.5$\times$18 cm^3) filled with 0.3 mm glass beads allowed the sandfish to swim within a granular medium of controlled and repeatable packing. Simultaneous visible light and high-speed x-ray imaging was used.

Side view x-ray imaging of the sandfish subsurface revealed that the sandfish executed lateral undulation and the body moved forward and down at an angle $\sim 22.2 \pm 3.7°$ with respect to the horizontal. We characterized the undulatory kinematics of the sandfish by by digitizing the midline from the dorsal x-ray images (Fig. 5). The undulations pattern is similar to small (< 1 mm) swimmers such as nematodes in fluids at low Re number. The undulatory motion was well described by a posteriorly traveling single period sinusoidal

---

[*]The animal experiments were conducted by Ryan Maladen, a bioengineering graduate student in Goldman's group. The results in this subsection has been published in a journal paper " Undulatory swimming in sand: subsurface locomotion of the sandfish lizard," Ryan Maladen, Yang Ding, Chen Li and Daniel I. Goldman, *Science*, 325, 314 (2009).
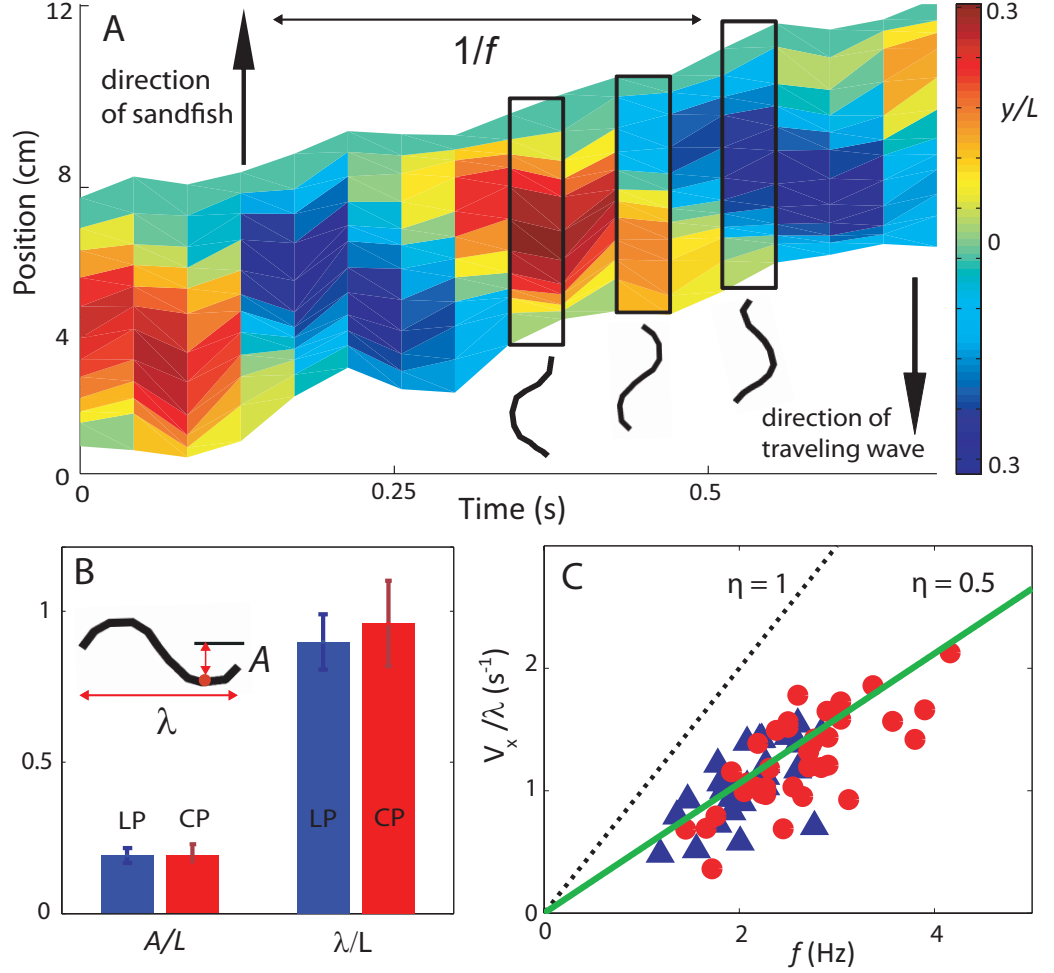
Figure 6: A: Traveling wave moving down the body of the sandfish opposite to the direction of the sandfish forward motion (sampled every 0.04 s). For each time instant, the instantaneous lateral displacement of a tracked section of the sandfish is represented in color. The black stick figures show the tracked mid-line of the sandfish. B: The amplitude A and wavelength λ of the sinusoidal fit to the tracked midline of the sandfish (inset), for loosely and closely packed media. C: Red circles (closely packed, n = 24 trials), and blue triangles (loosely packed, n = 22 trials) show dependence of swimming speed on wave frequency. The slope of green line is the approximate wave efficiency $\eta \approx 0.5$ of animal and the dashed black line represents $\eta = 1$.

wave (Fig. 6), that is $y = A \sin \frac{2\pi}{\lambda}(x + v_w t)$, where A is the amplitude, λ is the wavelength, f is the undulation frequency, and $v_w = f\lambda$ is the wave speed. From the fit, we obtained these parameters as well as the forward swimming speed of the center of mass v_x. We observed stereotyped kinematics: there were no significant changes in A or λ within a run and in differently packed media (see Fig. 6B). The sandfish increased swimming speed by increasing wave frequency f (see Fig. 6C). The wave efficiency, which can be calculated from the slope of v_x/λ as a function of f, was $\eta = 0.54 \pm 0.12$ and $\eta = 0.49 \pm 0.09$ for loosely and closely packed material, respectively. The difference between different packing states was not statistically significant ($p > 0.05$), despite the differently packed materials having different penetration resistances (see [75] and section 1.2). We observed that the sandfish was able to swim in $3\,\mathrm{mm}$ glass particles with the same (not statistically different) kinematics and performance. It is also interesting to note that the η for the sandfish in granular media falls between that in low Re fluids and on the surface of solids.

1.1.4   Application of sand-swimming robots

Robots that could move within complex material like sand, rubble, and loose debris are desirable. For example, such robots could help search for hazardous chemical leaks [63] and victims in disaster sites [86, 8, 85]. Limbless robots that use their bodies to move through material have advantages over those traditional wheeled [103, 113, 128, 6] and legged robots [18, 76, 105, 99, 59, 106, 69] in places where space is limited and/or obstacles are close to the size of the robot [36]. To explore celestial objects that are covered with granular media (regolith) and have very low gravity, locomotion is a challenge, especially for conventional wheeled vehicles [115]. A sand-swimming robot may have better mobility and the ability to explore places that are out of reach of surface vehicles. Although a few limbless robots have been developed for and tested in unstructured environments [19, 20, 35], most limbless robots have been developed for and tested on rigid surfaces [57, 109, 29, 70, 25].

1.2   Forces and flow in granular media

The forces between particles in dry granular media are repulsive and dissipative; the particles are subject to gravity and are confined by external boundaries. Despite this simplicity,
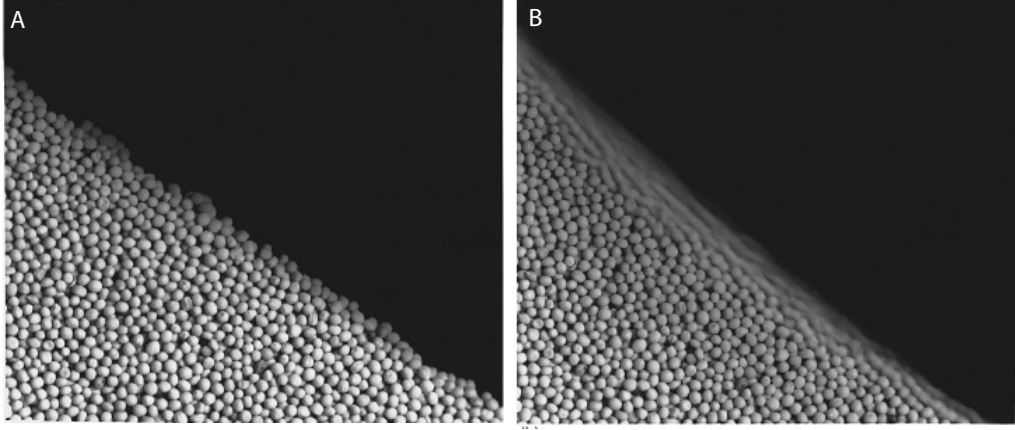
Figure 7: A pile of mustard seeds shows both solid-like and fluid-like behavior. A: The pile is tilted to an angle lower than the angle of repose. B: The pile is tilted to an angle higher than the angle of repose. (adapted from [65])

dense dry granular media can behave like a solid, fluid and a gas [65], often within the same experiment (see Fig. 7). Wet granular media, in which cohesive forces and fluid hydrodynamics play important roles, are even more complex and far more difficult to model; for example, a transition from frictional flow to lubricated flow may occur as stresses change in wet granular particles [62]. Therefore in this dissertation we focus on dry granular media and the models and results reported here are for dry granular media. Flowing, forced dry granular media are often classified into three different regimes [65, 44]: (1) a dense quasi-static regime in which inertia effects are negligible and frictional forces between particles dominate. The contacts between particles are endure and break infrequently; (2) a gaseous regime in which the distances between particles are long and the particles interact only at collision; (3) an intermediate fluid regime in which the flow is rapid and either collisions nor enduring contacts dominate.

Although the understanding of force and flow in granular media is not at the level of fluids, some principles about the resistive forces on intruders in granular media have been revealed. At low speed (quasi static regime), effects of inertia are negligible and the resistive forces are dominated by gravitational forces (weight of the media) and the frictional forces. Therefore, the forces are independent of speed [125, 17]. Because the weight of the particles at shallower depths is supported by deeper particles, the pressure increases with depth in
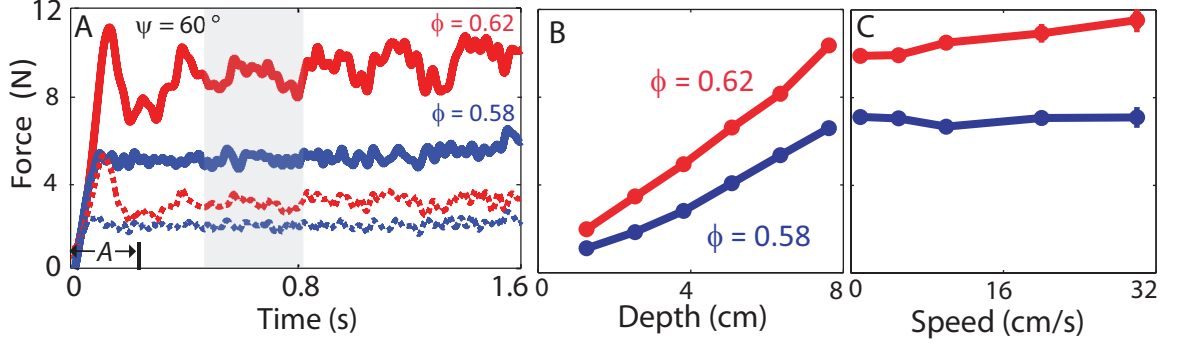
Figure 8: Representative total drag force profiles vs time for a stainless steel cylinder (diameter = 1.58 cm and length = 4 cm) oriented at an angle $\psi = 60°$ to the direction of its forward velocity (10 cm/s). The solid lines correspond to perpendicular component ($F_\perp^T$) and the dashed to parallel component ($F_\parallel^T$). Averaged force on the cylinder when it is oriented perpendicular to the direction of motion at different depths (B) and velocities(C) through granular media of low and high volume fractions. The red color represent CP and blue LP media.

granular media. However, due to frictional forces, granular media can maintain finite shear stress, and so the yield stress increases with depth [125, 3]. Due to the discrete nature of granular media, stress in granular media is often inhomogeneous and resistive forces may have significant fluctuations even in "steady state" [3, 51]. The resistive forces are also sensitive to the compaction of the media. The compaction can be quantified by the volume fraction ϕ, the ratio between the volume of the solid volume to the occupied volume. The volume fraction can vary between 0.57 and 0.64 [31] for granular media which consist of irregularly shaped (or spherical) particles. The magnitude of the drag force in granular media can change significantly (>50%) and the functional form of the drag can change qualitative with only a few percent of change in volume fraction [51]. These features of resistive forces in granular media were observed in our experiments measuring drag forces on a cylindrical rod through 0.3 mm glass particles as shown in Figure 8. When a intruder moves at high speed, such as the initial stage of a vertical impact, inertial effects become important and the vertical resistive forces scale with v^2 [21, 48].

Because the frictional force is the dominant force in the quasi-static regime, a granular medium can be modeled as ideal Coulomb material such that the material is rigid until the shear stress τ and normal stress σ satisfy the Coulomb yield criterion $\tau = \mu\sigma$ (μ is

the friction coefficient). For ideal Coulomb materials, some problems with simple geometry of slip plane (where material fails) can be solved analytically. For example, the retaining wall problem can be solved using Coulomb wedge method (see Fig. 9A). The force on a retaining wall can be solved by analyzing the force balance on the potential flowing region of the medium, whose shape is approximated as a triangle in the vertical plane. A similar analysis is presented in Chapter IV to explain the forces on a submerged plate.

To accurately describe the mechanical properties and the state of a granular medium, variables other than the properties of the particles must be considered as well. Since the particles are macroscopic, motion due to temperature is usually negligible. The lack of random motion of particles impedes the ability of the system to explore its phase space. When a granular medium yields under an external disturbance a new state will be reached and maintained. The possibility of different volume fractions with the same collection of particles is an examples that demonstrates the existence of many stable configurations of a collection of particles [24]. The dependence of the state of the medium on history makes the resistive force also depend on the history of disturbance [120, 97].

Computer simulations can provide more detailed information about the effects of parameters which are difficult to measure and vary experimentally. Simulation also are more flexible in modeling grains with different properties and complex geometry of containers or intruders. An important and useful model that is used to describe the flow of dense granular media is the discrete element method (DEM) (see Fig. 9A). The DEM simulation shares the same algorithm as that of the molecular dynamics (MD) simulation method to accelerate the computations [101](see Fig. 9). In DEM, particles are modeled as spheres with finite hardness so that particles can have enduring interaction. The trajectory of each particle is computed by integrating the net force on the particle twice during collision and under gravity. Force models for interaction between particles usually include repulsive forces in the normal direction and frictional forces in tangential direction. Force models have been proposed to capture various other features observed in contact and collision between particles, including Hertzian contact, velocity dependent restitution coefficient and Coulomb friction [33, 71].
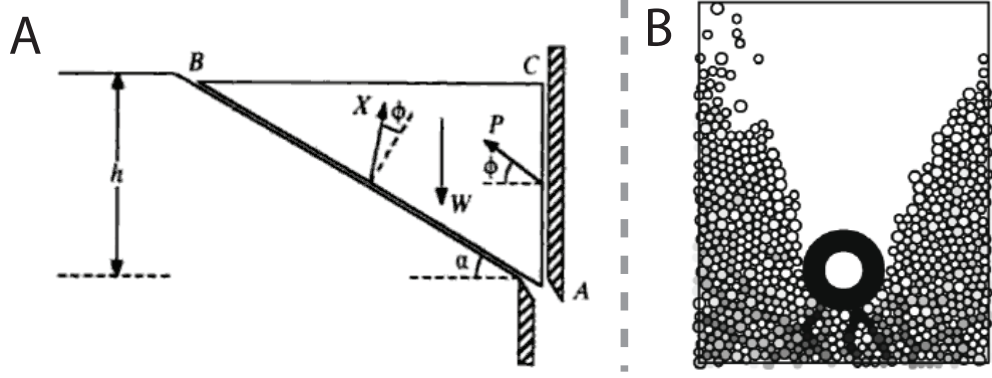
Figure 9: Two representative models of granular media. A: Coulomb wedge model solves the force on a retaining wall by analyzing the forces on the wedge $\triangle ABC$ (adapted from [92]). B: Discrete element method simulation of the impact of a intruder into granular media (adapted from [21]).

In this dissertation, I have developed theoretical (Chapter II) and numerical (Chapter III) models to study the mechanics of undulatory swimming in sand and the lift force in granular media (Chapter IV) during horizontal intrusion. Using the models, I have explained performance of the sandfish, revealed principles of the mechanics of undulatory sand-swimming, evaluated how granular forces and kinematics affect the swimming performance, revealed the shape dependent lift force in granular media and its important role in controlling the vertical motion of swimmers in granular media. A sand-swimming robot, whose design was guided by principles learned from the models, was used to test/validate model predictions about the the effects of kinematics on swimming performance (Chapter III) and the effects of lift force on vertical motion of swimmers (Chapter IV). My work includes the first sand-swimming models that incorperate detailed kinematics from animal experiments. These models show how the physics of granular media affects force generation and sand-swimming performance of the animal/robot. My work also provide hypotheses or answers to some important questions in animal locomotion such as how some morphological adaptations are related to vertical motion control in locomotion.

CHAPTER II

RESISTIVE FORCE THEORY

2.1 Introduction

Resistive force theory (RFT) model was first developed to explain the swimming speeds of micro-organisms in fluids at low Reynolds numbers (Re) [52], where viscous forces dominate and inertial effects are negligible. In the RFT model, the organisms are modeled as flexible rods whose shape varies as a traveling sinusoidal wave. The body is assumed to travel in the opposite direction of the traveling wave and the lateral motion and yaw motion were not considered in its original form [52] and this chapter. In RFT model, the body of the organism is partitioned into elements; each element generates thrust and experiences drag when moving through a media and forces on one element are not influenced by force fields from other segments. By integrating the forces for each element over the length of the body for a full period of a traveling wave, the net force on the body can be calculated (see Fig. 10). The net force is then set to zero to obtain the average swimming speed.

Because inertia is negligible at low speed in granular media (like in low Re fluids) and the kinematics of the sandfish can be well estimated with a traveling sinusoidal wave, we developed a RFT model with empirical granular force laws to explain the sand-swimming performance of the sandfish *. With mathematical approximations in the calculation and piecewise-linearization of empirical force laws, we solved the RFT model analytically and obtained insight into how the undulation amplitude and resistive forces determine the swimming performance †.

---

*This work has been published as part of a journal paper: "Undulatory swimming in sand: subsurface locomotion of the sandfish lizard," Ryan Maladen, Yang Ding, Chen Li and Daniel I. Goldman, *Science*, 325, 314 (2009)

†This work has been published as part of a journal paper: "Mechanical models of sandfish locomotion reveal principles of high performance subsurface sand-swimming," Ryan D. Maladen, Yang Ding, Paul B. Umbanhowar, Adam Kamor, and Daniel I. Goldman, *J. R. Soc. Interface*, 8, 1332-1345, (2011)
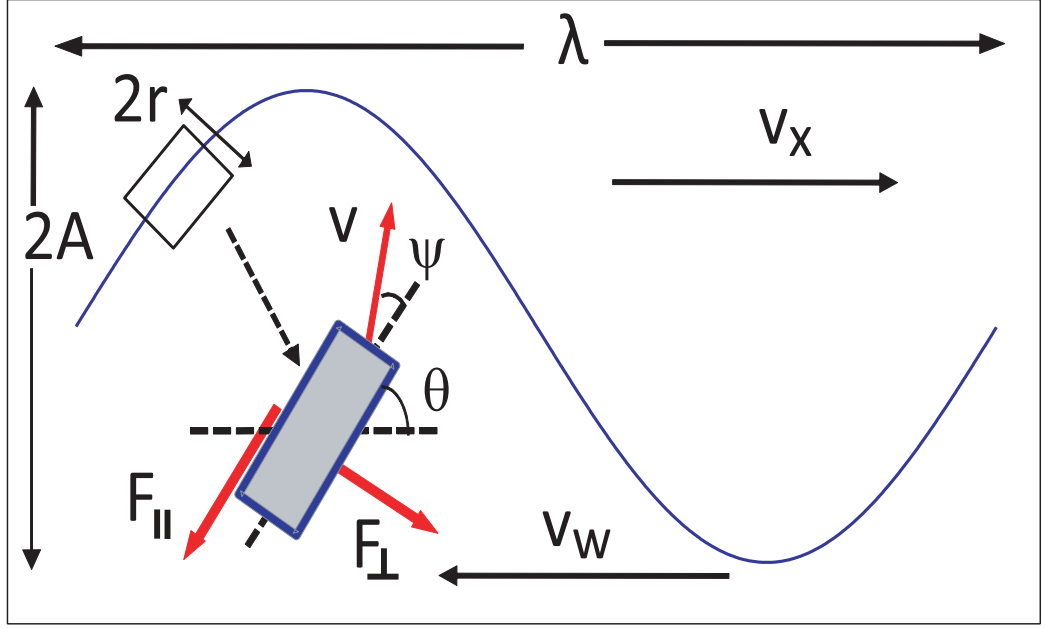
Figure 10: Schematics of the resistive force theory and the force diagram on a segment on the body.

2.2 Formulation

The sinusoidal traveling wave progressing from head to tail of the animal (Fig. 10) can be approximated as:

$$y = A \sin \frac{2\pi}{\lambda}(x + v_w t), \tag{1}$$

where x is the position in the direction of motion, y is the displacement away from the midline of a straight animal, A the amplitude, λ the wavelength, f the wave frequency, t the time, and $v_w = f\lambda$ the wave speed. For a given forward velocity v_x, other quantities characterizing the motion can be calculated:

$$v_y = \frac{dy}{dt} = \frac{2A\pi v_w}{\lambda} \cos \frac{2\pi}{\lambda}(x + v_w t) \tag{2}$$

$$\tan \theta = \frac{dy}{dx} = \frac{2A\pi}{\lambda} \cos \frac{2\pi}{\lambda}(x + v_w t) \tag{3}$$

$$\psi = \arctan(\frac{v_y}{v_x}) - \theta, \tag{4}$$

14

where θ is the angle of the axis of an infinitesimal cylindrical element with respect to the midline and ψ the angle between the axis of the element and its instantaneous velocity.

As shown in Figure 10, the force on an infinitesimal element of the animal is decomposed into forces $F_\perp$ and $F_\parallel$, the normal and lateral forces (perpendicular and parallel to the element axis respectively). We assume that the forces on an infinitesimal element of the animal are proportional to the area of the longitudinal cross section $\delta A = 2r\delta s$ ($2r$ is the height of the body and δs is an infinitesimal arch length.), and are functions of ψ (see section 2.3 for details of the empirical force model). The resultant force on the element in the forward direction $(+x)$ is:

$$\delta F_x = (P_\perp \sin\theta - P_\parallel \cos\theta)2r\delta s, \tag{5}$$

where $P_\perp$ and $P_\parallel$ are the forces per cross section area normal and parallel to the axis of the element. The total force on the body F_{bx} in the direction of motion can then be expressed as

$$F_{bx} = \int_0^\lambda (P_\perp \sin\theta - P_\parallel \cos\theta)\sqrt{1 + \tan^2\theta}2rdx. \tag{6}$$

Although the angle of each element changes in time, since the integral is over one full wavelength, the integral in Equation 6 is time invariant.

Equation 6 accounts for the forces acting on the body but not the head. To include the forces on the head, we use two limits: a flat head (FH) that produces maximum drag and no head (NH) which produces no drag. For the FH model, the drag on the head F_h can also be decomposed into two orthogonal components $F_\perp^T$ and $F_\parallel^T$. The net force in the forward $(+x)$ direction on the head becomes:

$$F_{hx}(t) = F_\perp^T \sin\theta - F_\parallel^T \cos\theta. \tag{7}$$

The drag force on the head is set to zero for the NH model.

For each cycle, the head (as well as the segments on the body) goes through every point of one wavelength of the traveling wave. Therefore, the time average of the force on the head $(\bar{F}_{hx})$ is equal to the spatial average:

$$\bar{F}_{hx} = \frac{1}{T} \int_0^T F_{hx} dt = \frac{1}{\lambda} \int_0^\lambda (F_\perp^T \sin\theta - F_\parallel^T \cos\theta) dx. \tag{8}$$

Combining the head drag with the body force we obtain the total time averaged force on the model sandfish:

$$\bar{F}_x = \int_0^\lambda [(P_\perp(\psi) \sin\theta - P_\parallel(\psi) \cos\theta) \sqrt{1 + \tan^2\theta} \, 2r$$
$$+ (F_\perp^T \sin\theta - F_\parallel^T \cos\theta)/\lambda] dx. \tag{9}$$

For a constant average speed, $\bar{F}_x$ is zero. The forward velocity v_x can then be found numerically if v_w, A, λ, $P_\perp(\psi)$, $P_\parallel(\psi)$, $F_\parallel^T$ and $F_\perp^T$ are known. The calculation is done using MATLAB (MathWorks) and the function *fminsearch* is used to find the root by minimizing the magnitude of net force. In next section, we use empirical force laws obtained form experiment and simulation to determine $P_\perp(\psi)$, $P_\parallel(\psi)$, $F_\parallel^T$ and $F_\perp^T$ in the RFT model.

2.3 Empirical force laws

For swimming in low Re fluid ($Re \ll 1$), the resistive forces are proportional the speed of the rod. The normal and parallel components of the force ($F_\perp$ & $F_\parallel$) on a segment on the body are proportional to their corresponding velocity components:

$$F_\perp = C_N v_\perp$$
$$F_\parallel = C_L v_\parallel. \tag{10}$$

where C_N and C_L are the coefficient for the normal and parallel component of the force and their ratio C_N/C_L is close to 2 [50, 52]. However, such force laws do not exist for granular media. Therefore we use empirical force laws measured in experiment.

2.3.1 Rod drag experiments and simulation

To obtain expressions for the forces on the sandfish, we dragged a stainless steel cylindrical rod through granular media at a constant speed ($10\,\mathrm{cm/s}$) and measured the resulting normal and lateral forces as a function of the angles between the rod axis and its motion direction ψ ranging from $0°$ to $90°$ (Fig. 11)*. We chose stainless steel because sandfish

---
*The experiment was conducted by Chen Li, a physics PhD student in the Goldman group.

16
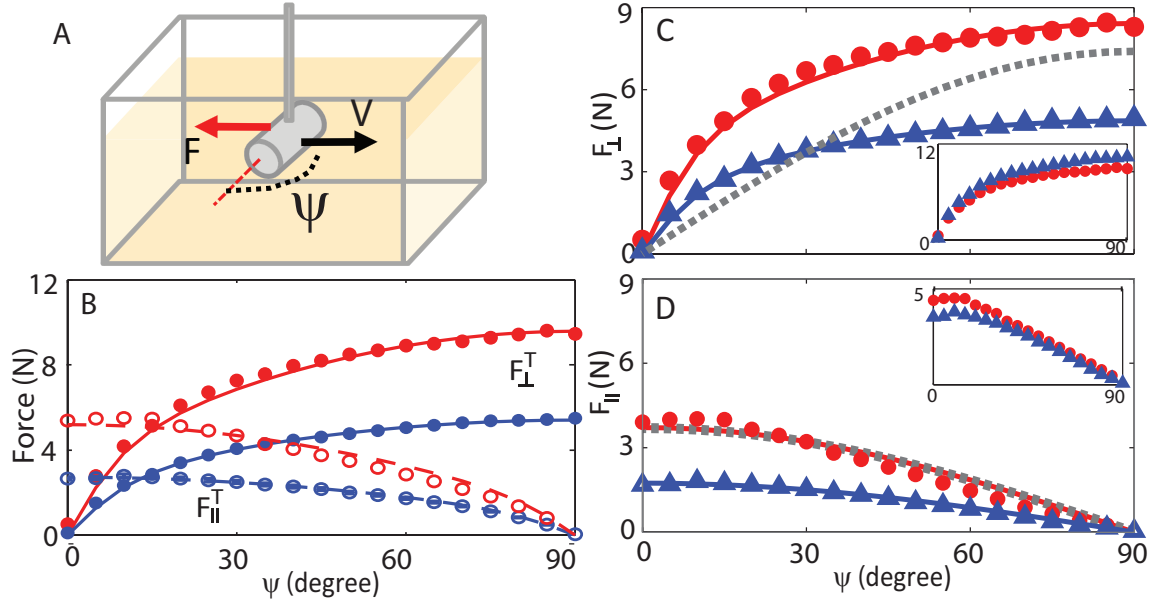
Figure 11: A: Schematics of the experiment. B: Average total forces (including sidewalls and end-caps) $F_\perp^T$ (closed symbols) and $F_\parallel^T$ (open symbols) on the cylinder dragged in $0.3\,\mathrm{mm}$ glass particles as a function of the angle between its axis and direction of motion ψ. C: The normal component $F_\perp$ of the force on the sidewall of the rod. D: The parallel component $F_\parallel$ of the force on the sidewall of the rod. The color of the symbols denote close (red) and loose (blue) packed preparations. Solid lines are model fits described by Equation 11. Dashed gray lines correspond to $F_\perp$ and $F_\parallel$ calculated for a low Re fluid (see Eqn. 10) by choosing a velocity that fits $F_\parallel$ versus ψ. All forces are calculated by averaging instantaneous forces over steady state motion (e.g., see gray region in Fig. 8A).

skin and stainless steel have similar friction coefficients with sand ($\approx$0.2 based on own measurement and [11]). The diameter of the cylinder ($2r = 1.58$ cm) is similar to that of the sandfish body. We used a fluidized bed to set the initial volume fraction (ϕ) of the media [64, 107, 108]. The cylinder was attached to a robotic arm (CRS Robotics) via a connecting rod to a force sensor (ATI industrial) which measured the net force generated during the horizontal motion. The force on the connecting rod was measured separately and subtracted to obtain the force on just the cylinder. The total forces $F_\perp^T$ and $F_\parallel^T$ were obtained as the averages over the steady state forces, indicated by the shaded region in Figure 8A.

Previous studies showed that drag in granular media was independent of speed ([126, 3]) and increased proportionally to depth ([126]). To test if this effect persisted in the regime relevant to the sandfish (0-40 cm/s), we dragged the cylinder perpendicular to its axis at different speeds (which encompass the sandfish's range of speeds) at a fixed depth of 7.6 cm. We found that over an order of magnitude change in speed, force only changed by 10% (Fig. 8B). We also dragged the cylinder oriented perpendicular ($\psi = 90°$) to its axis at different depths at 10 cm/s and confirmed that drag is proportional to depth [3] (see Fig. 8B). Therefore, to determine the empirical force laws for the RFT, we dragged the cylinder at a fixed depth of 7.6 cm and a constant speed of 10 cm/s for different ϕ.

We would like an expression for force on an infinitesimal (or small) segment of the sandfish body but the measured forces in experiment includes the forces on both the side-wall and the end cap on the leading side. Simulation has the advantage that the forces on the sidewall and the end-cap can be directly measured separately. We conducted rod drag experiments in a experimentally validated DEM simulation with a similar-sized rod (square cross-section, width=height=1.6 cm, length=4 cm) but different particles (3 mm & 6 mm diameter) to apply the RFT to sandfish swimming in 3 mm glass particles and a sand-swimming robot swimming in 6 mm plastic particles (see section 3.2.1 for details of the simulation and [82] for the robot development). The shapes of the force curves from simulated 3 mm particles are similar to those from experimental measurements in 0.3 mm particles (see Fig. 12 & 13).
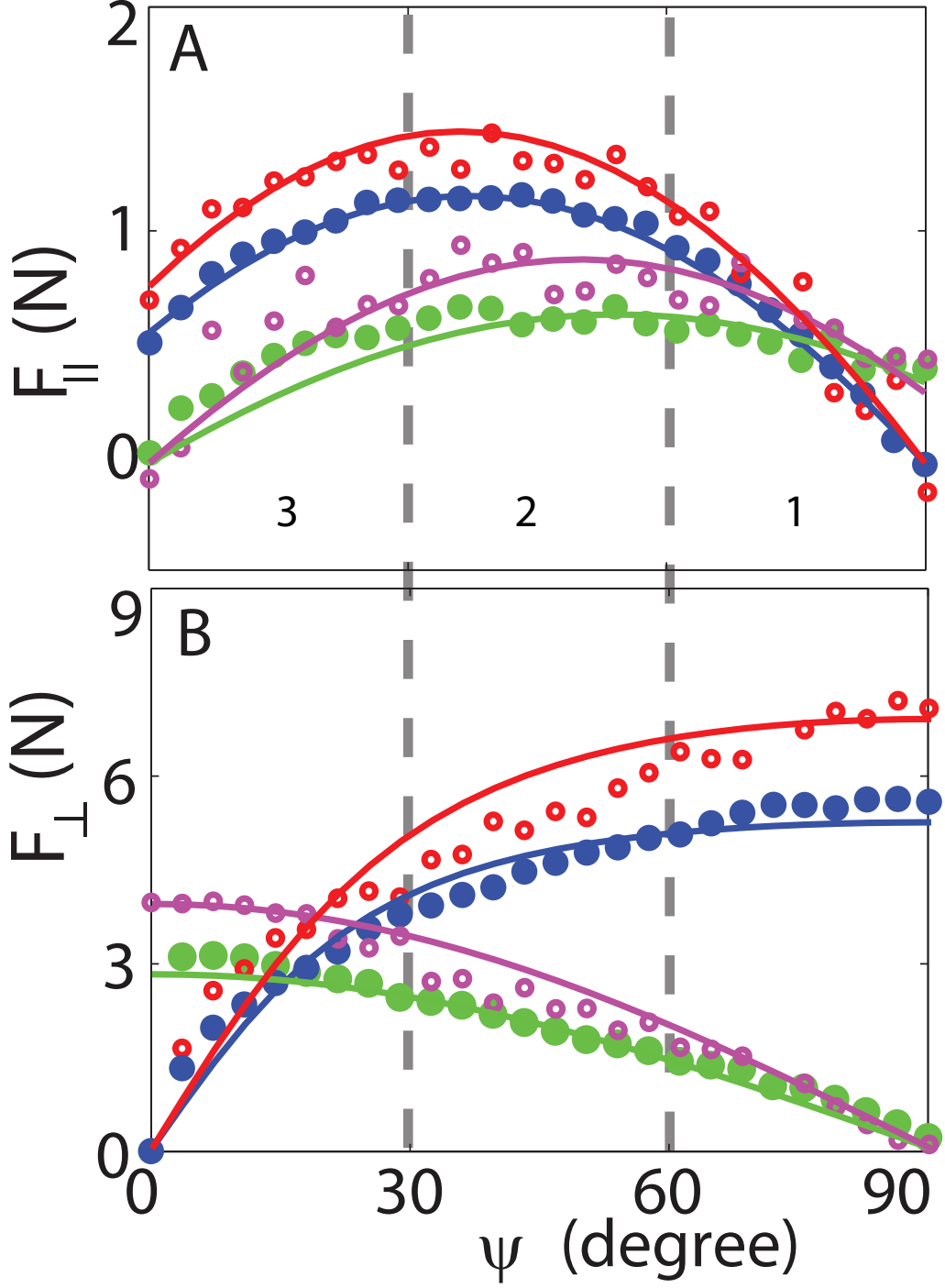
Figure 12: Parallel component $F_{\parallel}$ (A) and perpendicular component $F_{\perp}$ (B) of the force on a square cross-section rod (width, height=1.6 cm, length=4 cm) dragged through 3 mm glass particles in simulation as a function of the angle between the velocity direction and the rod axis, ψ. Blue and red markers correspond to forces along the length of the rod while green and magenta markers correspond to forces at the end-caps of the rod. Filled and open circles correspond to loosely and closely packed media, respectively. Solid lines denote fits to Equation 13 with fit parameters given in Table 2. Regions 1-3 separated by dashed gray lines correspond to similarly marked regions of between η and A/λ in Figure 15.
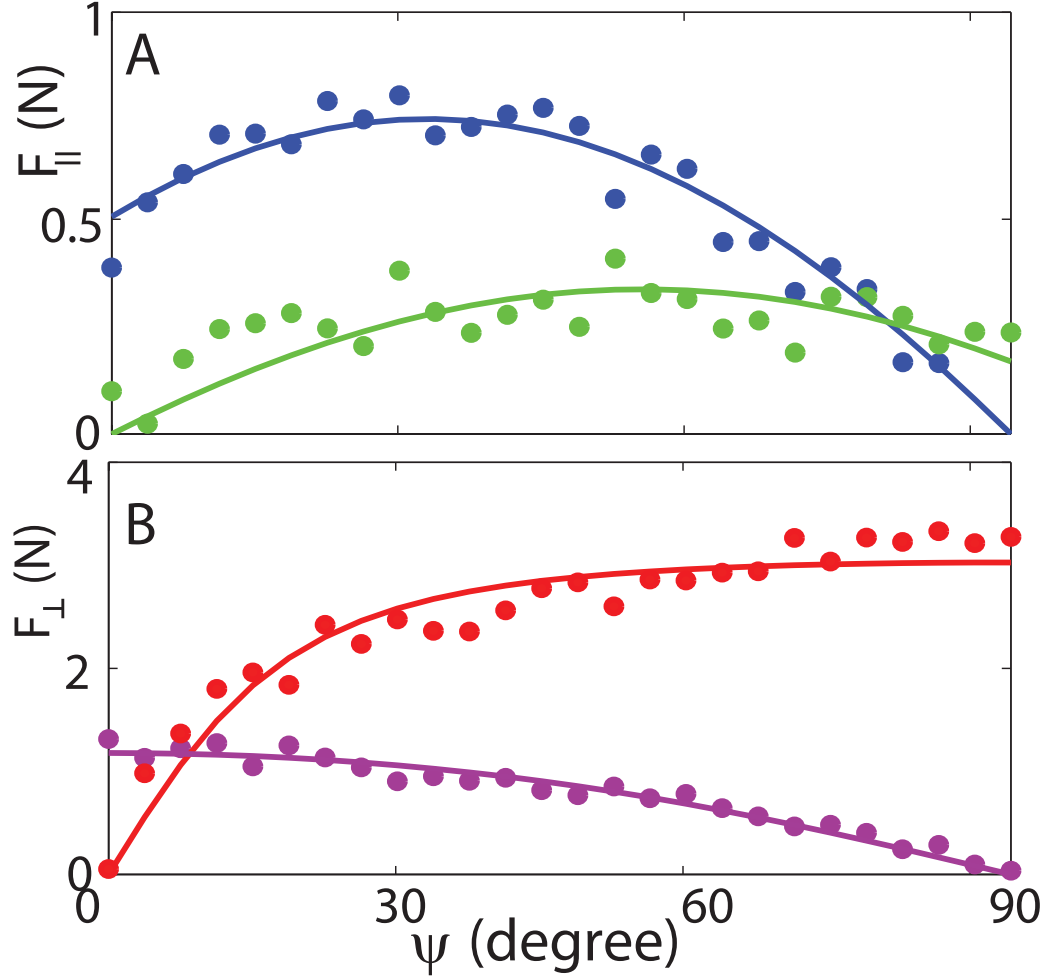
Figure 13: Parallel component $F_{\parallel}$ (A) and perpendicular component $F_{\perp}$ (B) of the force on a square cross-section rod (width, height = 1.6 cm, length = 7 cm) dragged through loosely packed 6 mm plastic particles in simulation as a function of the angle between the velocity direction and the rod axis, ψ. Blue and red markers correspond to forces along the length of the rod while green and magenta markers correspond to forces at the end caps of the rod. Parameters for the simulation are given in Table 4. Solid lines denote fits to Equation 13 with fit parameters given in Table 2.

Similar to the forces in low Re fluids or on frictional surface, as ψ increases, $F_\perp^T$ (and $F_\perp$) increase and then plateau for high ψ. However, the form of $F_\perp$ cannot be well approximated by the corresponding sine component (Fig. 11C, dashed gray lines) but rather increases more rapidly for $\psi < 30°$ and increases more slowly for $\psi > 30°$. $F_\parallel^T$ (and $F_\parallel$) decreases with ψ after a relatively small increase for $\psi <\approx 20°$. We hypothesize that the plateau of $F_\perp$ and $F_\parallel$ at $20° < \psi < 30°$, close to the angle at which internal slip planes or shear bands form and move [92], is a consequence of the formation of a solid region of grains that moves along with the rod [92, 126]. Preliminary numerical simulation indicates that the size of the solid region grows slowly with ψ for $\psi > 20°$.

2.3.2 Empirical fitting function

The experimentally measured forces include contributions from the surfaces on both the sidewall (length) and end-cap of the cylinder. However, we want to separate the forces from different surfaces so that the forces on the animal body are approximated using the forces on the length of the cylinder and the forces on the animal head are approximated using the forces on the end-cap. In experiment, to separate the forces as well as to characterize the relation between the measured values of normal and parallel forces as functions of its orientation with analytical form, we developed empirical fitting functions. For a cylinder with length l and radius r, the total forces $F_\perp^T$ and $F_\parallel^T$ can be written as the sum of the forces on the body, which is proportional to $2lr$ and the forces on the end-cap, which is proportional to πr^2:

$$
\begin{aligned}
F_\perp^T &= 2lr(C_S \sin \beta_0 + C_F \sin \psi) + \pi r^2 C_F \sin(\psi) \\
F_\parallel^T &= 2lr C_F \cos \psi + \pi r^2 C_S \sin \beta_0',
\end{aligned}
\tag{11}
$$

where $\tan \beta_0 = \cot \gamma_0 \sin \psi$, $\tan \beta_0' = \cot \gamma_0 \sin(\pi/2 - \psi)$, and γ_0 is a parameter.

The fits to the measurements of $F_\perp^T$ and $F_\parallel^T$ determine the three parameters C_S, C_F and γ_0. These parameters are given in Table 1. The terms that are proportional to $2rl$ were

21

Table 1: Fitting parameters for the analytical functions approximating $F_\perp$ and $F_\parallel$ from 0.3 mm glass particles.

Packing	ϕ	C_S (N/m$^2 \times 10^{-4}$)	C_F (N/m$^2 \times 10^{-4}$)	γ_0 (degree)
LP	0.58	0.51	0.28	13.84
CP	0.62	0.77	0.59	12.21

Table 2: Fitting parameters for the analytical functions approximating $F_\perp$ and $F_\parallel$ from 3 mm glass particles and 6 mm plastic particles. Units for C_S, C_F and C_L are N and γ is dimensionless.

	C_S	C_F	C_L	γ
3mm particles LP length	5.57	2.30	-1.74	1.93
3mm particles LP end cap	19.52	1.24	-0.99	0.14
3mm particles CP length	7.70	2.79	-2.03	1.575
3mm particles CP end cap	42.16	1.87	-1.58	0.088
6mm particles length	3.21	1.34	-0.82	2.79
6mm particles end cap	0.73	0.30	-0.19	0.52

used to approximate the forces on the body, that is

$$F_\perp = 2lr(C_S \sin\beta_0 + C_F \sin\psi)$$

$$F_\parallel = 2lrC_F \cos\psi. \tag{12}$$

For the forces from 3mm and 6mm particle simulation, the directly measured $F_\perp$ and $F_\parallel$ were slightly different from the calculated forces from 0.3 mm particles. Therefore, we modified fitting functions to obtain analytical expressions for $F_\perp$ and $F_\parallel$ as functions of ψ for the data shown in Figures 12 & 13:

$$F_\perp = C_S \sin\beta_0$$

$$F_\parallel = [C_F \cos\psi + C_L(1 - \sin\psi)], \tag{13}$$

where $\tan\beta_0 = \gamma\sin\psi$. For the forces on the end caps, the same fitting functions are used but ψ is replaced by $\pi/2 - \psi$ since the surfaces of the end caps are perpendicular to the rod axis. See Table 2 for the values of the fitting parameters C_S, C_F, C_L and γ.
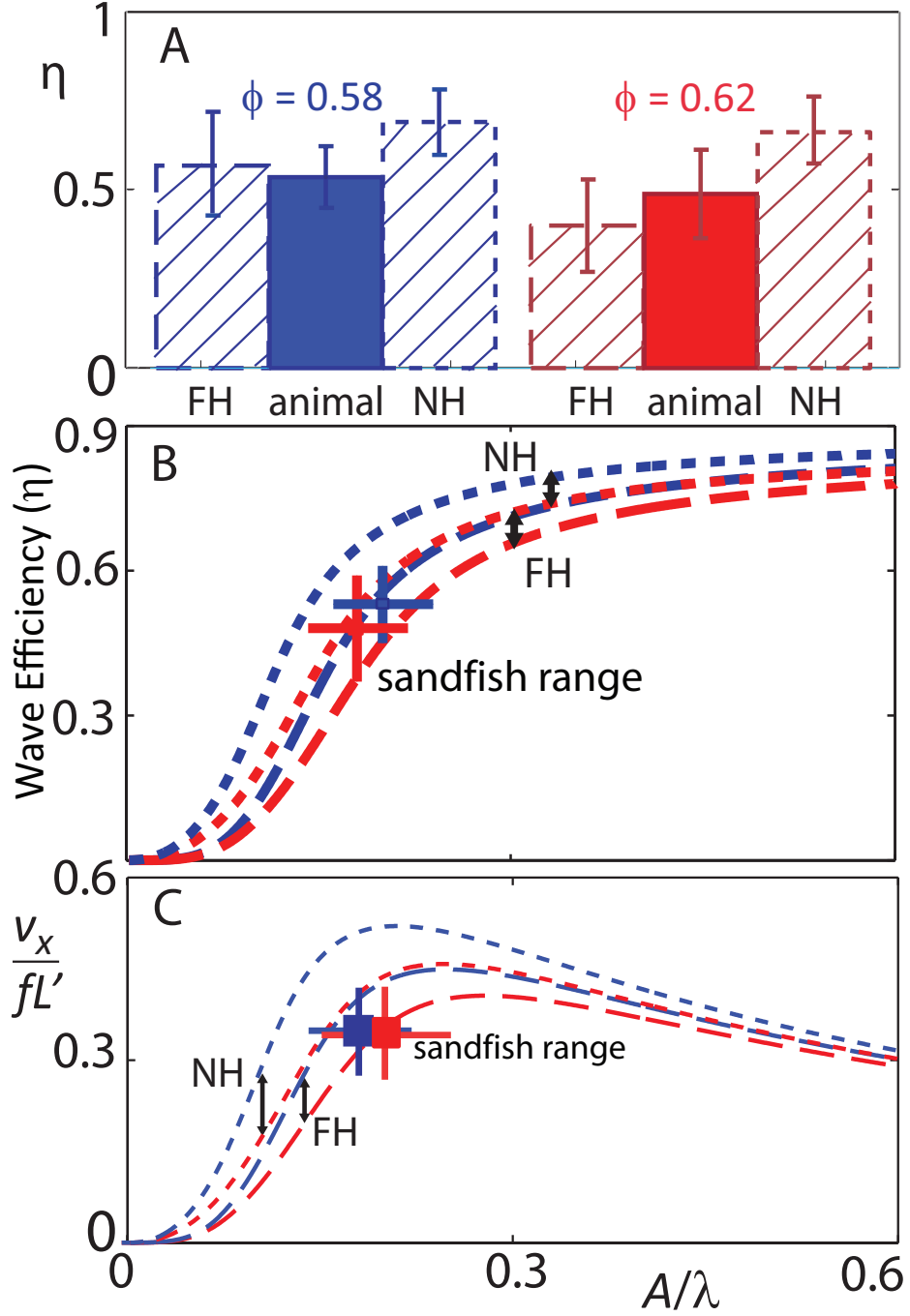
Figure 14: Comparison of experimental results and model predictions on sand-swimming performance of the sandfish in $0.3\,\text{mm}$ glass particles. Blue denotes loosely packed (LP) and red denotes closely packed (CP) material. A: Animal wave efficiencies from experiment are represented by solid bars (LP average $\eta = 0.54 \pm 0.12$, CP average $\eta = 0.49 \pm 0.09$). Shaded bars correspond to model predictions assuming head drag of a flat disk (FH) and no head drag (NH). B: The wave efficiency predicted by the RFT model as a function of amplitude normalized by wavelength (A/λ). C: Predicted swimming speed (in snout to tail tip length per cycle) versus (A/λ). The dashed lines are model predictions with no-head (short dashes) and flat-head (long dashes). Squares denote the measured average animal swimming speed from experiment. The range of frequency and speed accessed is given by the extent of the solid lines.

23
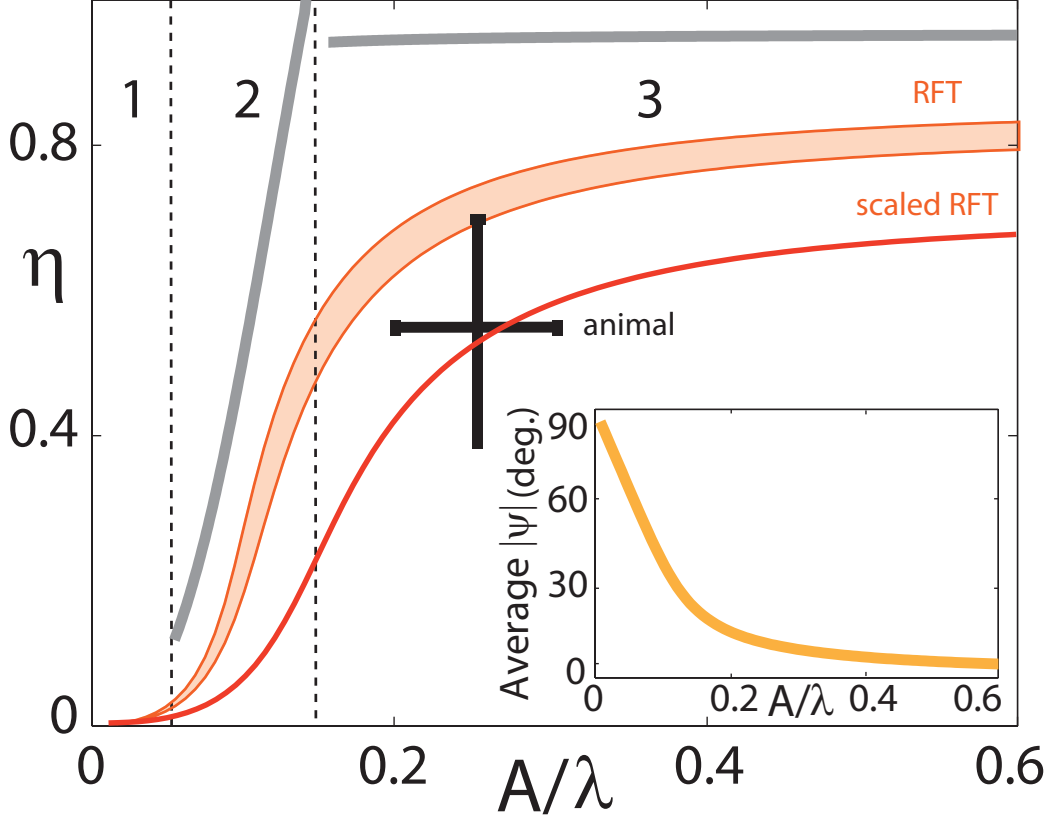
Figure 15: Wave efficiency η vs. amplitude to wavelength ratio A/λ for the numerical sand-fish simulation with a tapered square cross-section body (dashed and triangles, $f = 4$ Hz) in 3 mm particles. The orange shaded region corresponds to the RFT prediction for square cross-section body for maximum (flat plate, lower bound) and 30% of the maximum head drag (higher bound), respectively. The black cross corresponds to the animal experiments ($A/\lambda = 0.25 \pm 0.07$, $\eta = 0.53 \pm 0.16$). Gray solid curves correspond to analytical RFT solutions, and are divided into regions 1, 2, and 3 by dashed black vertical lines (regions correspond to those marked in Fig. 12). The red curve is the RFT prediction of η with the net force on each element scaled by 0.5 (see section 3.5.2). Inset: the average of the absolute value of ψ decreases with A/λ.

2.4 Results

2.4.1 Wave efficiency

Since the wave and body velocities in Equation 9 only appear as ratios (see Eqn. 2, 3 and 4) and do not appear in expressions for $P_\perp$ or $P_\parallel$, a proportional relation between v_x and v_w is expected. We can thus solve for the wave efficiency $\eta = v_x/v_w$. The RFT model predicts $0.4 \leq \eta \leq 0.65$ independent of ϕ (Fig. 14), which is in accord with experimental observation; the bounds on η are set by assuming the head drag is either zero or that of a flat plate because a measurement of the drag force on an object with the exact morphology of the wedge shaped sandfish head was not available.

It is remarkable that η does not change significantly for different ϕ, especially because drag forces for closely packed media is nearly as twice large as that in loosely packed material (Fig. 8). The model indicates that η is essentially constant because $F_\perp$ and $F_\parallel$ scale by the same ratio of 2.1 between closely and loosely packed material (see Fig. 11, C & D, insets), and it is the relative magnitude of $F_\perp$ to $F_\parallel$ that determines η (Eqn. 9 is unchanged if all forces are scaled by the same factor.). In low-Re fluids, the perpendicular force and parallel force are proportional to the perpendicular and parallel velocity component respectively, but with different coefficient. These force laws are shown as gray lines in Figure 11, B and C. The ratio between the two coefficients is usually near 2 [52], which generates a relatively smaller perpendicular force. The model implies that η is greater for sandfish than swimmers in low Re fluids because of the greater thrust to drag force ratio in granular media for all ψ.

Good agreement of the wave efficiency between experiment and RFT model was obtained for sandfish swimming in 0.3 mm particles but the RFT model systematically over-predicted the wave efficiency for sandfish swimming in 3 mm particles as shown in Figure 15. The over-prediction of the RFT model for sandfish swimming in 3 mm is due to a transition weakening effect when the displacement is nearly zero. More detailed discussion will be presented in Chapter III when we examine the detailed mechanics with simulation. We scaled the thrust forces by 0.5 to take into account the transition weakening effect and that resulted in a better match between RFT and experiment (the red line in Fig. 15).
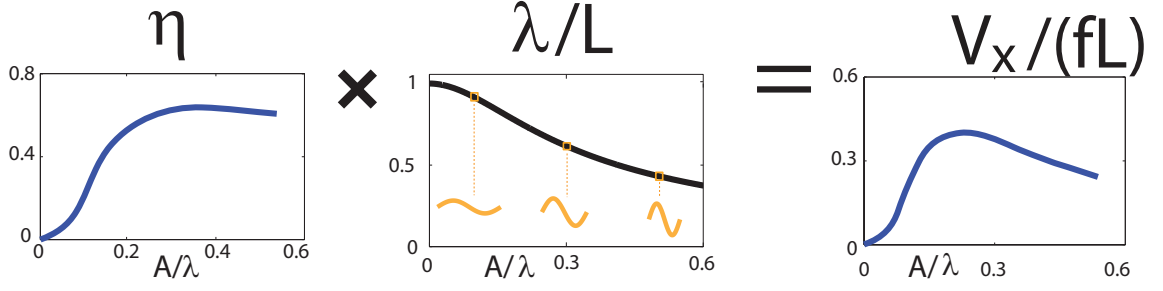
Figure 16: Competition between η and λ with varying A revealed that an optimal amplitude which maximize forward sand-swimming speed exist.

2.4.2 Optimal undulation amplitude

We now use the RFT model to investigate how swimming performance depends on variation of the spatial form of the sinusoidal wave. This allows us to systematically test our models and to advance an argument for why the rapidly escaping animal uses only limited ranges of A and λ. The RFT model predicts that the η increases rapidly with increasing A/λ for $A/\lambda \lesssim 0.3$ and increases slowly for $A/\lambda \gtrsim 0.3$. The model predicts a maximum in forward progress per cycle when $A/\lambda \approx 0.2$, and we find that the measured kinematics fall close to this speed (Fig. 14C).

We found that operating at large A/λ comes at a cost: λ decreases as A/λ increases since the animal has a finite length. The competition between the increase of η and decrease of λ results in the maximum speed (Fig. 16). This becomes more clear when the forward speed (in body-lengths traveled per cycle) is expressed as

$$v_x/fL = (\eta f \lambda)/fL = \eta \lambda / L. \tag{14}$$

2.5 Analytical solution

Since the maximal speed of sand-swimming is determined by the dependence of η on A/λ, it is important to understand how parameters in the model affect this functional relationship. Therefore, we gain insight into this function by developing analytic solutions of the RFT in three regions: low A/λ where η increases with positive curvature, intermediate A/λ where η increases significantly and high A/λ where η is largely independent of A/λ.
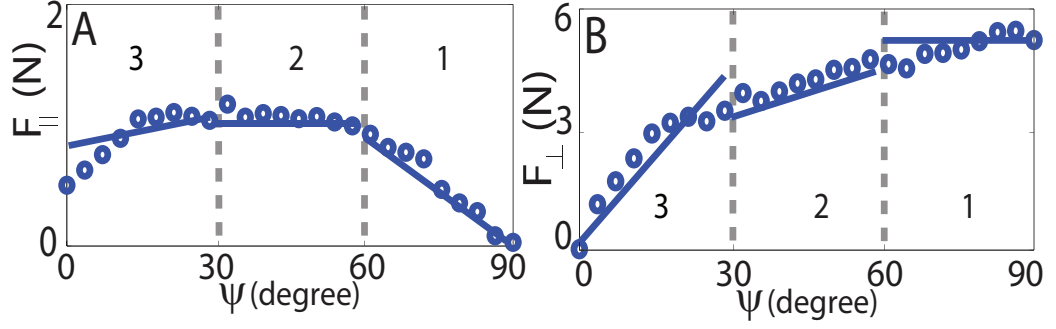
Figure 17: The normal component $F_\perp$ (A) and parallel component $F_\perp$ (B) of the force on the sidewall of a rod dragged in $3\,\mathrm{mm}$ particles. Solid lines are the piecewise linear fitting functions (Eqns. 15 19 and 23). Regions 1-3 separated by dashed gray lines correspond to similarly marked regions of between η and A/λ in Figure 15.

As Equation 5 shows, thrust is determined by the orientation θ of the element, where the average $|\theta|$ of the all elements increases with increasing A/lambda. and the magnitude of the normal force. The increase in the projected area of the element perpendicular to the forward motion of the animal (which increases thrust) explains the increase in η as a function of A/λ. Understanding the form of η vs. A/λ in the three regions, however, requires examination of the measured force laws (Fig. 12). Due to the non-trivial dependence of the force on ψ, we divide the η vs. A/λ relationship into three adjacent regions (Fig. 17) in each of which we approximate the force as either constant or linearly dependent on ψ. Below we give a summary of the calculations.

The order of the regions in Fig. 15 and Fig. 17 are reversed because A/λ and ψ are inversely related (see Fig. 15 inset). As solving the RFT numerically without head drag does not qualitatively affect the dependence of η on A/λ, we neglect head drag to simplify the analysis. We approximate $P_\perp$ and $P_\parallel$ as piece-wise linear functions of ψ. Approximation techniques are then used to obtain simpler analytical solutions.

2.5.1 Region 1

For small and increasing oscillation amplitude (and similarly for A/λ and θ), η increases from zero with an increasing rate. In this region as ψ decreases, the displacement of an element of the body of the animal remains nearly perpendicular to its forward velocity $\psi \approx \pi/2$ (see Fig. 12) for a majority of the cycle resulting in $F_\perp$ remaining nearly constant

(at its maximum) while $F_\parallel$ increases. Consequently, the stresses perpendicular and parallel to an element can be approximated as:

$$P_\perp = \frac{F_\perp}{bd} = C_{S\perp}^1$$
$$P_\parallel = \frac{F_\parallel}{bd} = C_\parallel^1 (\pi/2 - \psi),$$

(15)

where b and d are the height and length of the rod, and $C_{S\perp}^1$ and $C_\parallel^1$ are region specific (indicated by the superscript) constants. In Region 1, because the amplitude of undulation (A/λ) is small, θ is much less than unity (see Eqn. 3). Since the projection of the normal force (thrust) in the forward direction is small compared to the total force, the forward speed and hence the η is small. Also ψ is close to $\pi/2$ for most of each cycle. Accordingly we use the approximations $\theta \approx 0$ and $\psi \approx \pi/2$.

Starting with the expression for ψ given in Equation 4 and noting that $v_x/v_y = \tan\left[\pi/2 - \tan^{-1}(v_y/v_x)\right] \approx \pi/2 - \tan^{-1}(v_y/v_x)$ we approximate ψ as follows:

$$\psi = \tan^{-1}(v_y/v_x) - \theta$$

$$\approx \pi/2 - v_x/v_y - \theta$$

$$\approx \pi/2 - \frac{\eta v_w}{\frac{2\pi A v_w}{\lambda} \cos\frac{2\pi}{\lambda}(x + v_w t)} - \frac{2\pi A}{\lambda} \cos\frac{2\pi}{\lambda}(x + v_w t)$$

(16)

$$= \pi/2 - \frac{\eta}{I} - I, \text{ where } I = \frac{2\pi A}{\lambda} \cos\frac{2\pi}{\lambda}(x + v_w t)$$

$$= \pi/2 - I\left(1 + \frac{\eta}{I^2}\right).$$

The integral of the net forward force from Equation 9 (head drag neglected) becomes

$$\bar{F}_x \approx \int_0^\lambda \left[C_{S\perp}^1 I - C_\parallel^1 I \left(1 + \frac{\eta}{I^2}\right)\right] b\,dx$$

$$\approx \left[C_{S\perp}^1 \tilde{I} - C_\parallel^1 \tilde{I}\left(1 + \frac{\eta}{\tilde{I}^2}\right)\right] b\lambda,$$

(17)

where we replace I and I^2 in the integral by their average values $\tilde{I} = \frac{1}{\lambda}\int_0^\lambda |I| dx = \frac{4A}{\lambda}$ and $\tilde{I}^2 = \frac{1}{\lambda}\int_0^\lambda I^2 dx = 2\pi^2(\frac{A}{\lambda})^2$. Applying the constant velocity condition $\bar{F}_x = 0$ allows us to solve for η:

$$C_{S\perp}^1 \tilde{I}\lambda = C_\parallel^1 \tilde{I}\lambda\left(1 + \frac{\eta}{\tilde{I}^2}\right)$$

$$\eta = \left(\frac{C_{S\perp}^1}{C_\parallel^1} - 1\right)\tilde{I}^2$$

(18)

$$= 2\pi^2\left(\frac{C_{S\perp}^1}{C_\parallel^1} - 1\right)\left(\frac{A}{\lambda}\right)^2.$$

In this region of small A/λ (or small η), as A/λ increases, $F_\perp/F_\parallel$ decreases rapidly which competes with increasing $\sin\theta$ and results in the quadratic dependence of η on A/λ.

2.5.2 Region 2

For $0.05 < A/\lambda < 0.15$, η increases substantially and rapidly. In this region as ψ decreases $F_\perp$ increases slowly and $F_\parallel$ is nearly constant:

$$
\begin{aligned}
P_\perp &= \frac{F_\perp}{bd} = C_{S\perp}^2 + C_\perp^2 \psi \\
P_\parallel &= \frac{F_\parallel}{bd} = C_{S\parallel}^2.
\end{aligned}
\tag{19}
$$

In this region, $\eta \approx 0.3$ and the magnitude of θ and ψ are neither close to 0 nor $\pi/2$. To analytically solve for η, a first order Taylor expansion of the tangent function is used though it is a relatively poor approximation (indicated with $*$).

$$
\begin{aligned}
\psi &= \tan^{-1}\frac{v_y}{v_x} - \theta \\
\psi &\approx \frac{v_y}{v_x} - I \qquad\qquad (*) \\
\psi &\approx (\eta^{-1} - 1)I.
\end{aligned}
\tag{20}
$$

The integral of the net forward force becomes

$$
\begin{aligned}
\bar{F}_x &= \int_0^\lambda \left(P_\perp \sin\theta - P_\parallel \cos\theta\right)\sqrt{1 + \tan^2\theta}\, b\, dx \\
&\approx \int_0^\lambda \left[\left(C_{S\perp}^2 + C_\perp^2 \psi\right)|\sin\theta| - C_{S\parallel}^2 \cos\theta\right]\sqrt{1 + \tan^2\theta}\, b\, dx \\
&\approx \int_0^\lambda \left\{\left[C_{S\perp}^2 + C_\perp^2\left(\eta^{-1} - 1\right)I\right]I - C_{S\parallel}^2\right\}\sqrt{1 + \tan^2\theta}\, b\, dx \\
&\approx \left\{\left[C_{S\perp}^2 \frac{4A}{\lambda} + C_\perp^2\left(\eta^{-1} - 1\right)\frac{16A^2}{\lambda^2}\right] - C_{S\parallel}^2\right\} bL,
\end{aligned}
\tag{21}
$$

where we replace I in the integral by its average value $\tilde{I}$ and $L = \int_0^\lambda \sqrt{1 + \tan^2\theta}\, dx$ is the length of the body. Applying the constant velocity condition $\bar{F}_x = 0$ allows us to solve for η:

$$
\begin{aligned}
C_{S\perp}^2 \frac{4A}{\lambda} + C_\perp^2 \left(\frac{1}{\eta} - 1\right)\frac{16A^2}{\lambda^2} &= C_{S\parallel}^2 \\
\eta &= \frac{1}{\frac{C_{S\parallel}^2 - 4C_{S\perp}^2\frac{A}{\lambda}}{16C_\perp^2\left(\frac{A}{\lambda}\right)^2} + 1}.
\end{aligned}
\tag{22}
$$

29

Since $F_\perp/F_\parallel$ decreases slowly, η in this region is more sensitive to variations in $\sin\theta$ and therefore for increasing amplitude, η increases rapidly and approximately linearly.

2.5.3   Region 3

For increasing $A/\lambda > 0.15$, η increases slowly. Here as ψ decreases, $F_\perp$ decreases rapidly while $F_\parallel$ saturates at its maximum since the sides of the dragged rod are nearly parallel to its velocity for a majority of each cycle. This gives

$$P_\perp = \frac{F_\perp}{bd} = C_\perp^3 \psi$$
$$P_\parallel = \frac{F_\parallel}{bd} = C_{S\parallel}^3 + C_\parallel^3 \psi. \tag{23}$$

In this region $\eta \approx 0.7$, and since the amplitude of the undulation (A/λ) is large, $\theta \approx \pi/2$ and $\psi \approx 0$ for most of the cycle (see inset of Figure 15). We use the approximations $\theta \approx \pi/2$ and $\psi \approx 0$.

Starting with the expression for θ given in Equation 3 and noting that $\tan(\pi/2 - \theta) \approx \pi/2 - \theta = 1/\tan\theta$ we approximate θ as follows:

$$\tan\theta = \frac{2\pi A}{\lambda}\cos\frac{2\pi}{\lambda}(x + v_w t)$$
$$\theta \approx \pi/2 - \frac{1}{I}. \tag{24}$$

Similarly with the use of the approximation

$$\tan^{-1}\frac{v_y}{v_x} \approx \frac{\pi}{2} - \frac{v_x}{v_y}, \tag{25}$$

we have

$$\psi = \tan^{-1}\frac{v_y}{v_x} - \theta$$
$$\psi \approx \left(\frac{\pi}{2} - \frac{v_x}{v_y}\right) - \left(\frac{\pi}{2} - \frac{1}{I}\right) \tag{26}$$
$$\psi = \frac{1 - \eta}{I}.$$

The integral of the net forward force becomes

$$
\begin{aligned}
\bar{F}_x &= \int_0^\lambda \left(P_\perp \sin\theta - P_\parallel \cos\theta \right) \sqrt{1 + \tan^2\theta}\, b\, dx \\
&= \int_0^\lambda \left[C_\perp^3 \psi \tan\theta \cos\theta - \left(C_{S\parallel}^3 + C_\parallel^3 \psi \right) \cos\theta \right] \sqrt{1 + \tan^2\theta}\, b\, dx \\
&= \int_0^\lambda \left\{ C_\perp^3 I^{-1}(1-\eta) I \cos\theta - \left[C_{S\parallel}^3 + C_\parallel^3 \frac{1}{I}(1-\eta) \right] \cos\theta \right\} \sqrt{1+\tan^2\theta}\, b\, dx \qquad (27) \\
&= \int_0^\lambda \left[(C_\perp^3 - C_\parallel^3 I^{-1})(1-\eta)\cos\theta - C_{S\parallel}^3 \cos\theta \right] \sqrt{1+\tan^2\theta}\, b\, dx \\
&\approx \left[(C_\perp^3 - C_\parallel^3 \tilde{I}^{-1})(1-\eta)\cos\theta - C_{S\parallel}^3 \cos\theta \right] bL.
\end{aligned}
$$

In the last step I is replaced in the integral by its average value $\tilde{I}$. Applying the constant velocity condition $\bar{F}_x = 0$ allows us to solve for η:

$$
\begin{aligned}
(C_\perp^3 - I^{-1} C_\parallel^3)(1-\eta) &= C_{S\parallel}^3 \\
\eta &= 1 - \frac{4 C_{S\parallel}^3}{4 C_\perp^3 - \left(\frac{A}{\lambda}\right)^{-1} C_\parallel^3}.
\end{aligned} \qquad (28)
$$

Physically, the decrease in $F_\perp / F_\parallel$ competes with the increase of $\sin\theta$ which plateaus for large amplitude (as θ approaches $\pi/2$) which causes η to increase slowly.

Overall, the analytic solution of the RFT correctly predicts that η increases quadratically for small A/λ, increases rapidly for intermediate A/λ and is nearly constant for large A/λ. For each region, the analytical form of η qualitatively agrees with the calculated shape of the η vs. A/λ relationship, see Fig. 15. The solution demonstrates that the difference between swimming in sand and swimming in a low Re Newtonian fluid is predominantly due to the difference in functional forms of $F_\perp$ and $F_\parallel$ in these two media (in addition to the difference that in granular media, forces are speed independent for low speeds, less than $40\,\mathrm{cm/s}$ in our case). In low Re fluids [52], $F_\perp$ and $F_\parallel$ are proportional to their respective projected velocities with coefficients in the ratio $2:1$. In contrast, in granular media, the functional forms of $F_\perp$ and $F_\parallel$ are more complicated and thus the effective coefficient ratio depends on A/λ. The larger slope of $F_\perp$ at smaller ψ (small A/λ) is largely responsible for the increased magnitude of η in granular media relative to that in low Re swimmers like nematodes.

2.6 Discussion and summary

There are some assumptions that have not been validated in the RFT model. We assumed that forces on a segment depend on the local orientation and velocity of that segment and there are no interactions between segments. Another assumption was that all body and head segments encounter material with the same ϕ; that is probably not true because the body encounters grains disturbed by the head and other body segments. However, because $F_\perp$ and $F_\parallel$ scale in the same ratio in all ϕ and this ratio determines η, wave efficiency should be insensitive to ϕ.

In this Chapter, a resistive force theory (RFT) with empirical force laws for granular media from experiment and simulation was developed to explain the swimming performance of the sandfish lizard and predict how amplitude of the undulation affects the swimming performance. Because of the larger perpendicular force $F_\perp$ in granular media, the sandfish can reach a higher wave efficiency ($\sim$0.5) compared to the low Re swimmers. The approximated analytical solution of the RFT further elucidated the relation between shape of the wave efficiency curve and the force profile as a function of ψ. The scaling of the force explained the similar wave efficiency observed in different packing state of the media. By varying the amplitude of the undulation in RFT, I showed that the range of amplitude used by the animal coincides with the maximum speed, which implies that the animal optimizes its speed, in accord with the behavior studied, an escape response.

CHAPTER III

NUMERICAL SIMULATION OF SAND-SWIMMING

3.1 Introduction

We showed that the sandfish lizard can swim within granular media at speeds up to 0.4 body-lengths/cycle by propagating a traveling wave posteriorly along its body (described in Chapter I). We developed an empirical resistive force theory (Chapter II) that predicted the performance of the animal within granular media (i.e. wave efficiency to within 20%) [81]. The RFT predictions are, however, based on several assumptions: the forces experienced by the sandfish are velocity independent, and the average thrust and drag forces can be approximated by steady state forces at a slow speed. Also, the lateral motion and the yaw motion were not considered. These assumptions make study of more detailed mechanics such as flow of the medium and parameter variation difficult or impossible. The kinematics of the animal in RFT is modeled as a simple one period uniform traveling sinusoid, and it is non-trivial to modify the RFT model to incorporate other form of kinematics.

In simulation, we use the multi-body software Working Model to obtain a more flexible model of the locomotor and overcome these problems. We use the discrete element methods (DEM) [100] to simulate the particles because it is more flexible and able to capture many aspects of the dynamics of granular material [38]. An experimentally validated model of the medium thus enables us to examine the dynamics in the media at flow and grain level, obtain the forces on the model sandfish without resorting to use of empirically established force laws, and vary the properties (like grain friction, size and density) of the media directly. Also, with a better understanding of the flow, it is possible to develop better force laws and theoretical models for locomotion in sand.

Using this numerical simulation we investigate the effects of varying kinematics parameters, which can not be controlled in animal experiment, on swimming performance. First we describe the development of the simulation approach and compare its predictions of η to

the animal experiment. We then vary kinematic parameters to systematically demonstrate an optimality condition for undulatory swimming in granular media*. Next we use the simulation to make measurements of mechanics of sand-swimming, including the body velocities, reaction forces from the medium, power, and actuator torque*. Some comparisons with animal experiments or robot experiments will be made when possible. We will also compare the differences and similarities of swimming in granular media to swimming in a fluid.

3.2 Simulating the granular media

As desert sand has a typical grain size of 300 μm, the computational power required to simulate a sand bed with comparable size of a sandfish is far beyond the facilities that are available to us. Therefore we use 3 mm glass beads and 6 mm as model sands for animal simulation and robot simulation, respectively. We observed no differences in the kinematics of the sandfish lizard between 3 mm particles and 300 μm particles and the performance of the animal is similar with different size particles [84]. Therefore we would expect the qualitatively same result if particles with natural grain size were used. The choice of 6 mm plastic particles for robot simulation also has the added benefit that they are less likely to get inside the skin of the robot.

3.2.1 Discrete Element Method

The granular medium was simulated using a custom-written 3D soft sphere DEM code [100]. In DEM simulation, particles are modeled as perfect spheres. To compute particle-particle and particle-intruder interaction forces, we calculate the normal force [73], F_n, and the tangential Coulomb friction force, F_s (see Figure 18) at each contact using

---

*This work has been published in two journal papers: "Mechanical models of sandfish locomotion reveal principles of high performance subsurface sand-swimming," Ryan D. Maladen, Yang Ding, Paul B. Umbanhowar, Adam Kamor, and Daniel I. Goldman, *J. R. Soc. Interface*, 8, 1332-1345, (2011) and "Undulatory swimming in sand: experimental and simulation studies of a robotic sandfish," Ryan D. Maladen, Yang Ding, Paul Umbanhowar, and Daniel I. Goldman, *The Inter- national Journal of Robotics Research*, 30, 7, 793, (2011).

*These results are part of a manuscript in preparation for the Journal of Experimental Biology, "Mechanics of Undulatory Swimming in a Frictional Fluid," Yang Ding, Sarah S. Sharpe, Andrew Masse, Ryan D. Maladen, and Daniel I. Goldman
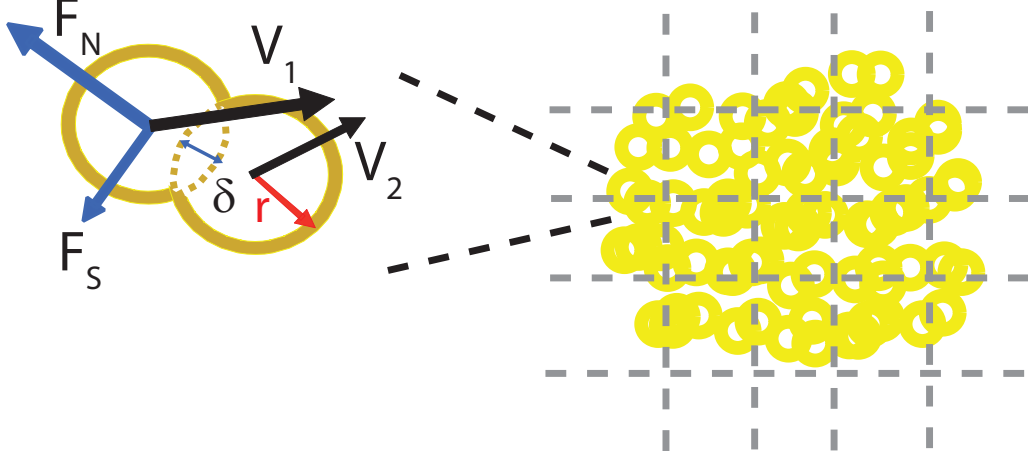
Figure 18: In the discrete element model, each of simulated particle is assigned to a grid based on the position of the particle (right). Forces on two representative contacting particles whose interaction forces are given by Eq. 29. $F_\perp$ and F_S correspond to the normal and tangential forces respectively. δ, r, v_1, and v_2 correspond to the virtual overlap between interacting particles, and the radius and velocities of the particles respectively.

$$F_n = k\delta^{3/2} - G_n v_n \delta^{1/2}$$

$$F_s = \mu_{pp} F_n,$$

(29)

where δ is the virtual overlap between interacting particles, v_n is the normal component of relative velocity, and k, G_n, and μ_{pp} represent the hardness, viscoelastic constant, and the particle–particle friction coefficient respectively (see Table 3 & 4 for specific values). Rotation was not considered.

At each time step δt, the position x, net force F and velocity v of each particle is calculated sequentially:

$$x_i(t) = x_i(t - \delta t) + v_i \delta t$$

$$F_i(t) = F_i(x_{1...n}(t), v_{1...n}(t - \delta t))$$

(30)

$$v_i(t) = v_i(t - \delta t) + F_i \delta t.$$

where i is the index of a particle and t is the time.

Because the force on a particle can potentially result from interaction with any other particles, $N(N - 1)$ pairs of particles need to be considered for the force calculation. To reduce the computational time which has a computational complexity of $O(N^2)$, we use
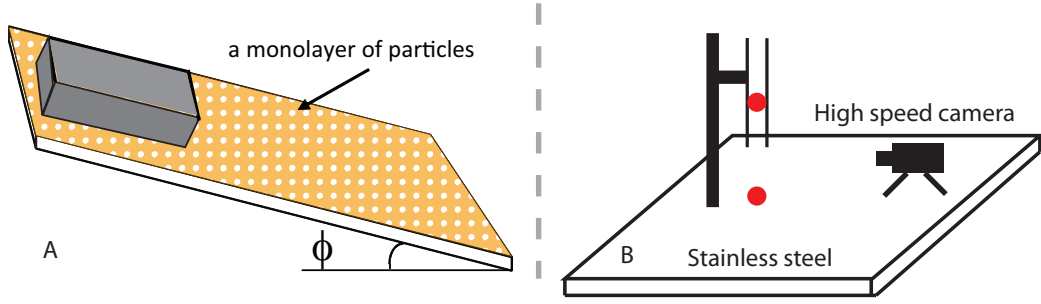
Figure 19: Diagrams of the experiment setups for the friction coefficient (A) and restitution coefficient (B) measurements. In (A), intruders or particle-covered plates were placed on an inclined surface covered a mono-layer of particles. In (B), a particle is dropped from a tunnel to collide with another particle glued to a stainless steel plate.

the popular cell-division algorithm. The space of interest is divided into a uniform grid of cubic cells with edges slightly larger than the diameter of the largest particle. Particles are assigned to the cells based on their position and this list is updated every time step. This space division algorithm ensure that only particles in the same cell or adjacent cells could be in contact. This reduces the computational complexity to $O(N \log(N))$, which significant reduces computational time. The initial volume fraction was prepared by randomly distributing the particles in the volume corresponding to the desired volume fraction and then eliminating particle overlap using the method of [95].

3.2.2   Measurements of the particle and intruder properties

There are three fitting parameters in our force model that determines the mechanical properties of the particle. To estimate friction between particles (both 3 mm glass beads and 6 mm plastic particles), and the friction between various intruders with the particles we measured the angle at which the intruders began to slide on an inclined surface (see Fig. 19). The inclined surface was covered by a mono-layer of either 3 mm or 6 mm particles. The angle of the surface was initially set high so that the intruder did not stop. Then the angle was decreased until the intruder stopped quickly even after a small push and the angle ϕ was recorded. The friction coefficient μ was calculated as $\mu = \tan(\phi)$. We started from a high angle and decreased it rather than started a low angle and increases the angle until the intruder began to slip because the unevenness of the surface may contribute to the resistance of downward motion.

Table 3: Parameters used in simulation and measured from experiments for 3 mm glass particles. PD is the average particle diameter of 3.2 mm. For both 6 mm plastic and 3 mm glass particles (see below) the restitution coefficient was measured for particle-particle collisions with one particle glued to a stainless steel plate and with an impact velocity of 0.48 m/s in experiment and simulation.

	Experiment	Simulation
Hardness (k)	5.7×10^9 kg s^{-2} m$^{-1/2}$	2×10^6 kg s^{-2} m$^{-1/2}$
Restitution coefficient	0.92 ± 0.03	0.88
G_n	15×10^2 kg m$^{-1/2}$ s^{-1}	15 kg m$^{-1/2}$ s^{-1}
$\mu_{particle-particle}$	0.10 ± 0.01	0.10
$\mu_{particle-body}$	0.27 ± 0.01	0.27
Density	2.47 g cm^{-3}	2.47 g cm^{-3}
Diameter	3.2 ± 0.2 mm	3.0 mm (50%) and 3.4 mm (50%)
Granular volume	67 PD $\times$ 56 PD $\times$ 31 PD	109 PD $\times$ 43 PD $\times$ 32 PD

The hardness of the particles k was estimated using the Hertzian contact model [42] with the values of Young's modules from [1]. To reduce computational time, smaller k values were used. k was chosen so that δ is less than 0.2% PD for all conditions, although the actual k values were nearly a factor of 2×10^3 times greater than the simulated values. Doubling k changed measured quantities (resistive forces) by less than 5%. G_n, μ_{pp}, and μ_{pi} were chosen to match experimental measurements of restitution coefficient and friction coefficients. To measure the restitution coefficient, we let two particles have head on collision at $\sim$40cm/s in experiment. One particle was glued to a stainless steel plate, which has a Young's modules 3$\sim$4 times greater than that of the glass and nearly 10 times higher than that of plastics. We assume that the energy loss in the stainless steel plate during the collision was negligible. Another particle was dropped from above from a plastic tunnel and its trajectory was tracked using high-speed camera to obtain the velocity of the dropped particle. Only the runs for which the velocity of rebound particle was within 10° from a vertical line and the collision speed was 40±4cm/s were considered. To capture the diameter variation in experiment, we used a 50%:50% bi-dispersed particle with the same standard deviation of the particle diameter distribution in experiment. The measured values and the values used in simulation are shown in Table 3 and Table 4.

Table 4: Parameters used in simulation and measured from experiments for 6 mm plastic particles. PD is the average particle diameter of 5.87 mm.

	Experiment	Simulation
Hardness (k)	1.7×10^8 kg s^{-2} m$^{-1/2}$	2×10^5 kg s^{-2} m$^{-1/2}$
Restitution coefficient	0.96	0.88
G_n	1×10^2 kg m$^{-1/2}$ s^{-1}	5 kg m$^{-1/2}$ s^{-1}
$\mu_{particle-particle}$ (μ_{pp})	0.07 ± 0.01	0.080
$\mu_{body-particle}$ (μ_{bp})	0.27 ± 0.01	0.27
Density	1.03 ± 0.04 g cm^{-3}	1.06 g cm^{-3}
Diameter	5.87 ± 0.06 mm	5.81 mm (50%) and 5.93 mm (50%)
Granular volume	188 PD $\times$ 62 PD $\times$ 35 PD	188 PD $\times$ 62 PD $\times$ 24 PD

3.2.3 Validating the simulated granular media

The simulated medium composed of 3 mm particles was validated by comparing the forces on a cylindrical stainless steel rod (diameter $=$ 1.6 cm, length $=$ 4 cm and rod-particle static friction coefficient $\mu_{bp} = 0.15$) dragged through it with those measured from experiment (see Fig. 20). The drag tests to validate the simulated media were performed at a constant speed of 5 cm/s with the object's vertical mid-point at depth $d = 7.6$ cm and its long axis perpendicular to the motion direction (see Fig. 20 inset). In experiment, the cylindrical rod was attached to a robotic arm (CRS Robotics) via a thin but stiff supporting rod which moved the intruder at constant depth and velocity. A 6 d.o.f. force sensor (ATI industrial) mounted to the robotic arm measured the drag force. The force on the supporting rod was measured separately and subtracted from the total force on the rod with the object attached to obtain the force on the object alone. The test was repeated three times for each object. The container holding the particles was $35 \times 15 \times 9$ cm^3 in extent. The deviation between experimentally measured and simulated drag force as a function of angle was less than 10%.

To validate the simulated medium composed by 6 mm particles and obtain the values of friction μ_{pp}, hardness k, and viscoelastic constant G_n (see Table 4), we dropped an aluminum ball (diameter 6.35 cm and mass 385 g) into the plastic particles with varying impact velocity ($0.5 - 3$ m/s) in both experiment and simulation, and set grain interaction
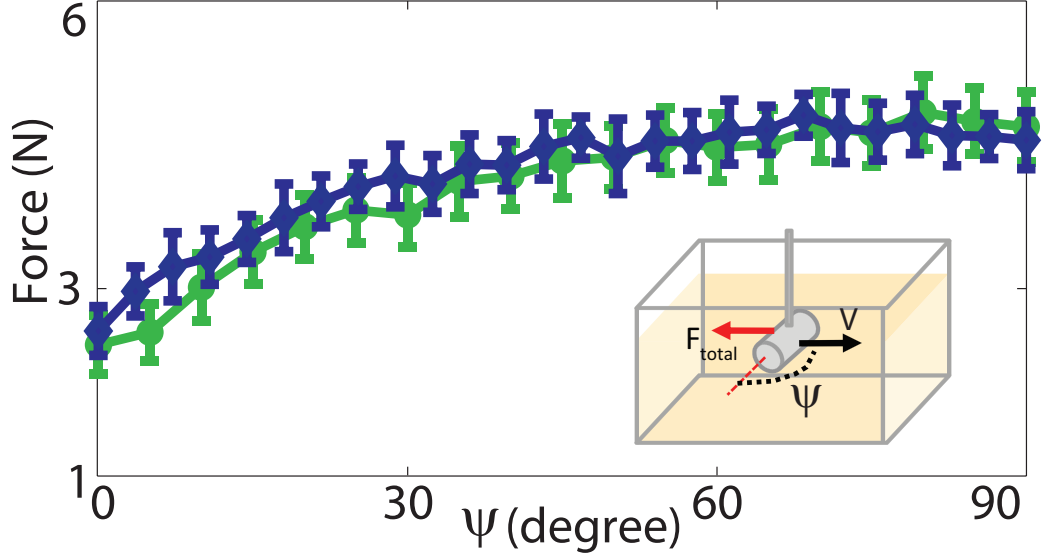
Figure 20: DEM simulation was validated by comparing the forces on a rod dragged through it with those measured from experiment. Total force on a stainless steel rod (sides and ends) (diameter $= 15.8\,\mathrm{mm}$, length $= 40\,\mathrm{mm}$, and rod-particle static friction coefficient $\mu_{bp} = 0.15$) immersed to a depth of $7.62\,\mathrm{cm}$ was measured as a function of the angle (ψ) between the velocity direction and its orientation in experiment (green) and simulation (blue) in a loosely packed medium. The inset shows the experimental setup.

parameters to best match the measured and simulated acceleration of the intruder during the impact collision as a function of time (Fig. 21A)* [48]. With parameters determined from impact at $v = 1.4$ m/s, the force profile fit well at other impact velocities, which is demonstrated by the peak acceleration as a function of impact velocity (Fig. 21B).

3.3 Simulating the sandfish and sand-swimming robots

The multi-segment numerical model of the simulated sandfish and sand-swimming robots were developed using the commercial software package Working Model 2D (Design Simulation Technologies). The multi-body solver was able to calculate the motion of multiple segments connected through joints (actuators). We used the scripting language provided by Working Model. The models were divided into small segments and the segments were connected by joints whose angular position were actuated to generate the desired motion.

We coupled the 2D models in Working Model to the 3D soft-sphere DEM simulation by loading the DEM simulation as Dynamic-link library (DLL). The motion of the animal

---

*Experiments were done by Mateo Garcia, an undergraduate student worked in the Goldman group
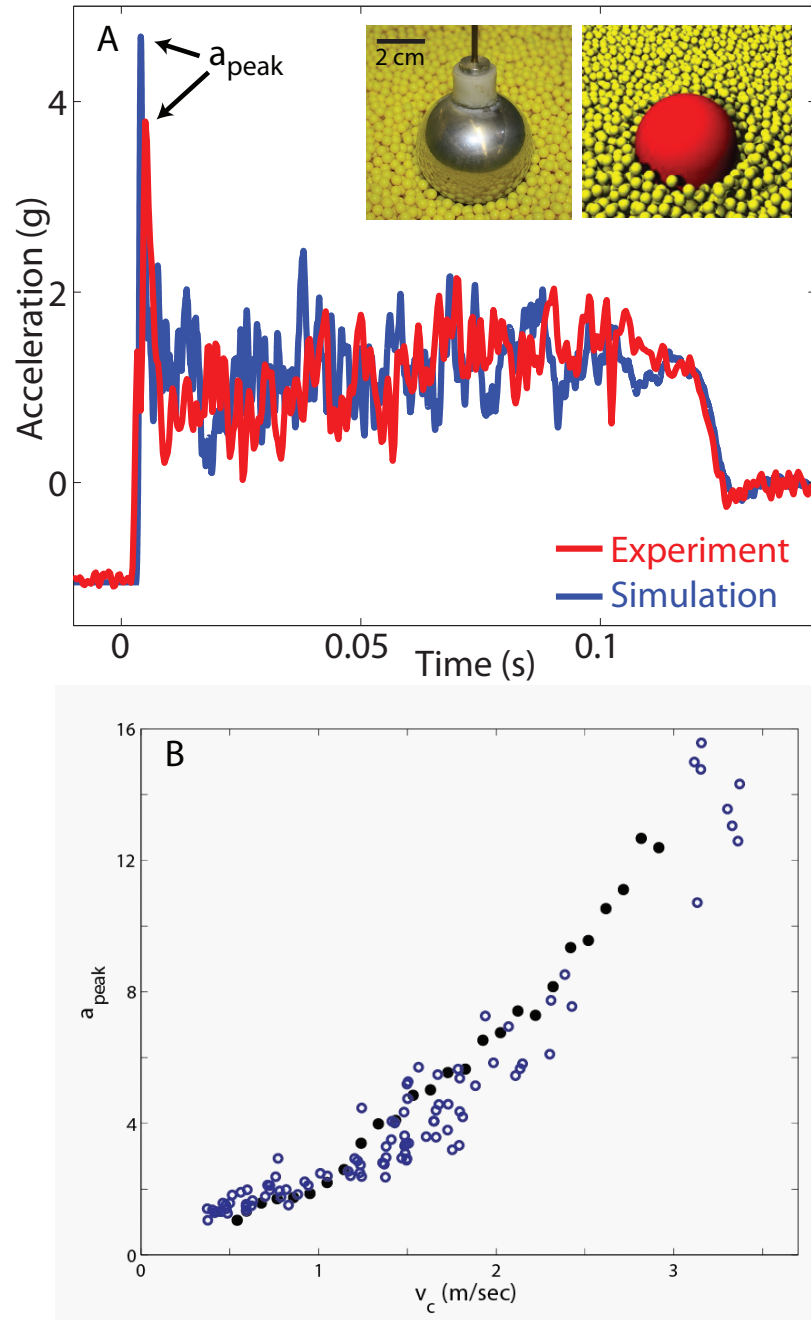
Figure 21: Validation of the discrete element method simulation for the granular medium composed of 6 mm plastic particles using impact experiment of a 6.35 cm diameter sphere. A: The acceleration of the sphere impacted at 1.4 m/s as a function of time is plotted in blue for simulation and in red for experiment. Acceleration is given in units of g, the acceleration due to gravity. (Left inset) Aluminum ball instrumented with accelerometer resting on 6 mm plastic particles. (Right inset) A snapshot of the impact simulation. B: The peak acceleration during the impact as a function of impact velocity v_c. Black solid symbols represent simulation and open blue symbols represent experiment.
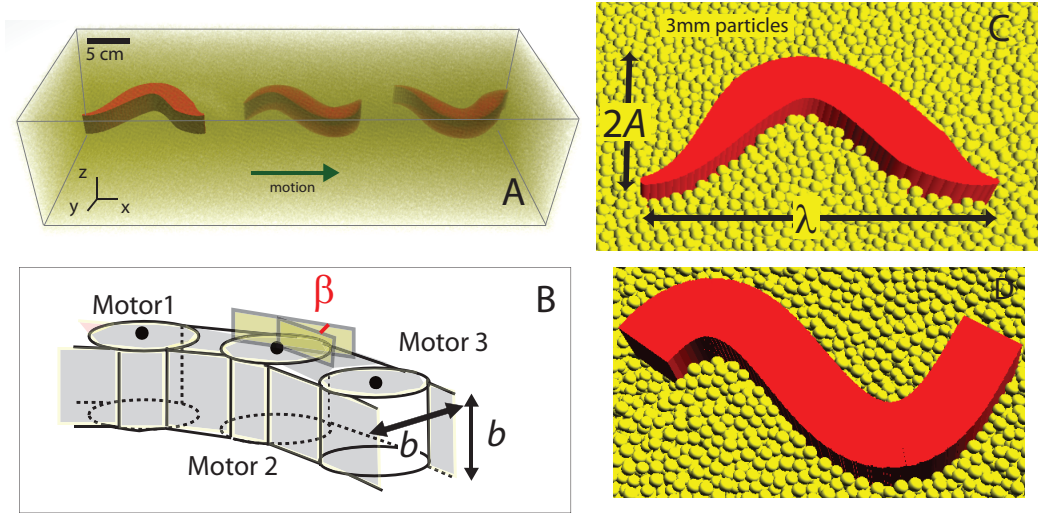
Figure 22: A: 3D view of the simulated sandfish at 3 different instants as it swims within a container of experimentally validated 3 mm glass particles. The particles are rendered semi-transparent for visibility of the model sandfish. B: Inter-actuator connections of a section of the simulated sandfish. b indicates both the width (the maximum along the model) and height of the segments in the non-tapered section of the animal model. The angle between adjacent motors was modulated using Eqn. 31. C & D: Close up view of the simulated sandfish with a tapered body and an uniform square body in 3 mm glass particles. A and λ correspond to the amplitude and wavelength of the simulated sandfish. Particles above the sandfish model are rendered transparent.

model was constrained to prevent rotation of the axis of the traveling wave out of the horizontal plane of motion (roll and pitch). At every time step, the net force on each segments was calculated in the DEM and transferred to Working Model, then Working Model calculated the position and the velocity of each segment and transferred them back to the DEM. The geometries of the segments were defined in the DEM but not considered in Working Model. Interaction between segments due to overlap was not considered.

To compare performance of the numerical simulation to the RFT and capture the shape of the sandfish body, the morphology of the simulated animal was approximated as a tapered tube with rectangular cross-section (see Fig. 22). The width varied uniformly from the snout tip to 1/6 bl, and from 3/5 bl to the tail tip. No tapering in the height of the body along its length was considered as doing so resulted in the model rising as it moved forward due to drag induced granular lift [32]. This lift results from the vertical component of the normal force on an inclined surface dragged through a granular medium and is discussed in Chapter

Table 5: Parameters of the sandfish measured in experiment and used in simulation.

	Experiment	Simulation
Amplitude/Wavelength	0.25 ± 0.05	0.22
Length (Snout to tail tip)	12.8 ± 0.3 cm	12 cm
Weight	16.2 ± 4 g	16 g
Max. diameter	1.63 ± 0.11 cm	1.6 cm

IV and [32, 82]. To study more general mechanics of undulatory swimming in sand as well as to examine the effect of body shape on swimming performance, we developed a flat head sandfish model with uniform body width and height. The tapered sandfish model consisted of 50 segments and the flat head sandfish model consisted of 60 segments. Both models did not include limbs since the sandfish places its limbs along its sides during subsurface swimming [81]. To estimate the magnitude of limb drag, we tested a simulated animal with segments of appropriate length (limbs) placed at locations along the body obtained from animal measurements. We found that with the segments extended perpendicular to the body segment (to which they were attached) η decreased by nearly 15% due to the increased drag force.

Model properties such as animal dimensions and density were taken from biological measurements (refer to Table 5 for values). The segment height and maximum segment width were the same and are denoted by b. For simplicity we used the same normal force parameters for both the particle-particle and body-particle interactions. Each joint angle was constrained so that an approximate sinusoidal wave traveled posteriorly from head to tail (Fig. 22). The angle (β) between segments i and $i + 1$ was varied as

$$
\begin{aligned}
\beta(i,t) = \tan^{-1}\left[\frac{2\pi A}{\lambda}\cos\left(\frac{2\pi}{\lambda}x_{i+1} + 2\pi ft\right)\right] \\
- \tan^{-1}\left[\frac{2\pi A}{\lambda}\cos\left(\frac{2\pi}{\lambda}x_i + 2\pi ft\right)\right],
\end{aligned}
\tag{31}
$$

where A is the amplitude, λ is the wavelength, x_i is the position of the ith segment in the direction of motion, f is the frequency and t is time.

Motivated by animal experiment and to test the results of RFT model and numerical
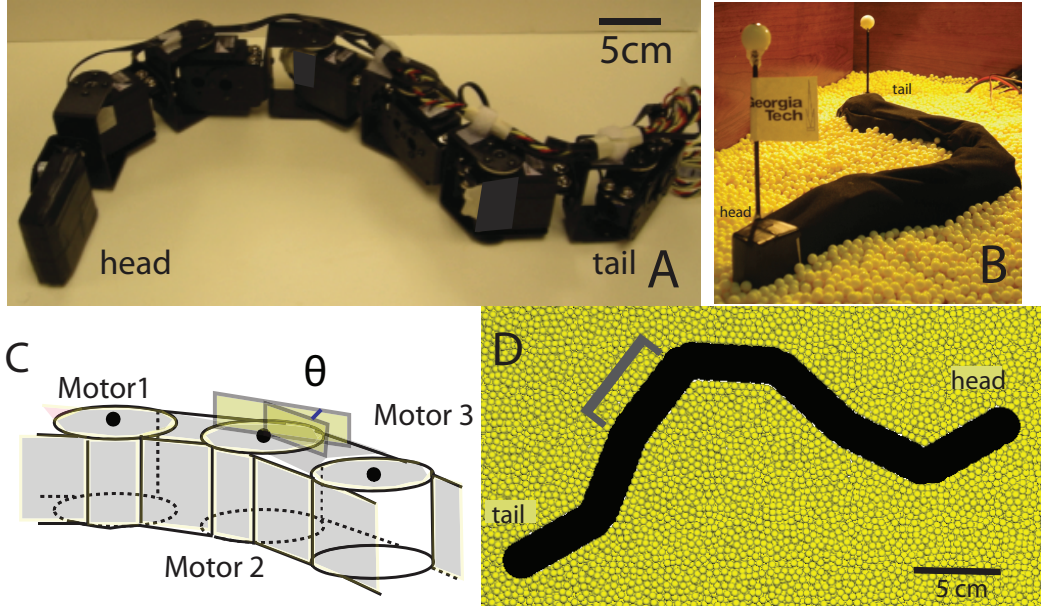
Figure 23: Design of the physical and simulated sand-swimming robot. A: Basic construction (servomotors and aluminum brackets with power wires running along the top of the device). B: The robot with outer layer and masts on the head and tail segments on 6 mm plastic particles. Balls atop the masts are for motion tracking. C: Schematic diagram of a few representative motors (actuators) and elements of the robot modeled with 49 interconnected elements. D: Top view of the simulated robot submerged in 6 mm particles with the particles above the robot rendered transparent. Only every 8th actuator is active while all other actuators are immobilized. The angle between adjacent segment β_i is modulated according to Equation 32 to approximate a sinusoidal traveling wave kinematics ($i = 1$ refers to the head). The particles have been rendered semi-transparent for visualization. The gray brackets ([ ) indicate a single robot segment.

simulation, we developed a 7-segment robot that swims in 6 mm particles [82] [†]. The simulated robot consisted of 49 cuboid interconnected segments and actuated motors (vertical cylinders) of the same height (Fig. 23). Depending on the number of segments (N) to be employed, every $48/N$ actuator (motor) was driven with an open loop signal to generate a sinusoidal wave traveling posteriorly from head to tail while the remaining actuators were immobilized to form a straight segment of length $48 / N$ cm. Preliminary tests of the robot revealed that the angle between adjacent segments was prescribed as

$$\beta(i,t) = \beta_0 \xi \sin(2\pi\xi i/N - 2\pi f t), \tag{32}$$

where $\beta(i,t)$ is the motor angle of the ith motor at time t, β_0 is the angular amplitude, ξ is the number of wavelengths along the body (period), and N is the number of actuators. We use this traveling wave rather than the sinusoidal traveling wave used for the animal simulation (Equation 31) because the kinematics prescribed by the sinusoidal traveling wave are accurate only for low amplitudes, due to the finite segment length associated with a finite number of segments (fixed total length).

3.4   Results

3.4.1   Average swimming speed

Since in the biological experiments the sandfish swam within both 300 μm and 3 mm sand with a single period sinusoidal wave with a typical amplitude of $A/\lambda = 0.22$, we first fixed the amplitude of the model sandfish to $A/\lambda = 0.22$ and varied the oscillation frequency f, and measure the resulting forward speed v_x. The forward speed of the simulated sandfish increased linearly with oscillation frequency, which is consistent with the animal experiments and RFT prediction (see Fig. 24A). The slope of this relationship is the wave efficiency η (Fig. 24A inset). We observed little differences between closely packed media and the loosely packed media and the predicted η values from simulation were close to those observed for the animal. Hence we used loosely packed media for the study reported in the rest of this

---

[†]The development was done by Ryan D. Maladen, a then PhD Bioengineering student in the Goldman group.
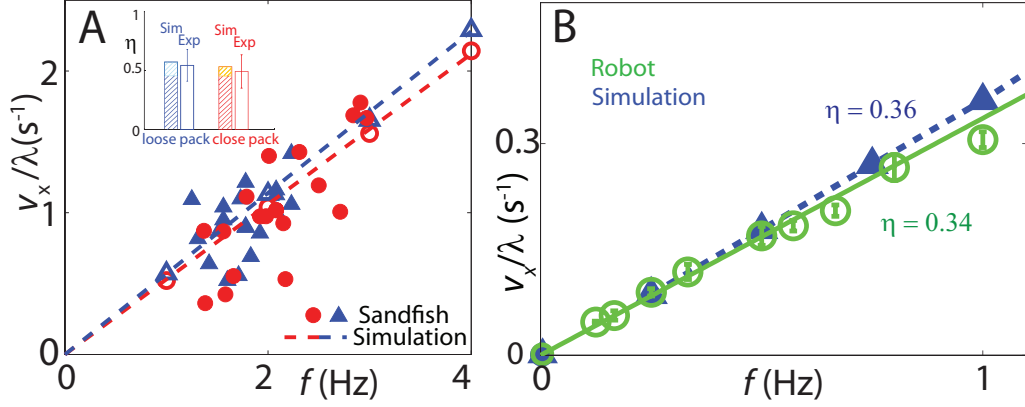
Figure 24: A: Average forward speed vs. undulation frequency as the sandfish swam within 3 mm glass particles. Solid symbols refer to biological measurements, and the dashed lines with open symbols correspond to simulation predictions, respectively. inset: Wave efficiency η, the ratio of the forward swimming speed to the wave speed as determined from the slope of v_x/λ vs. f relationship for biological data and numerical simulation. For the simulation, the lower and higher limits of the η deviation (cyan and orange thatch) correspond to flat and tapered head shapes, respectively. Blue and red colors in correspond to loosely and closely packed media preparations, respectively. B: Forward velocity vs. oscillation frequency relationship for the robot in experiment (green circles) and simulation (blue triangles) ($A/\lambda = 0.2$ and $\xi = 1$). The slope of the dashed (simulation) and solid (experiment) fit lines gives wave efficiency η of 0.36 and 0.34, respectively.

chapter.

The temporal characteristic of the simulated robot quantitatively matched the robot experimental results (Fig. 24B). The forward speed of the robot increased linearly with oscillation frequency. The wave efficiency was $\eta = 0.36 \pm 0.02$, less than that of the sandfish lizard. Increasing N (for a fixed length device) in the robot simulation caused the robot to advance more rapidly and with greater wave efficiency until $N \approx 15$ above which η remained constant at 0.54 (approximately that of the animal) (Fig. 26). We hypothesize that the increase in η with increasing N is due to a smoother body profile which facilitated media flow and led to decreased drag and/or a decreased variation in the spatial form (A/λ) from the prescribed sinusoidal target (as much as 30% for $A/\lambda = 0.2$ for $N = 7$, measured using video of the robot undulating on a flat surface). This result suggests that near maximal performance occurs when the spatial form of the robot reproduces a sinusoidal traveling wave with minimal deviation.

The wave efficiency η for the biological sandfish in 0.3 mm particles and 3 mm particles
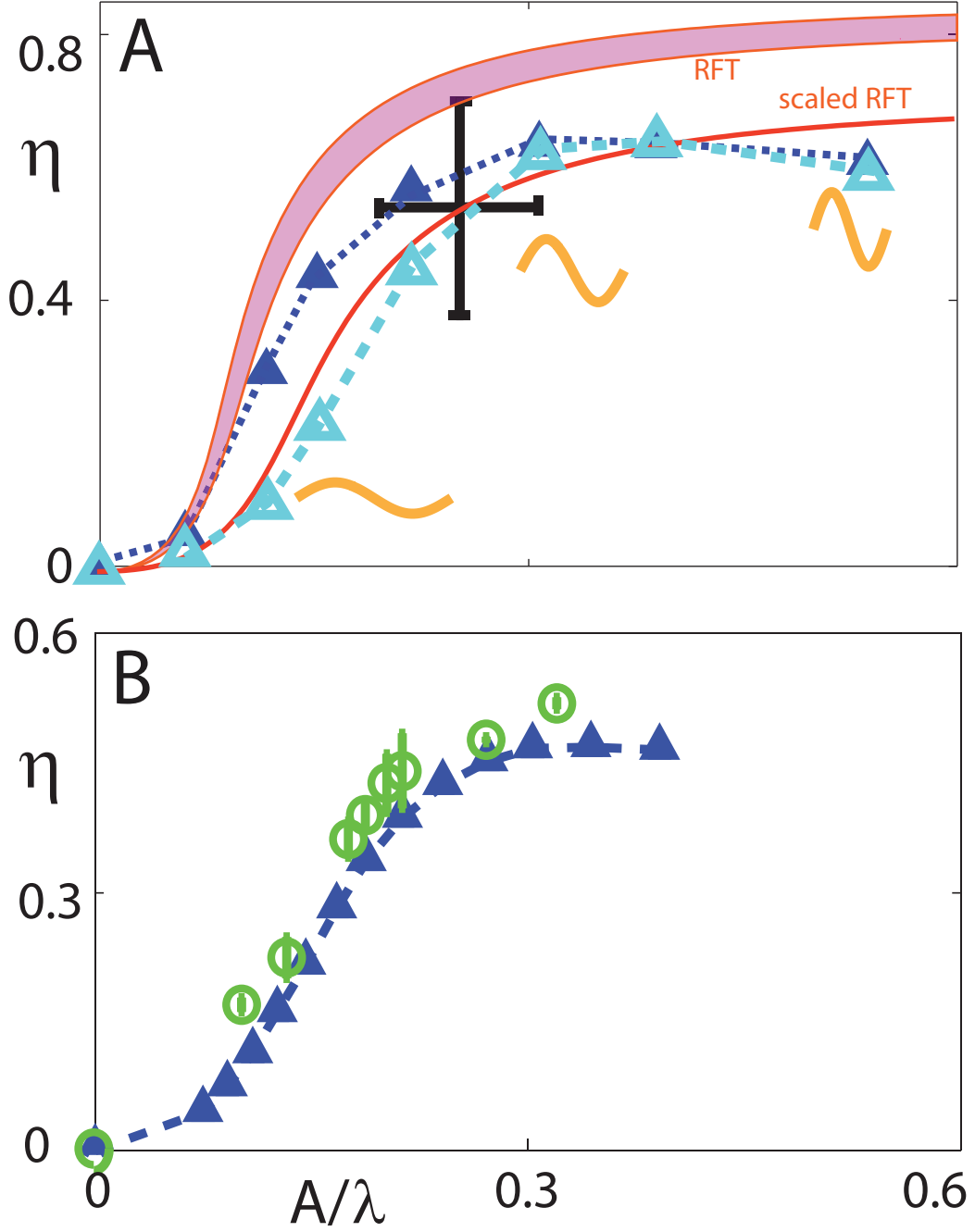
Figure 25: A: Effect of varying A/λ on η of the simulated sandfish within 3 mm glass particles. The cyan and blue dashed curves with triangles correspond to the sandfish simulation with uniform body and tapered body, respectively. The pink shaded region corresponds to the RFT prediction for uniform body for maximum (flat plate, lower bound) and 30% of the maximum (higher bound) head drag. The red curve is the RFT prediction of forward speed for a uniform square body with maximum head drag with the net force on each element scaled by 0.5 (see text). The black cross corresponds to the animal experiment. $\xi = 1$ and $f = 4$ Hz. B: Effect of varying A/λ on η of the robot (green circles) and simulated robot (blue triangles) within 6 mm plastic particles. $\xi = 1$ and $f = 0.5$ Hz.
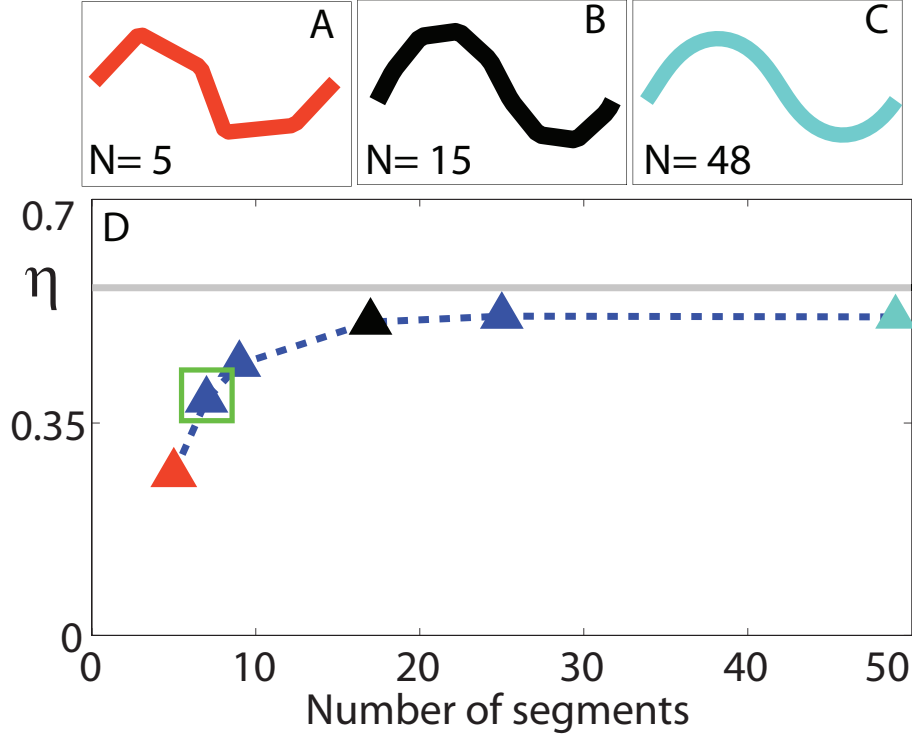
Figure 26: Effect of number of segments on the wave efficiency η for a fixed length robot in simulation (blue dashed curve) ($f = 1$ Hz and $A/\lambda = 0.2$). The red, black, and cyan triangles correspond to 5 (A), 15 (B), and 48 (C) segment robots respectively. The green square corresponds to the number of segments used in the physical robot, and the gray line indicates η predicted by the RFT solved for a continuous body profile (see [49] for details).

with different volume fractions, the numerical sandfish in 3 mm particles, and the simulated 49-segments robot in 6 mm particles are all close to 0.5. This suggests that maximal performance of subsurface locomotion in granular media is not sensitive to changes in media properties like particle size, and density.

3.4.2 Effect of friction on sand-swimming performance

The performance of a sand-swimmer depends on the thrust and drag forces generated by the body. Both of these forces are sensitive to particle-particle friction (μ_{pp}) and body-particle friction (μ_{bp}). We used the simulation to investigate the effect of varying each of these frictions while keeping the other one fixed on forward sand-swimming speed. We found that the speed of the simulated sandfish decreased with increasing μ_{bp}, but increased with increasing μ_{pp} (see Fig. 27). We attribute the decrease of swimming speed to the increase of drag on the body of the model sandfish because the frictional forces on the segments
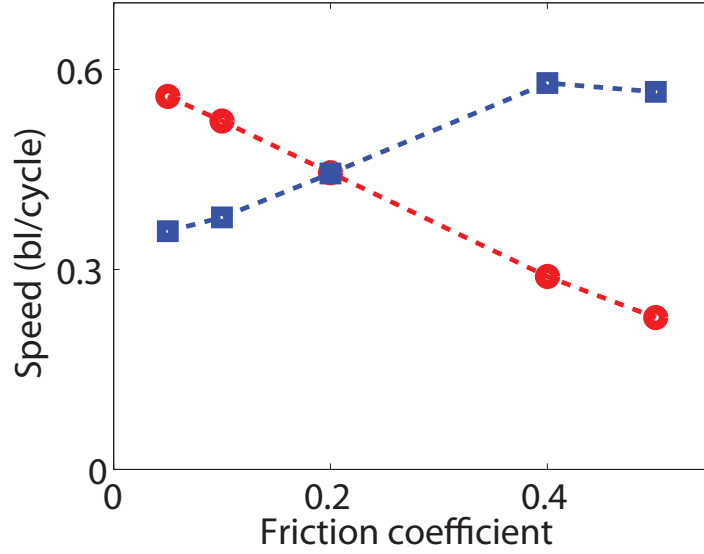
Figure 27: Forward speed of simulated sandfish in $3\,\mathrm{mm}$ glass particles was measured as body-particle friction ($\mu_{pp} = 0.1$, red trace) and particle-particle friction ($\mu_{bp} = 0.27$, blue trace) were varied.

determine the parallel force $F_{\parallel}$ and hence the drag on the body. We hypothesize that the increase of η as particle-particle friction coefficient increased was a result of an overall increase in magnitude of $F_{\perp}$ or a more rapid increase of $F_{\perp}$ at low ψ.

3.4.3 Optimal waveform for sand-swimming speed

We investigated the sand-swimming with parameters used by the sandfish, a sinusoidal traveling wave with fixed kinematics ($A/\lambda = 0.22$ and $\xi = 1$). We now use the numerical simulation to investigate how sand-swimming performance depends on variation of the spatial form of the sinusoidal wave. This allows us to explain or provide hypotheses for why the animal utilized only a limited range of A, λ, and ξ.

We varied A/λ for a single period wave along the body of the simulated sandfish and measured the corresponding η (see Fig. 25). Consistent with RFT prediction, for a given oscillation frequency, η increased quadratically for small A/λ, increased rapidly for intermediate A/λ, and varied slowly for large A/λ. While the shapes of the curves are similar between RFT and simulation, the RFT predictions (for the square cross-section and for the reduced head drag) systematically overestimate η. However, scaling the thrust force

on each element (excluding the head) by a factor of 0.5 in the RFT prediction results in a curve that closely matches the non-tapered simulation (Fig. 25A).

The numerical sandfish simulation displayed a maximum in the forward progress per cycle at $A/\lambda \approx 0.2$ ($\xi = 1$, see Fig. 28), and was close to the prediction from the RFT (see Chapter II). Like the plot of η vs. A/λ, we observed deviation between speed predicted by the RFT and numerical simulation. The biological data resides at the peak of the curve, indicating that the animals could be optimizing their sand-swimming speed. This result agreed with the biological hypothesis that sandfish burial is an escape response [7].

We systematically varied A/λ for $f = 0.5\,\text{Hz}$ and measured the wave efficiency of the robot as it swam subsurface. For all A/λ tested, there was good agreement between η measured in experiment and in the numerical robot simulation. Although η corresponding to an $A/\lambda = 0.2$ was lower than what was measured in the biological experiment, and the numerical sandfish simulation, the shape of the η vs. A/λ relationship remained qualitatively the same.

To test the effect of number of wave periods on performance, we fixed $A/\lambda = 0.2$ and varied $0.6 < \xi < 1.6$. Testing was possible over only a limited range for the physical robot because for $\xi < 0.6$ the side walls of the test container interfere with the motion due to the large amplitude of undulation of the robot, and for $\xi > 1.3$ the maximum angle required to maintain $A/\lambda = 0.2$ exceeds the range of motion of the servomotors. We found that the simulated sandfish, physical robot and the simulated robot all progressed forward fastest for approximately a single period along its body (Fig. 29). We can understand the dependence of speed on ξ by the following argument. For non-integer ξ the sandfish model experienced an unbalanced torque that resulted in a periodic yawing motion (with an amplitude of more than $40°$ for $\xi = 0.5$), which caused A to become effectively smaller and which resulted in lower η and lower v_x. For $\xi > 1$, decreased v_x resulted from a lower η due to the decrease in A required to keep A/λ fixed.
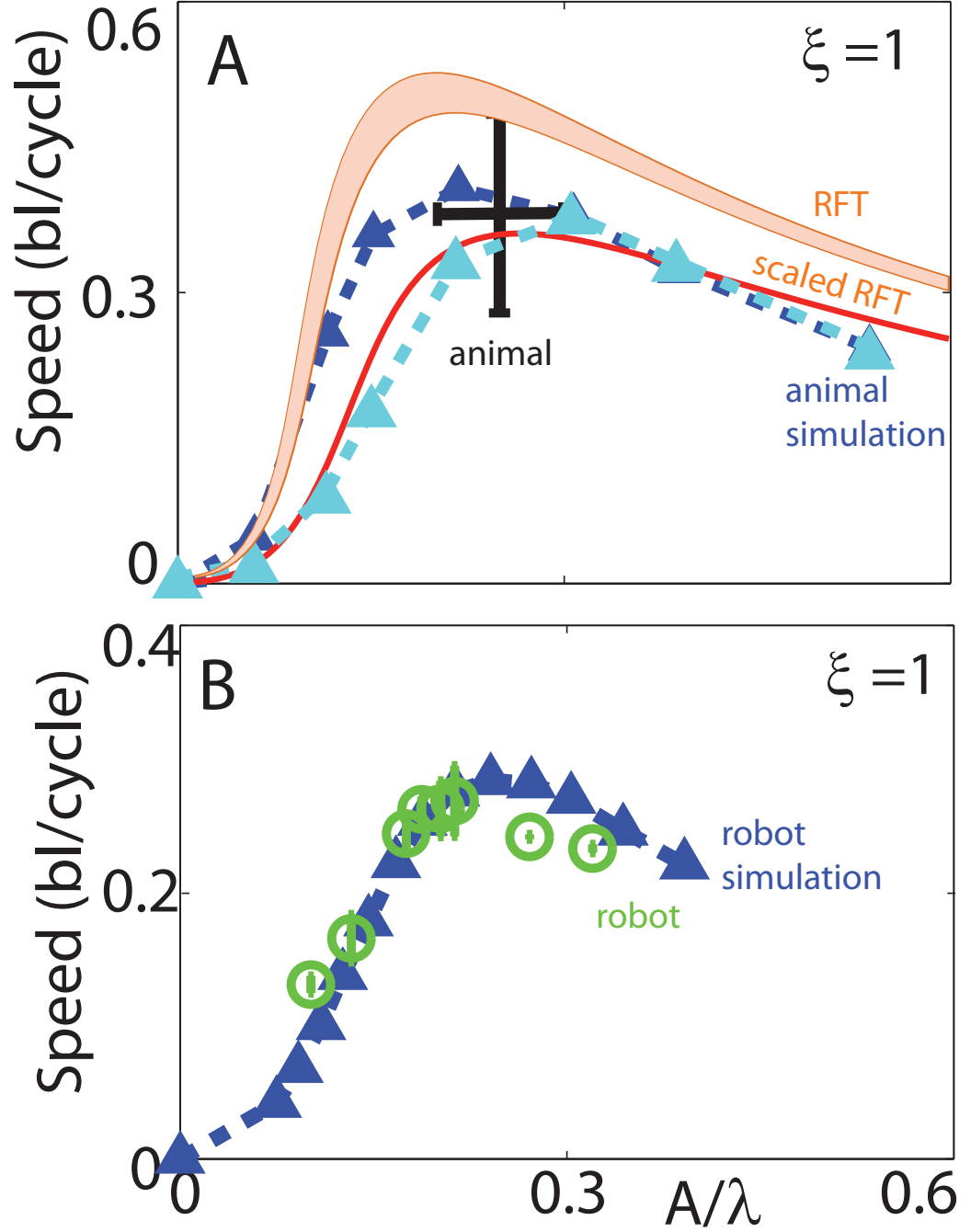
Figure 28: A: Effect of varying A/λ on swimming speed (body-lengths/cycle) of the simulated sandfish within 3 mm glass particles. The cyan and blue dashed curves with triangles correspond to the sandfish simulation with uniform square body and tapered body, respectively. The pink shaded region corresponds to the RFT prediction for square cross-section body for maximum (flat plate, lower bound) and 30% of the maximum (higher bound) head drag. The red curve is the RFT prediction of forward speed for a uniform square body with maximum head drag with the net force on each element scaled by 0.5. $\xi = 1$ and $f = 4$ Hz. Black cross corresponds to measurements from animal experiment. B: Effect of varying A/λ on the swimming speed of the physical (green circles) and simulated robot (dashed blue curve with triangles). $\xi = 1$ and $f = 0.5$ Hz.
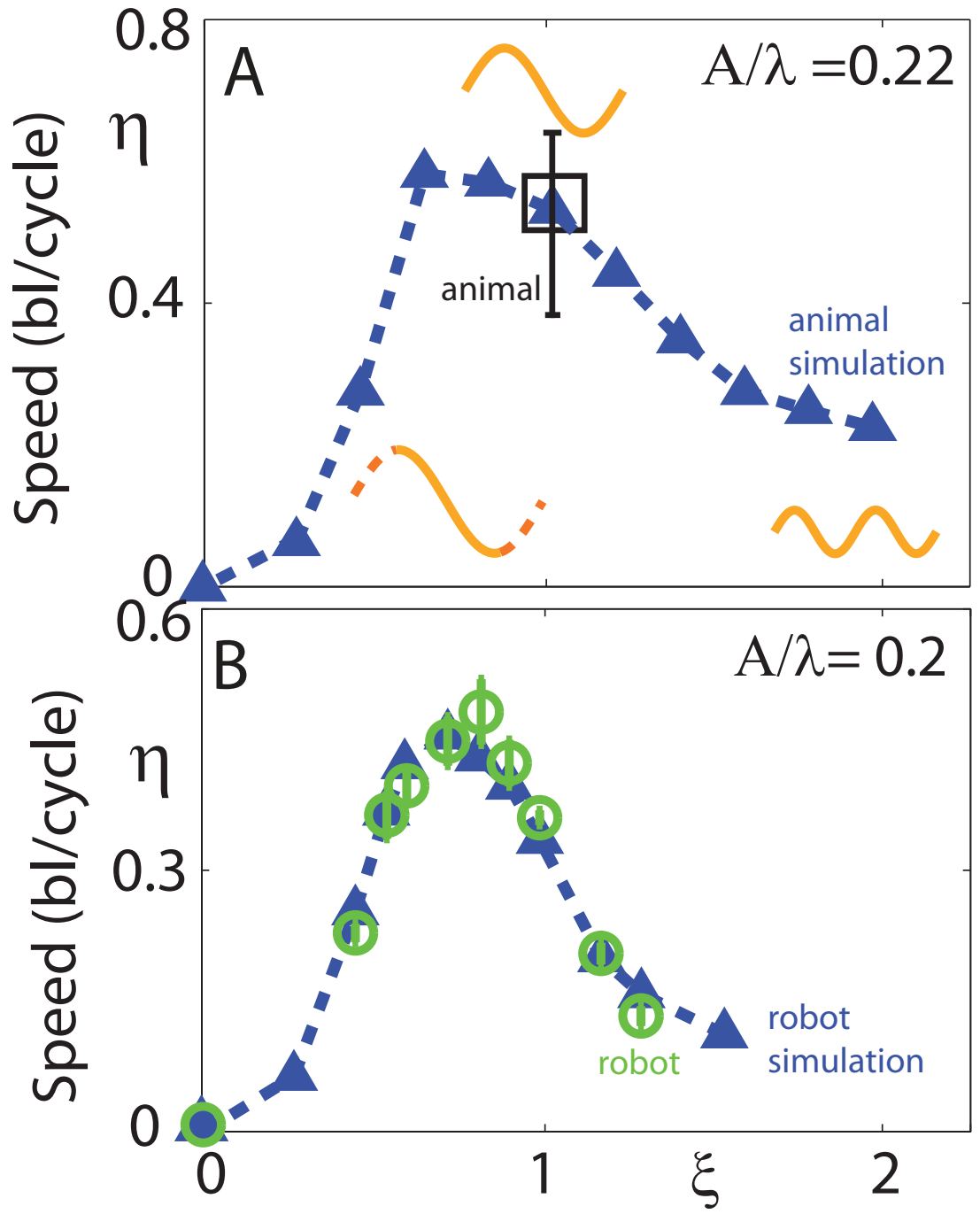
Figure 29: Speed (body-lengths/cycle) vs. ξ relationship identified the kinematics that maximized forward swimming speed for $A/\lambda = 0.2$ for the (A) simulated sandfish in $3\,\text{mm}$ particles with $f = 4$ Hz. and (B) physical (green circles) & simulated (dashed blue curve with triangles) robot in $6\,\text{mm}$ particles with $f = 2$ Hz. A: Black open box corresponds to the single period wave observed in animal experiment. Spatial forms are depicted by orange curves.

51
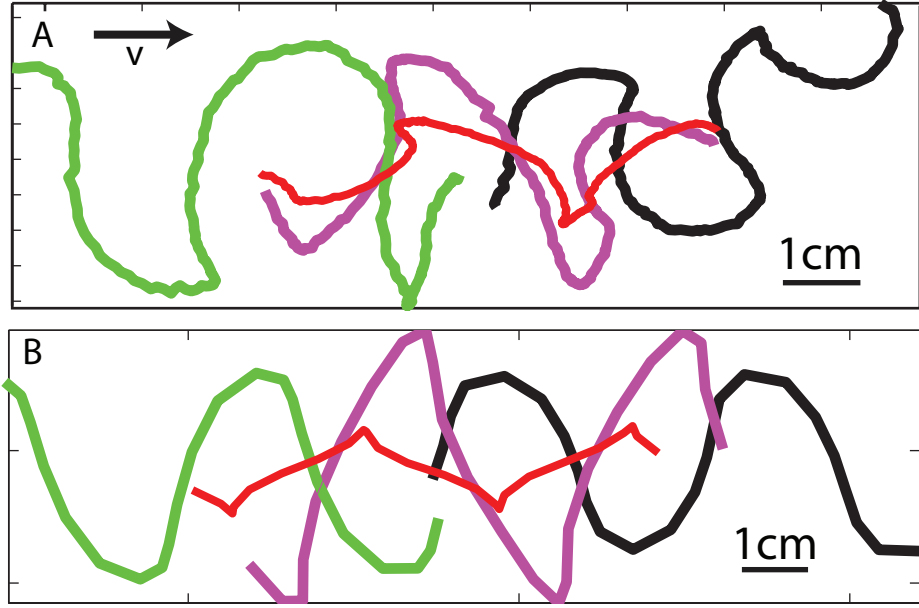
Figure 30: The trajectories of three segments near the head (black), middle of the body (magenta) and tail (green) from experiment (A) and simulation (B). The markers in experiment are located at 19%, 44%, and 69% of the total body length measured from the head to the tail tip and the 10th (16%), 25th (42%) and 45th (75%) segment are chosen as counterparts in simulation. The red line represents the average position of all markers in experiment and the average position of segments between 10th and 45th segments in simulation.

3.4.4   Detailed kinematics

In the previous subsections, we mainly considered a body shape which approximated the tapered shape of the sandfish. We also showed that the model sandfish with a uniform body of fixed width and height, and with flat ends resulted in increased head drag and a smaller swimming speed compared to the tapered model. Otherwise, all the results in previous sections (and following sections as well) are qualitatively the same for a tapered body or uniform body. Hence we only reports results from a uniform body; we will point out the differences in respective places. Two wave amplitudes $A/\lambda = 0.22$ and $A/\lambda = 0.06$ are tested in simulation, and we will refer to them as "animal amplitude" and "small amplitude" hereafter.

The kinematics during swimming result from the coupling between the prescribed body deformation and reaction forces from the media. Because the body motion is described by a traveling sinusoidal wave, each segment would follow a sinusoidal trajectory if the body

moved only in forward direction at a constant speed. However, because of the coupling between the segment motion and body motion, including fluctuations in forward speed, the segment trajectories in the lab frame are distorted traveling waves whose shape depends on the position on the body. Figure 30 shows the trajectories of three representative segments from animal experiment and simulation. In experiment, lead markers were placed on the animal and the trajectories of the segments were obtained from a representative high speed x-ray video of the sandfish lizard swimming in 300 μm glass particles [‡]. Because the animal swam at an angle ($\approx 23°$) into the medium, the trajectories from experiment have been scaled by $\cos^{-1}(23°)$ for comparison. The trajectories of segments from simulation show similar pattern as the trajectories of the lead markers on the animal body. The significant discrepancy near the end (right) is likely because the animal turned and stopped in experiment.

We characterize the undulatory amplitude of a segment by calculating root mean square (RMS) of the lateral displacement y_{RMS}, which is shown in Figure 31. For both low amplitude and animal amplitude (Fig. 31A), y_{RMS} show a high-low-high-low-high pattern as a function of position along the body. The amplitude is larger near the middle and two ends and has two local minima near 20% and 80% points of the total body-length. We also observed the high-low-high-low-high pattern in experiment although the the average magnitude of y_{RMS} was smaller and there was an increasing trend in from from head to tail. We found these features could be captured by using a smaller amplitude $A/\lambda = 0.16$ and an entry angle of of 22° in simulation (see Fig. 31B).

3.4.5 Forces

Overall, the forces predicted by the empirical force laws used in RFT model predicted the direction of the forces and the spatial pattern of thrust and drag forces on the simulated sandfish (see Fig. 32A): The force on a segment was always in the opposite direction of the velocity of the segment (blue arrows in Fig. 32A). The forces on the model sandfish did not change significantly for frequencies less than 4 Hz, which is consistent with the RFT

[‡]The experiment was done by Sarah Sharpe, a bioengineering graduate student in the Goldman group. See [110] for details about the experiment
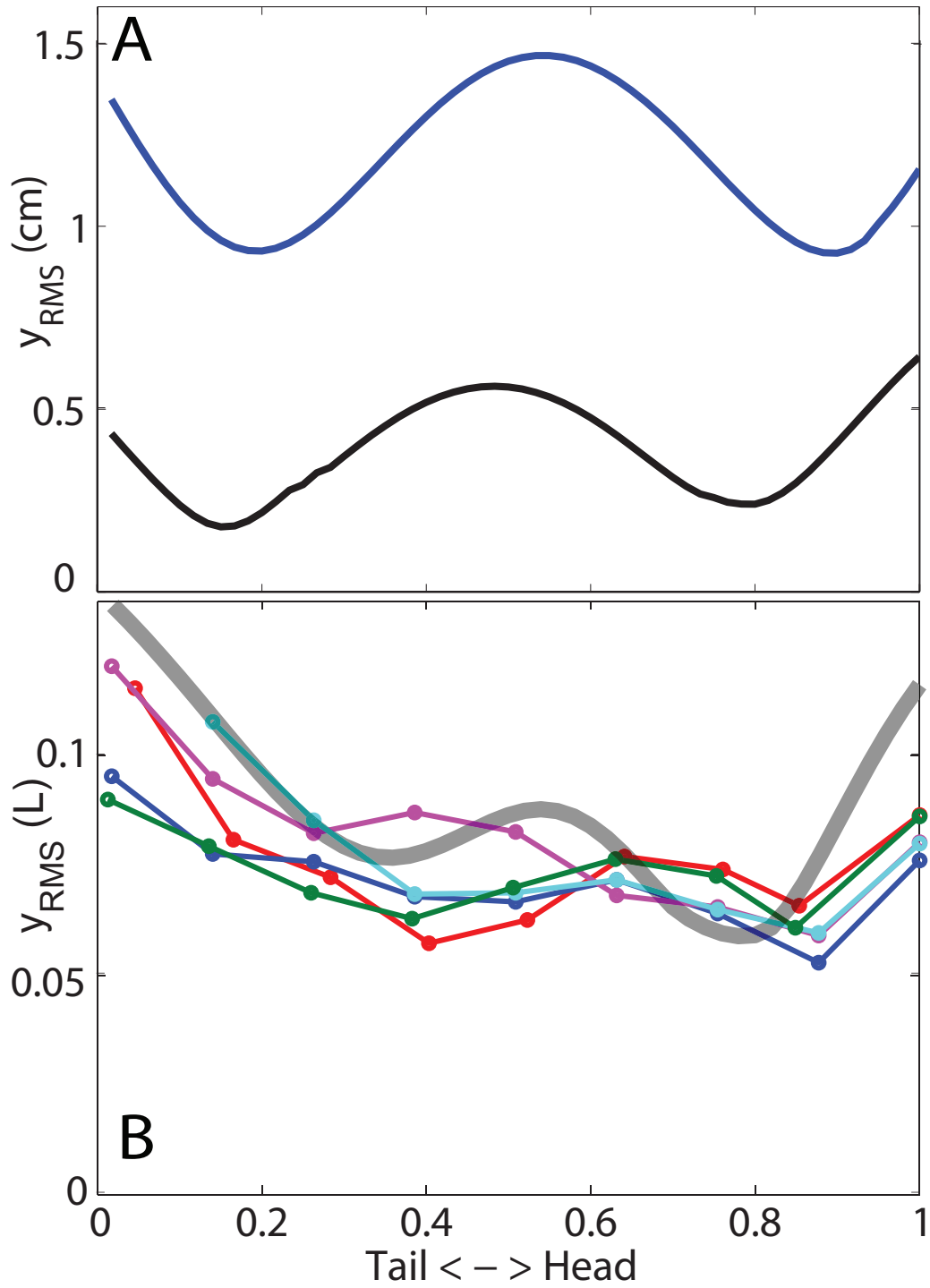
Figure 31: A: The Root Mean Square of the lateral displacement of a segment normalized to the total body length (defined as the length from snout to tail tip) as a function of position on the body from experiment (colored lines and symbols) and a simulation (thick gray line) with an entry angle of 22° and an amplitude of $A/\lambda = 0.16$. B: The Root Mean Square of lateral displacement of a segment as a function of position on the body of a simulated sandfish diving at 22 degrees. Blue represent animal amplitude and black represent small amplitude.
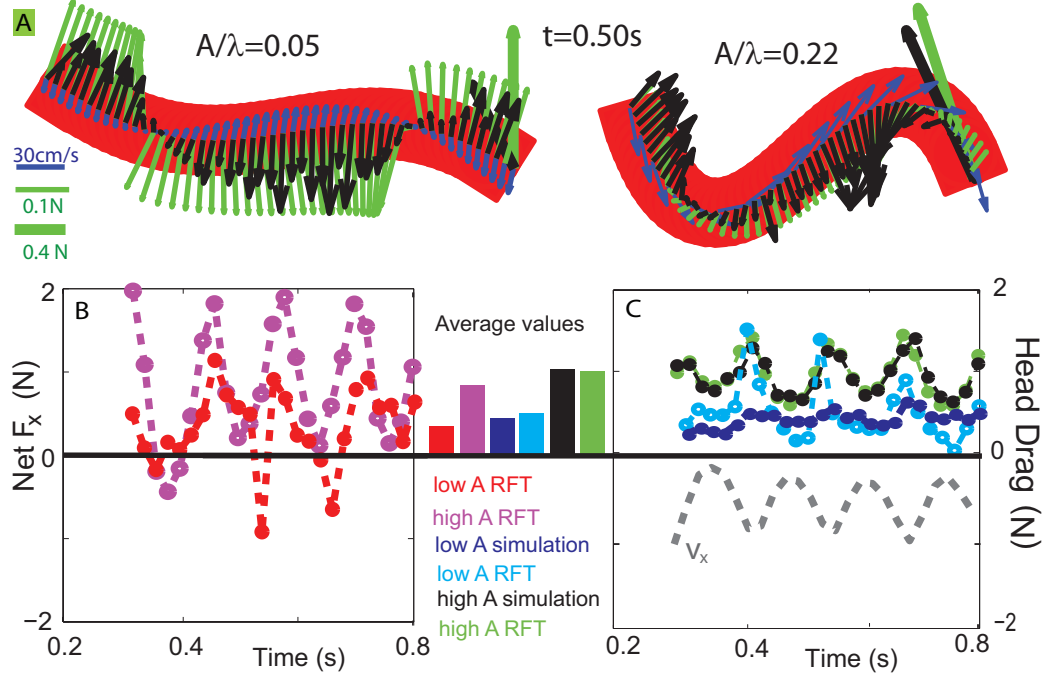
Figure 32: Reaction forces during sand-swimming. A: A snapshot of the reaction force on all the segments. Black represents simulation, green represents the force model prediction in RFT with the small amplitude $A/\lambda = 0.06$ (left) and the animal amplitude $A/\lambda = 0.22$ (right). Blue arrows represents segment velocities. For visibility, every 3rd segment velocities are omitted for the animal amplitude. For visibility, the head drag is scaled by a factor of 0.25 and drawn in thick lines. B left panel: The net force on the body (including head) in the forward direction as a function of time for the animal amplitude (magenta) and the small amplitude (red). C: The head drag as functions of time with the animal amplitude (green represents the RFT model and black represents simulation) and the small amplitude (blue represents RFT model and cyan represents simulation). The forward speed for animal amplitude is re-plotted as the gray line to show its relative phase. Bars between B&C: The average values of the net forces and head drag in corresponding colors.

assumption force is independent of speed. For the small amplitude simulations, the forces on the body were mainly lateral and for the animal amplitude, the larger angle between the segments and forward direction resulted in a larger thrust force on the body. For both amplitudes, we observed substantial head drag (the thick lines in Fig. 32A), which was overcome by the thrust generated by the body. On average, the head drag predicted by the force model quantitatively matched the head drag from the simulation (see Fig. 32). The variation in head drag was in antiphase of the variation of the forward speed (dashed grey line in Fig. 32B), which implies that the variation in forward speed was caused by the variation of the head drag. In the small amplitude runs, both the head drag and the thrust from the body were approximately 50% smaller than the forces in the animal amplitude runs.

We observed significant discrepancy in the magnitude of the forces on the body between those from empirical force laws and those from the simulation: the magnitudes of the forces measured in simulation were in general smaller. The differences were the largest near the maximum lateral excursion, where velocity (and force) reversal occurred in lateral direction. As shown in Figure 32B, this overestimation of thrust made the net forward force larger than zero, the value assumed in RFT model and observed in simulation when the steady speed was reached. As the empirical force laws were used in RFT model, this overestimation of thrust force would also occur in RFT model. In RFT model, the speed is solved from the balance of thrust and drag. If the thrust is overestimated, the force balance would be achieved at a speed larger than it should be. In other words, the overestimation of the force magnitude resulted in the overestimation of speed in RFT model.

The forces on the animal model with the tapered body showed a similar pattern: Thrust and drag distributions were qualitatively the same as the animal model with the uniform body (see Fig. 33A). Because the orientation of the surface on the tapered part of the body was not parallel to the axis of the body, forces on both sides of the head contribute to the net force on the head (see Fig. 33B). The head drag for a tapered head, calculated by summing the drag on the tapered segments on the head and shown with thick pink line in Figure 6, is approximately 18% smaller compared to the drag on the blunt head. For the segments
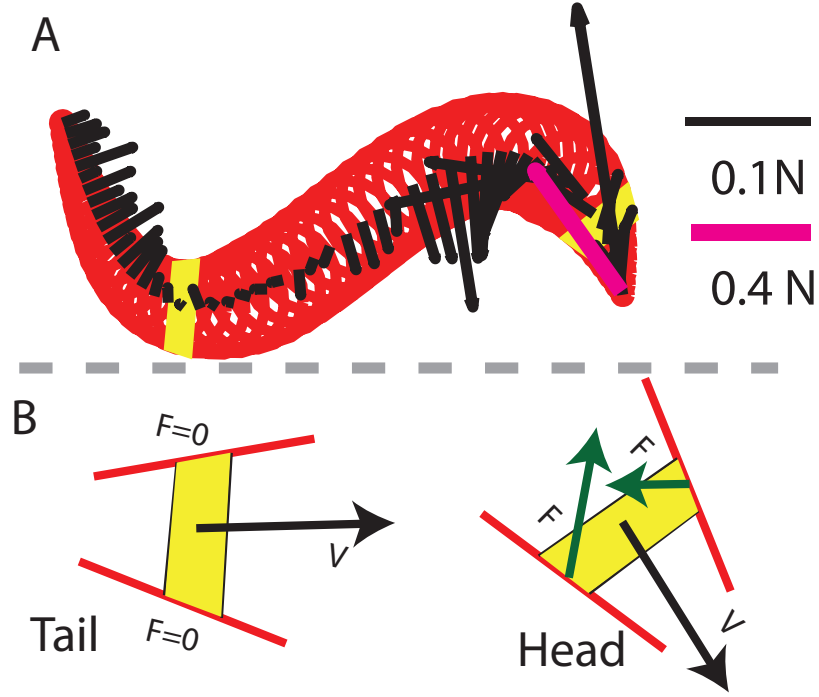
Figure 33: A: A snapshot of the reaction force on segments (black arrows). The pink arrow represents the head drag with a different scale. B: Representative forces on the segments (highlighted with yellow color on the body in A) in the tapered body regions near the tail (left) and near the head (right).

on the tapered tail, the projections of the velocity of a segment might be towards the inner side of that segment on both sides, that is the segment was in the "shadow" of the segments ahead (see Fig. 33B). In such cases, the segments in the "shadows" experienced nearly zero forces. Due to the shape difference, at the animal amplitude, the average speed was observed in the animal model with the tapered body was 30% higher than the non-tapered body.

3.4.6 Actuator Torque

The torque generated by each actuator (τ_i) to follow the designated angle as function of time was measured in Working Model. The actuator torque oscillated at the same frequency of the body undulation but was not sinusoidal and varied with body position as shown in Figure 34A. Therefore, we used root mean square value $\tau_{RMS} = \sqrt{\overline{\tau_i^2}}$ to quantify the magnitude of τ. τ_{RMS} was nearly symmetrically distributed along the body with the maximum torque near the center of the body, resembling a bell shape (Fig. 34B). Because
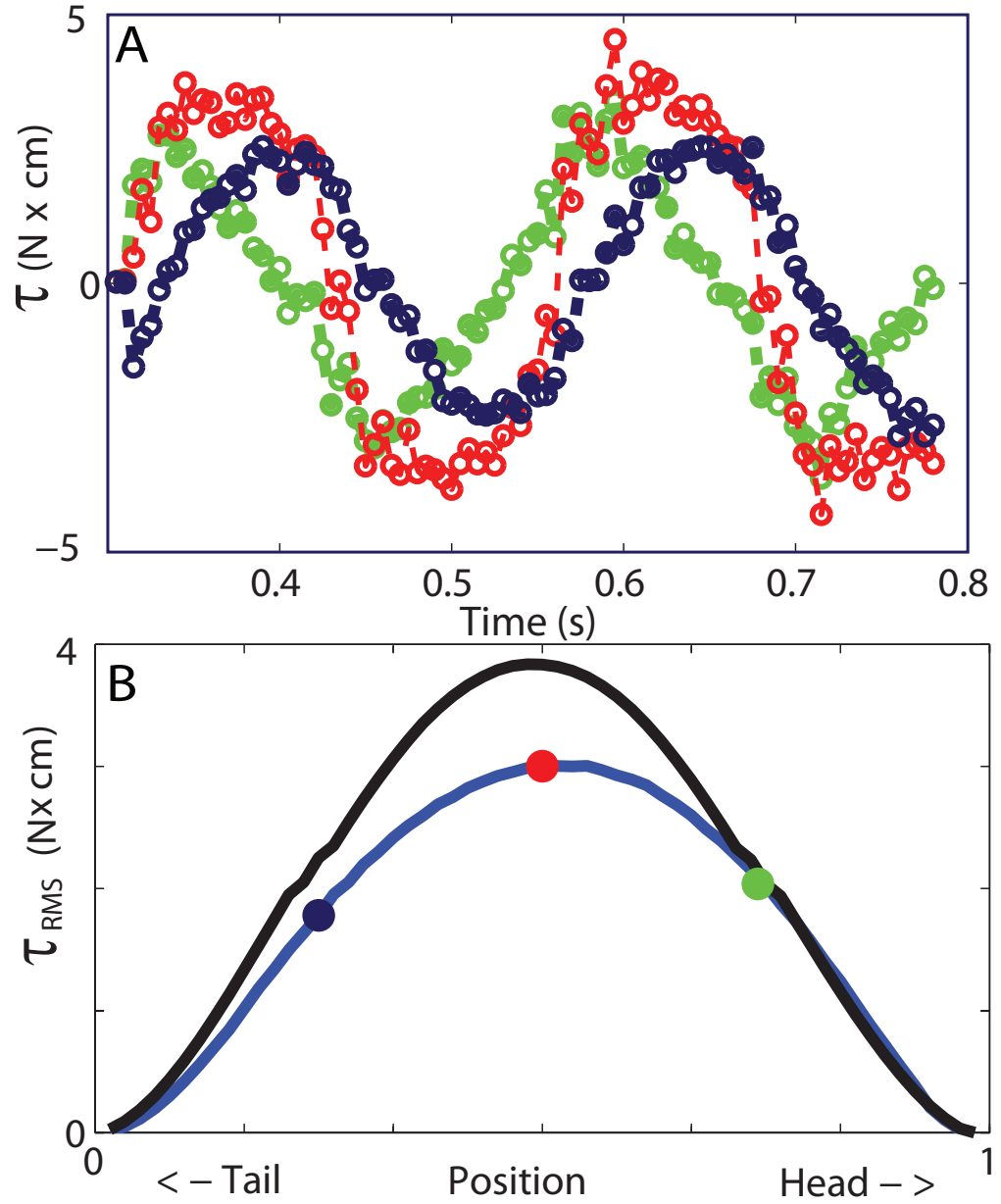
Figure 34: The torque generated by actuators of the sandfish model in simulation. A: The torque generated by actuators at 25%, 50% and 75% of the body (represented by green, red, and dark blue symbols and lines respectively) as a function of time for the animal amplitude. B: RMS of the torque of a actuator as a function of its position on the body for the animal amplitude (blue) and the low amplitude (black). Large filled circles indicate the RMS of the torques curves in panel A with the same color scheme.

the largest portion that could move toward the same side laterally on a traveling sinusoidal wave is half a wavelength, the torque generated by segments with distances larger than half wavelength is likely to be in opposite direction of the torque generated by the segments within the half of a wavelength. The center actuators generate the largest torques because the distances from the center to both ends are half of a wavelength. The magnitude of the torque for the small amplitude is in general larger since the torque arm is larger due to its larger associated wavelength.

3.4.7 Power

The average actuator power also displayed a bell-shape distribution (see Fig. 35A): The central actuators generated most of the power and actuators near the end generated nearly zero or even negative power (dissipation). Energy was generated from the actuators and dissipated to the media through the resistive forces on the segments. From the product of the forces and velocities of the segments, the average dissipation power per unit length along the body was calculated (see Fig 35B). We found that about 30% of the power was used to overcome the head drag for the animal amplitude, and the percentage is smaller for smaller amplitude, which is in accord with the head drag observation. The slower forward speed was also responsible for the smaller energy dissipation on the head for the small amplitude. On the body, power distribution on the segments showed a pattern similar to the amplitude of lateral undulation of the segments. The power was enhanced in the middle and two ends and was reduced near the 20% and the 80% locations along the body (see Fig. 31). Since no significant difference in the magnitude of the force along the body was observed, this indicates that the travel distance in the lateral direction was responsible for the power differences along the body. Inside the granular medium, the energy was dissipated due the interactive forces and relative motion between particles. The random motion of the particles can be measured by the granular temperature [65]. We use the definition of granular temperature as $< (u- < u >)^2 >$ as in [15], where u is the particle velocity and "$<>$" means averaging over 3 cm (W) $\times$3 cm (L) $\times$1.6 cm (H) cells whose centers are at the same depth of the center the model sandfish. We found that the high temperature regions
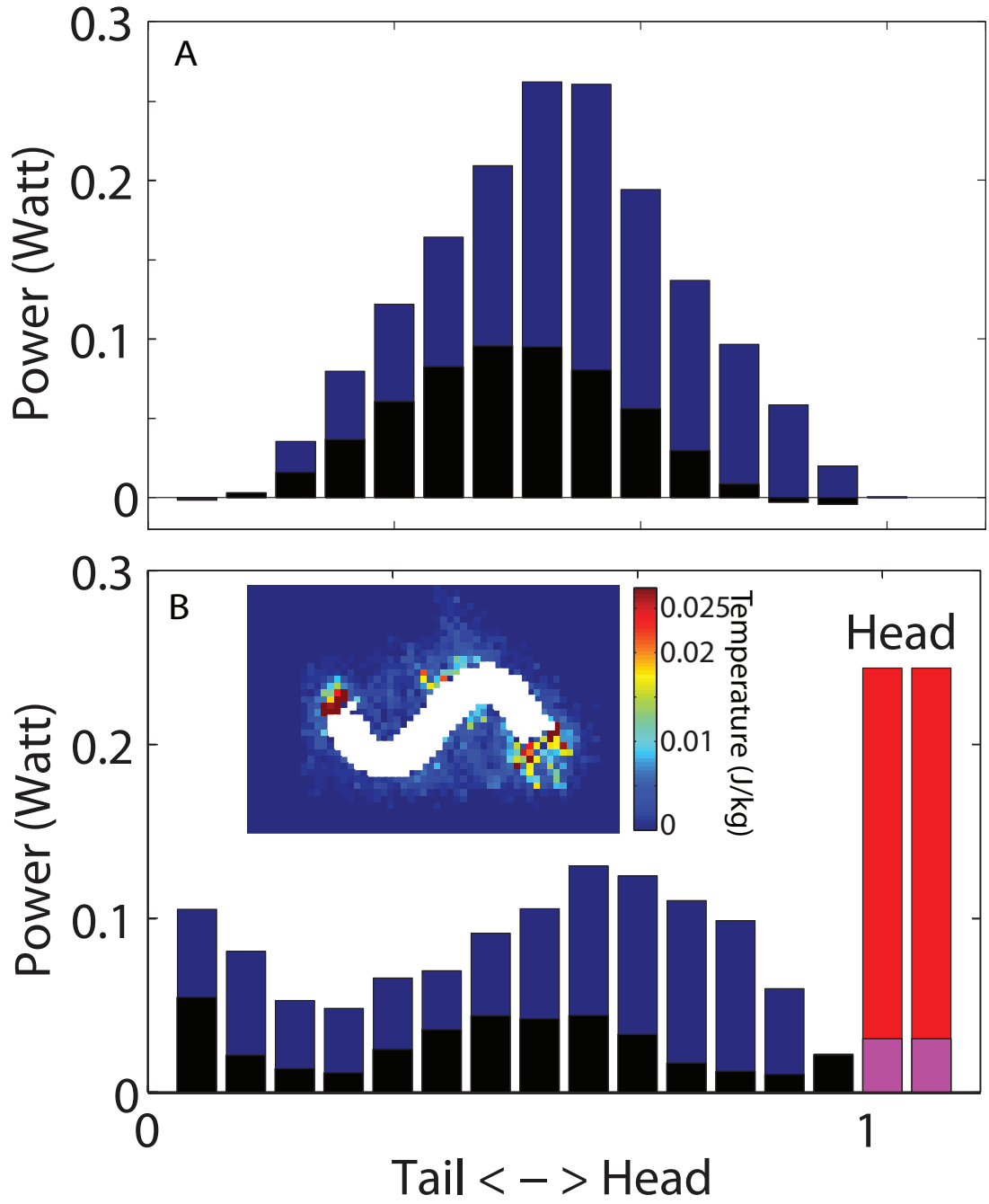
Figure 35: A: Variation of the average power output from the actuators (A) and the power output to the media (B) along the body. Each bar represents a 0.8 cm × 1.6 cm cross-sectional area along the body or on the head (head area = 1.6cm × 1.6cm). The blue bars and red bars represent the animal amplitude simulation. The black bars and pink bars represent the small amplitude simulation. Inset shows the granular temperature calculated from particles within cells with dimensions of 0.6 cm (W) by 0.6 cm (L) by 1.6 cm (H).
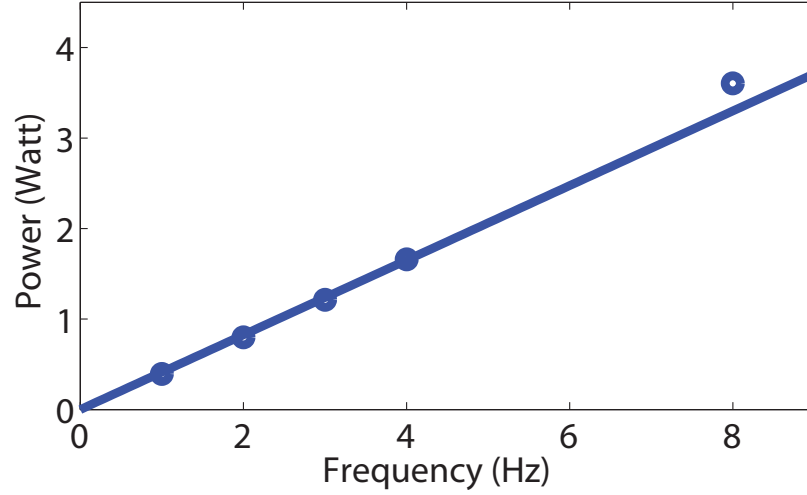
Figure 36: The total power generated by the actuators as a function of undulation frequency for the animal amplitude. Solid line is the best fit of a linear function.

appear only in the vicinities of body and decay to nearly zero in a distance of about the diameter of the body (Fig. 35B inset). The temperature was highest near the head and tail. The total power can be calculated by either summing the actuator power (generation) or the segment power (dissipation). The total power increased linearly with frequency within a biologically relevant range and become super-linear at higher frequencies (Fig. 36).

3.4.8   Cost of Transport

The mechanical cost of transport (CoT) was calculated by dividing the average power by the average speed (Fig. 37). Since both the power and the speed increased linearly with the frequency for $f < 4$ Hz, frequency did affect the mechanical cost of transportation in this range. This also implies that there is no preferred frequency for the animal in terms of energy savings assuming small inertial cost associated with accelerating body segments. We hence examined how the CoT depended on the amplitude. The power increased and plateaued near $A/\lambda = 0.2$. This resulted in a rapid decrease of CoT for small A/λ, a minimum near $A/\lambda = 0.2$ and a slow increase after. As expected, the power and CoT for a tapered body shape was smaller than the uniform body shape with a blunt head. The corresponding A/λ for minimum of CoT is close to the range ($A/\lambda = 0.2 \sim 0.3$) where the speed is maximized, indicating that maximal forward speed is associated with minimal
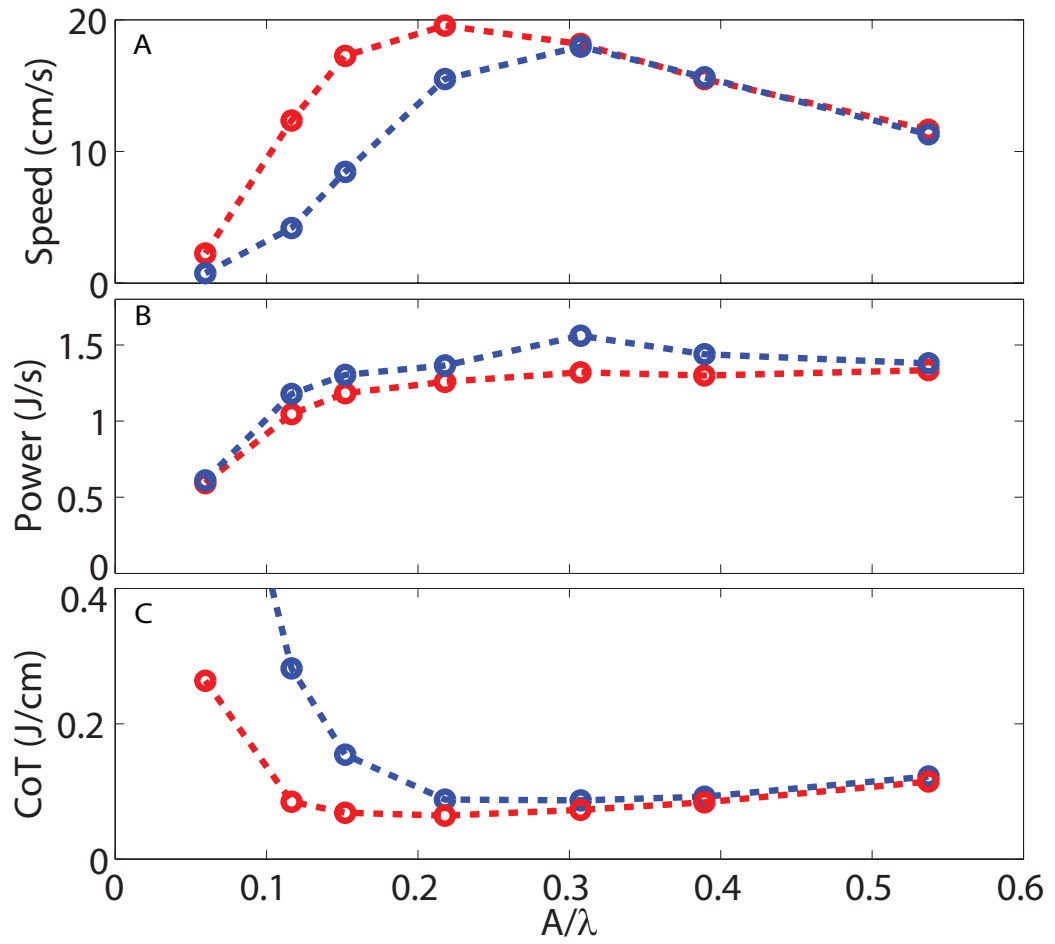
Figure 37: (A) The average speed, (B) the average power, and (C) the mechanical cost of transportation (power/speed) as functions of A/λ. Blue represents uniform body and red represents tapered body.
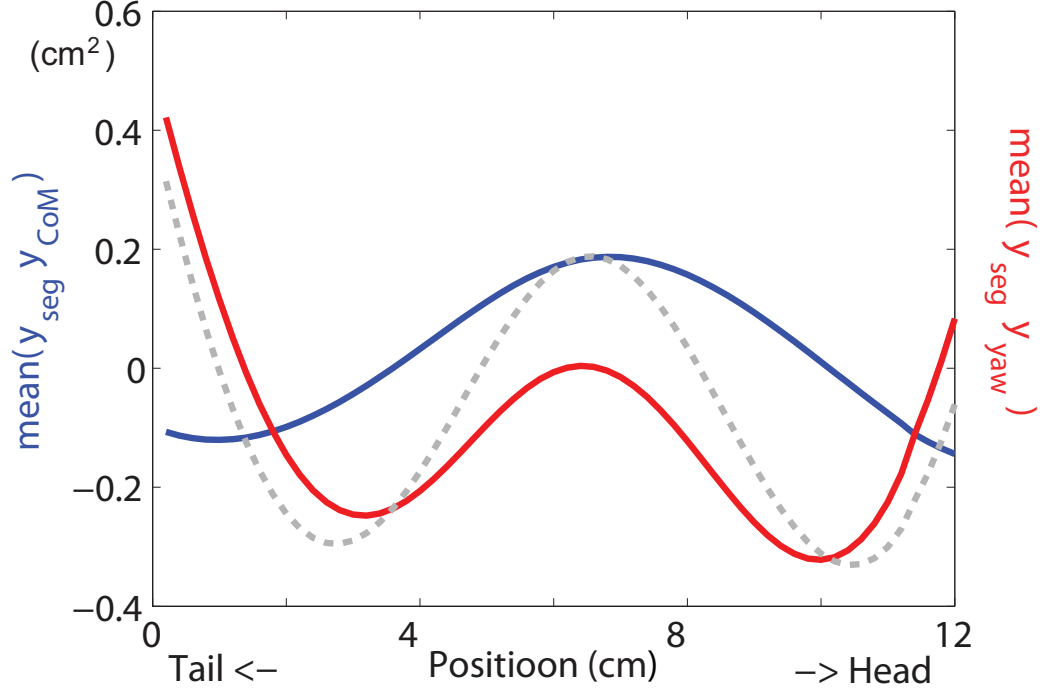
Figure 38: The correlation between the lateral motion of segments along the body and the lateral motion introduced by the CoM motion (blue curve) and yaw motion (red curve) of the body. Blue represents CoM and red represents yaw. The dashed gray line is the sum of the blue and red lines.

energy use [81].

3.5 Discussion

3.5.1 Segment motion

Because a sinusoidal traveling wave is symmetric in the lateral direction, we neglected the lateral or yaw motion of the body in the RFT model. However, because the sandfish is of finite length, net lateral force and net torque are usually not zero and they induce lateral and yaw motion. Head drag breaks the symmetry and introduces extra lateral force and torque. To examine how the pattern of the magnitude of lateral displacement of the segments was generated, we examine the correlation between the lateral displacement of a segment y_{seg} to the lateral displacement of the CoM y_{CoM} and yaw motion y_{yaw} (see Fig. 38). y_{yaw} was calculated as $y_{yaw} = \theta_b(x_{seg} - x_{CoM})$, where x_{seg} is the position of the segment in forward direction.

The positive/negative sign of the time-averaged products of the lateral displacements

63

$< y_{seg}y_{CoM} >$ or $< y_{seg}y_{yaw} >$ indicates the CoM or the yaw motion enhanced/reduced the lateral motion of the segment. The shape of the two plots indicates that the CoM motion was responsible for the enhancement of the lateral motion in the middle, while the two dips near 20% and 80% of the body length was caused by the yaw motion. As the resistive forces increase with depth within the granular medium, the anterior portion of the body of the animal experiences more resistance compared to the posterior portion of the body during burial. Therefore, we hypothesis that the larger amplitude observed in experiment is because of the increased resistive force and rotation of the body. Another factor that may also affect the magnitude of the resistive force and hence the exact functional form of y_{rms} is the lateral cross-section area, which is uniform in simulation but decrease towards the head and tail tip of the animal.

3.5.2 Forces

As shown by previous studies including ours [2, 82], (head) drag is not sensitive to the shape of an intruder in granular media [82]. Therefore the head drag acting on the sandfish is mainly determined by the head area. Since the swimming performance is determined by the balance of thrust and drag, the potential locomotion ability depends on ratio between the areas that generate thrust and areas that generate drag. This ratio may be approximated by the ratio between the cross-sectional area of the body to the head area : $A_{body}/A_{head} = bL/b^2 = L/b$. This implies that animals with a longer body may overcome the head drag more easily.

To identify the origin of the discrepancy of the force magnitude between the empirical force model used in RFT and the simulation, we dragged a 10 cm long, 1.6 cm wide square rod and measured the resistive force it experienced (see Fig. 39A). The displacement of the rod normal to its axis is prescribed as a sinusoid as a function of time to capture the undulatory motion of a segment on the animal body. We varied the frequency and amplitude of the oscillation to examine different scenarios (see Fig. 39B). We found similar discrepancies between simulation and empirical force law as for the undulatory swimming case. Based on the empirical force model, the oscillatory motion should generate a lateral
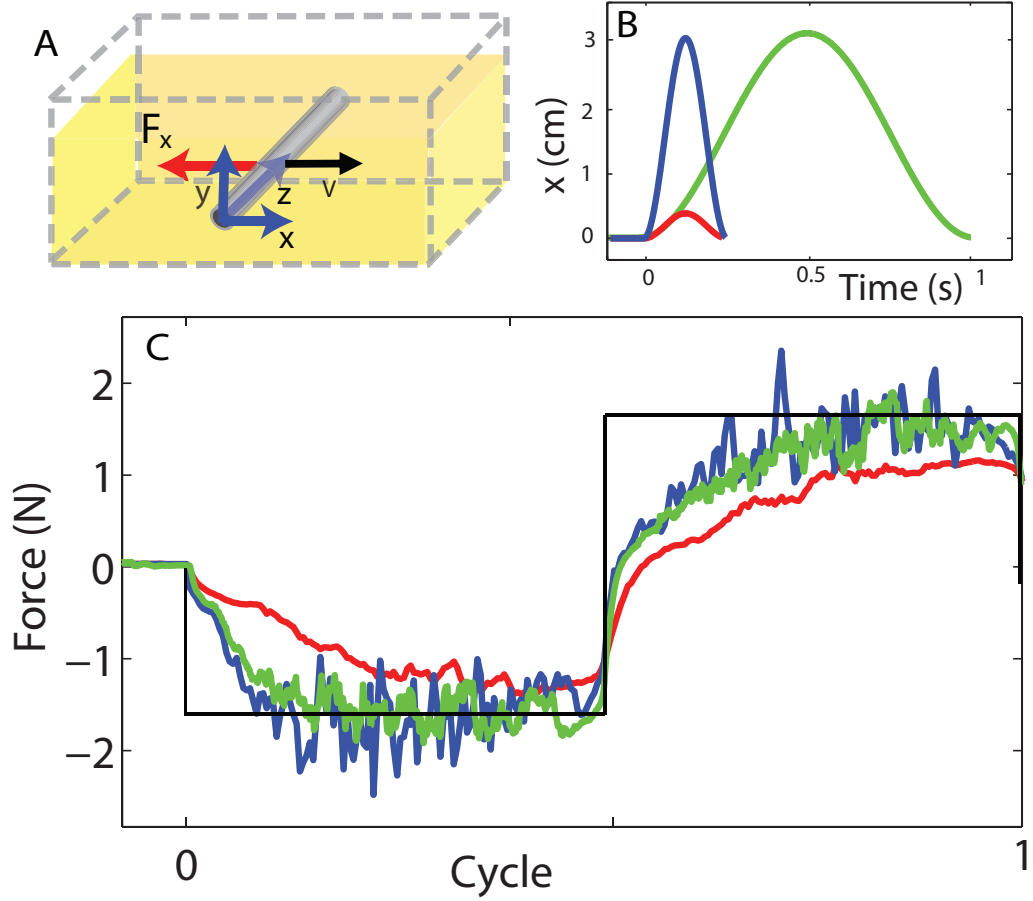
Figure 39: Drag forces on a cylinder that is oscillating horizontally and normal to its axis. A: Schematic diagram of the simulation. B: The lateral displacement of the rod as a function of time. C: The resistive force in lateral direction as a function of time. Blue, green and red lines represent the data from simulation with parameter sets ($f = 4$ Hz, $A = 1.59$ cm), ($f = 1$ Hz, $A = 1.59$ cm), and ($f = 4$ Hz and $A = 0.20$ cm).

force as a function of time that has a square wave shape (the black line in Fig. 39C), as we assume the force only depends on the motion direction. In simulation, when the rod changed direction of motion, the resistive force went back to zero quickly and then the magnitude increased gradually rather than with a discontinuous jump. Consistent with the assumption that forces are independent of speed, this discrepancy did not change significantly with different frequency (the blue line and the green line). However, the different amplitudes of the oscillation significantly affected the force. For the smaller amplitude case, the rate of the increase in magnitude was smaller and a larger portion of the cycle was in the transient region (the red line). This transient weakening effect has been observed and studied in cyclically sheared granular media [120]; the underlying physics may be related to changes in structural states such as compaction set by previous shearing (or other disturbance) [120, 97].

However, the relatively shorter transient region observed for larger amplitude oscillations does not necessarily mean that larger amplitude swimming was less affected by this transient weakening effect. That is because the lateral motion of a segment in relation to its local segment axis is not the same as the lateral motion in relation to the forward direction of the body. As shown in Fig. 5A, for the small amplitude case in which the local segment axis is nearly align with the forward direction, the lateral velocity of a segment related to its local segment axis is nearly the same as the lateral velocity in relation to the forward direction of the body. For the animal amplitude case, the velocity of a segment in the direction normal to the segment axis is only about $\tan|\psi| \approx 20\%$ of the total velocity. In the extreme case in which the swimming speed is equal to the wave speed, every segment moves in the same direction as its axis and hence there is no motion normal to any segment axis. This explains the observed over-prediction of force by the empirical force laws and the over-prediction of speed by the RFT model at all amplitudes in previous study [82].

3.5.3 Inertia

The power increases nearly linearly with frequency but the slightly higher power at 8 Hz may indicates that the inertia effects become important at higher frequency. We therefore

estimate the inertial force due to acceleration of material around the body and compare it to the total force, which includes quasi-static friction. If we take the force on an area of d^2 ($\approx$1 N) on the body as an example, the contribution from inertial force can be estimated as

$$F_{inertial} = ma = cd^3\rho_e\omega^2 A \tag{33}$$

where d^3 is the characteristic volume of granular material accelerated by the body, ρ_e is the density of the media taking into account of the voids between the particles, $\omega = 2\pi f$ is the angular velocity and c is a geometric coefficient. Assume the shape of the accelerated volume is a cube, then c=1. The formula gives 0.07 N for 4 Hz and 0.28 N for 8 Hz, which is about 7% and 28% of the total force. As $c = 1$ is unlikely to be exact and we used the maximum force as a rough estimation. Nevertheless, this estimation and the power-frequency curve (see Fig. 35C) from simulation both indicate that material inertia become non-negligible at frequencies >4 Hz. Note that the scaling of non-inertial forces and inertial forces are different: Non-inertial forces increase with depth and the inertial forces scale with f^2. This implies that the inertial force may dominate when the animal is closer to the surface. However, at typical animal undulation frequencies (less than 3 Hz), the depth at which the inertial forces have a significant contribution (>10%) is less than the diameter of the animal. Therefore the inertial force becomes negligible as soon as the animal is subsurface.

3.5.4   Power and CoT

The mechanical power required for swimming in granular media might be demanding for the animal, therefore we estimate the maximum power output from muscle and compare it to our simulation results. Assuming the mass of the animal is 14g, 50% of the body mass is muscle, and the maximum muscle power is 140 Wkg^{-1} [117], then the maximum mechanical power output is $\approx$1 W. This value correspond to about 2 Hz at the depth of 5 cm for the animal amplitude. Considering the animal has been observed to swim at a maximal frequency of $\approx$4 Hz and a depth of nearly 10 cm (the frequency and the depth were not observed at the same time), sand-swimming is energetically demanding for the animal and the muscle power might be the limiting factor of the swimming speed.

The CoT is determined by the speed and power. The dependence of speed on amplitude have been explain by the competition between the increase of wave efficiency and the decreases in wavelength. Similarly, we examine the dependence of the power on the undulation amplitude characterized by A/λ. As mentioned before, the lateral motion of a segment with respect to its axis increases slowly as A/λ increases. Since the magnitude of the force on a segment is insensitive to speed and the force direction is nearly normal to the segment for most of the time, we attribute the plateau in power to a plateau in lateral displacement of the segments relative to their axes.

3.5.5 Phase between the curvature and the torque of an actuator

Because the actuator power is the product of the angular velocity and the actuator torque, the sign of the power is an indicator of the phase difference between the angular velocity and actuator torque. The nearly zero or negative actuator power near the tail and head indicates that the angular velocity is in antiphase with the actuator torque while the positive power indicates the two variables are in phase. The sign of power also implies that the phase between actuator torque and angular velocity varies along the body. The phase shift of muscle activation relative to the curvature, which is closely related to torque generation, has been observed on aquatic and terrestrial animals [47, 18, 122] as well as in the sandfish [110]. Body stiffness and elasticity, which are determined by muscle and passive elements such as tendons, play important roles in swimming in fluids and have been shown to affect the phase shift between the curvature and muscle activation [79, 80, 122]. Although our animal model consists of only actuators and rigid segments, the zero or negative power indicates a possibility of generating similar kinematics with passive elements and an elastic body in granular media. As the bending of the body is (nearly) in antiphase with the torque near the tail, joints/body with certain elasticity without actuators may bend the same amount in response to the torque generated by granular force, hence generate similar kinematics.

3.5.6 Comparison of granular to fluid swimming

It is instructive to compare the mechanics of undulatory swimming in granular media to that in fluids and other environments. Similar to swimming in fluids, the coefficient for

the normal component of the resistive force is larger relative to the lateral force. Therefore the forces point to the opposite side of velocity and are nearly perpendicular to the axes of the segments and parallel to the velocity vectors. This results in a similar pattern of the force on the body in granular media similar to that in fluid and the surface of the ground [18, 61]. Similar oscillation in the forward and lateral direction, yaw motion, and similar patterns for the amplitude of lateral displacement have been observed in a computational study of swimming in a fluid ([16]). The different force laws do, however, lead to differences in the swimming mechanics. The power increases linearly with speed in granular media but increases super-linearly in fluid. The head drag can only be reduced by a maximum of 30% in granular media but can be reduced by an order of magnitude by streamlining in a fluid. Because thermal fluctuation does not destroy the disturbed state of the granular media, material properties such as yield stress exhibit hysteresis effects. The transient weakening effect, which reduces the thrust on the body, is one example of such effects in granular media.

3.6   Summary

Motivated by biological experiments of sandfish locomotion we developed a numerical simulation approach to study undulatory sand-swimming. We used this model to test the assumptions and predictions of our previously developed empirical resistive force model. We showed that swimming performance comparable to that of the animal can be achieved within granular media by utilizing the kinematics of the animal. We determined how η depends on the spatial characteristics of the undulatory swimmer and showed that an optimal $A/\lambda \approx 0.2$ and $\xi \approx 1$ maximized forward swimming speed. The robot with a finite number of segments (7) confirmed these optimal kinematics and simulation explained why the performance of the robot was lower than the animal. Remarkably, the sandfish uses these optimal kinematics to swim rapidly within granular media.

The coupling between the prescribed body motion, resistive forces from the media, and the overall body motion generate non-trivial patterns of segment motion and power dissipation along the body even though both the geometry and the prescribed motion of

the segments are uniform along the body. The energy was generated mainly from the central segments and a significant portion was dissipated to overcome the head drag for the animal amplitude. As the resistive force in granular media is independent of speed, power scaled linearly with frequency and CoT did not depend on frequency in the biological relevant range. However, the transition weakening effect associated with oscillation of intruders must be taken into consideration for an accurate description of the resistive forces in granular media and the sand-swimming mechanics. Although the force laws in granular media is different from fluid (e.g. enhanced normal forces in granular media and different scaling with velocity), we observed phenomena that are general for undulatory swimming, such as larger thrust forces are generated from the segments that have larger angles relative to the forward direction, and that power is generated mainly by the central portion of the body.

CHAPTER IV

DRAG INDUCED LIFT IN GRANULAR MEDIA

4.1 Introduction

Objects moved through media experience drag forces opposite to the direction of motion and lift forces perpendicular to the direction of motion. The principles that govern how object shape and orientation affect these forces are well understood in fluids like air and water. These principles explain how wings enable flight through air and the fins generate thrust in water [123].

Lift and drag forces are also generated by movement within dry granular media, collections of discrete particles that interact through dissipative contact forces. We hypothesize that the generation and control of these forces while moving within granular media is biologically relevant to many desert inhabitants that dive into [7], or swim within [81] sand such as the sandfish lizard. Lift forces are also relevant to industrial process such as soil tillage [96]. The work presented in this chapter was partially inspired by the morphology of the sandfish–a shovel shaped head and a flat belly (Fig. 40). We therefore investigate how the shape affect the lift force in granular media using experiment and simulation and explain the lift force by developing a force model based on the flow field from simulation [*][†]. We applied the principles learned from drag experiment and simulation to the head shape of the sand-swimming robot to control the vertical motion of the robot [‡][§].

In granular media, lift and drag forces are not as well understood as in fluids; movement probes the complex fluid/solid behaviors of dense granular flows [65]. While progress has

---

[*]The experiments were done by Nick Gravish, a physics graduate student in Goldman's group.

[†]This work has been published as a journal paper:"Drag induced lift in granular media", Yang Ding, Nick Gravish and Daniel I. Goldman, *Physical Review Letters*, 106, 028001 (2011)

[‡]The robot development and experiments were done by Ryan Maladen, Paul Umbanhowar and Andrew Masse, who were BME graduate student, visiting scientist and Physics undergraduate student in Goldman's group.

[§]The work presented here has been published as part of a peer-reviewed conference paper: "Lift control in a sand-swimming robot," Ryan D. Maladen, Paul B. Umbanhowar, Yang Ding, Andrew Masse and Daniel I. Goldman, *IEEE: International Conference on Robotics and Automation* (2011).
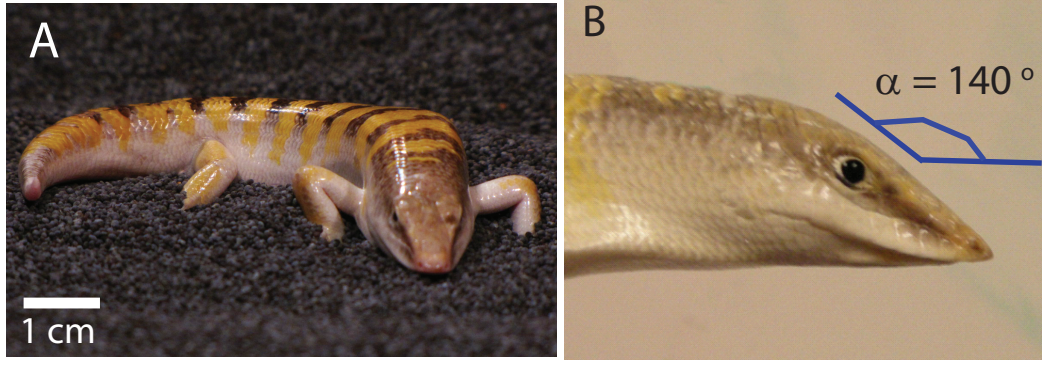
Figure 40: (A) Front and (B) side views of the sandfish head. α is the angle of the leading surface of the sandfish head respect to the horizontal.

been made understanding drag forces in slow horizontal and vertical drag and impact [3, 48, 93, 51], there has been comparatively little work investigating lift forces. Studies have examined lift forces for a partially submerged vertical rod moving horizontally and for a rotating plate [114, 125], and the drag force on submerged objects with curved surfaces [2]; however, the lift forces experienced by horizontally translated submerged intruders have not been explored.

4.2 Experiment and simulation setup

Experiment and simulation were employed to investigate the lift (F_z) and drag (F_x) forces on simple shapes during horizontal translation in granular media (Fig. 41). In experiment long intruders with different cross-sections were dragged within a bed of glass beads with particle diameter (PD) of 0.32 ± 0.02 cm and density (ρ) 2.47 g/cm^3 (Fig. 41). Dragging was performed at a constant speed 10 cm/sec with the intruder's vertical mid-point at depth $d = 12.5$ PD and its long axis perpendicular to the direction of motion. In experiment, $l = 31.3$ PD long intruders were connected at the midpoint to a force sensor (mounted to a linear translation stage) by a stiff stainless steel rod of diameter 2 PD. Following the method of [3], forces on the connecting rod were determined in separate measurements and subtracted from F_x and F_z. The grain bed was 75 PD wide by 53 PD deep by 75 PD long. The initial packing state of the grains was prepared by shaking the container moderately in the horizontal direction before each run. The volume fraction was determined through measurements ρ, total grain mass (M), and occupied volume (V) to be $\frac{M}{\rho V} = 0.62 \pm 0.01$.

72
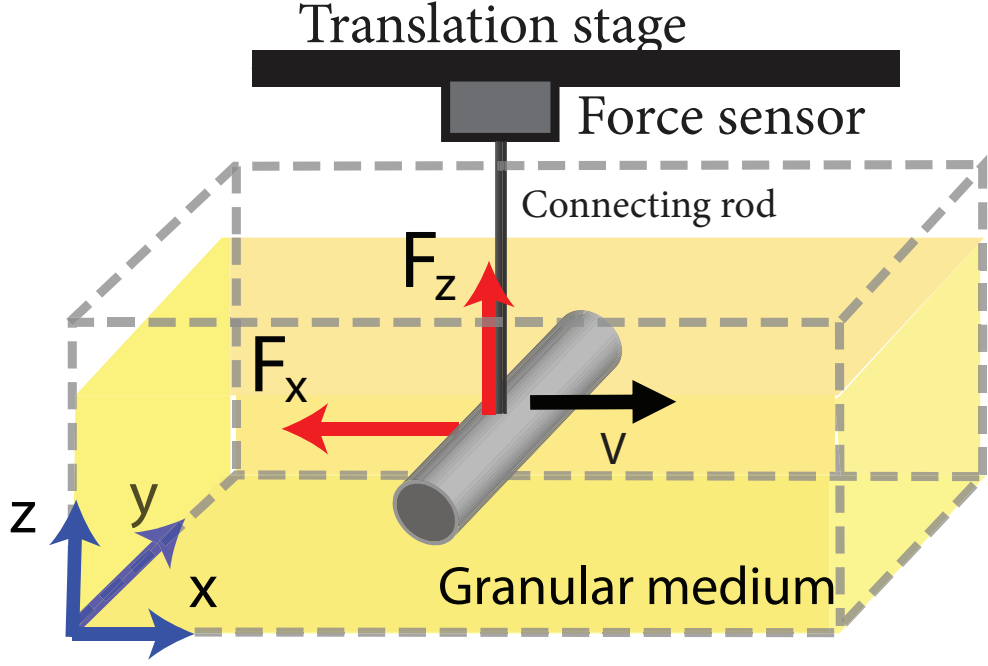
Figure 41: A: Schematic of the setup of the rod drag experiment.

Simulation employed the soft-sphere Discrete Element Method (DEM) method (see Chapter III for more details about model development) with $\mu = \mu_{\{pp,pi\}} = \{0.1,\ 0.27\}$ as particle-particle and particle-intruder friction coefficients respectively. The simulated grain bed, bounded by frictionless walls, was 75 PD wide by 55 PD deep by 78 PD and consisted of 350,000 particles in a bi-disperse mixture of equal parts 0.3 and 0.34 cm diameter spheres. Doubling any dimension of the grain bed did not change the forces significantly. The initial volume fraction 0.62 ± 0.01 was prepared by randomly distributing the particles in the volume corresponding to the desired volume fraction and then eliminating particle overlap [95]. Forces were nearly independent of speed, like other drag studies in the non-inertial regime [126, 17] (speed $\lesssim 40$ cm/s for our study). In simulation the intruder dimensions and intruder speed were matched to those in experiment and the forces were averaged over the steady-state time intervals.

4.3 Shape determines lift

In both experiment and simulation, F_z was sensitive to the cross-section of the intruder. As shown in Figure 41 & 42, F_z for the half-cylinder was downward (opposite the orientation
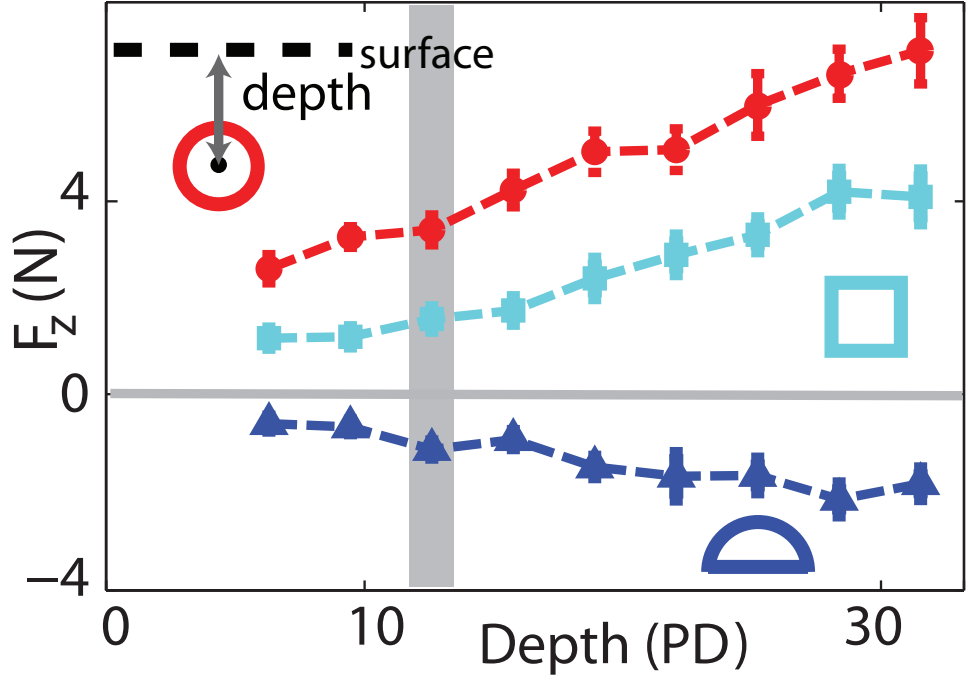
Figure 42: Lift force as a function of depth for the cylinder (●), square rod (■) and half cylinder (▲). Gray region indicates the depth at which forces in Figure 43 were measured.

of the curved surface), while for the two vertically symmetric geometries, the full cylinder and square rod, F_z was positive with magnitude larger for the cylinder than for the square. Experiments with smaller glass particles (0.3mm) gave similar results (see Fig. 43). $|F_z|$ increased with intruder depth for all intruders (Fig. 41B). The lift mechanism is different from the Brazil nut effect [104] which results from agitation of the medium by the container.

Simulation allowed investigation of the surface stress distribution responsible for lift and drag on the intruders. For all shapes the surface stress was largest along the leading surface (Fig. 43 green arrows). Due to the linear dependence of granular pressure with depth and the finite size of the intruder [3], local stresses increased with depth along the flat face of the square (Fig. 43). However, for curved intruders (e.g. the cylinder in Fig. 43), the magnitude of local stress was primarily determined by the local surface orientation. As the local surface tangent became more aligned with the intruder velocity the force magnitude became small, supporting observations that surfaces parallel to the direction of motion contribute little to the drag force [2]. Since the normal force was larger than the frictional force, the direction
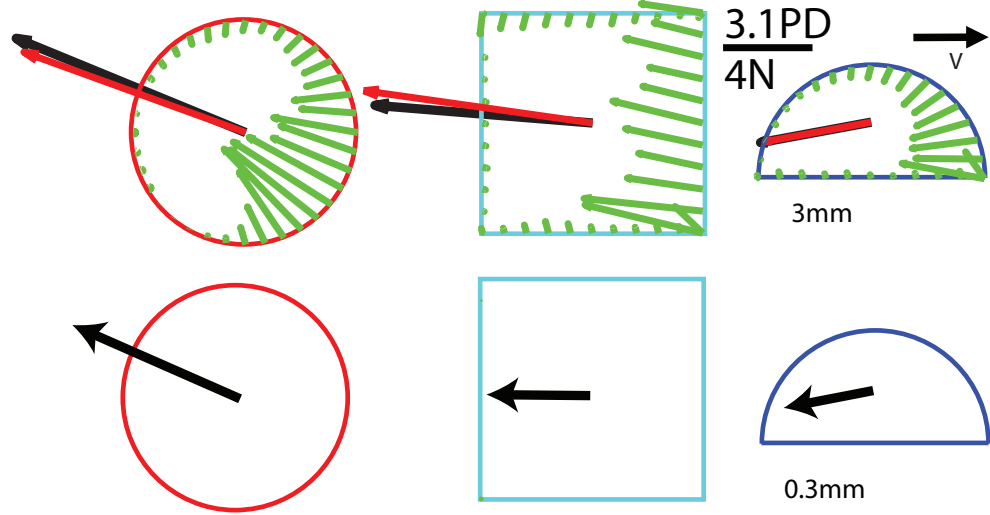
Figure 43: Net force on rods measured in experiment (←) and simulation (←). Forces (←) on the intruder surfaces were measured in simulation and are scaled by four for better visibility.

of the local grain-intruder reaction force was nearly opposite to the surface normal at all points along the intruder's leading surface.

The dependence of the forces on the local surface orientation suggests that decomposing the surfaces into differential area elements and summing the forces on those elements may describe the net drag and lift experienced by the three shapes studied. This is similar to the resistive force theory developed in Chapter II, which was used to calculate the net force on the sandfish in the horizontal plane.

4.4 Plates as differential elements

To determine if the forces on curved intruders can be understood by decomposing the shape into flat plate elements, we now study the stresses on a flat plate with tangent angle α varied between $0°$ and $180°$ (e.g. $\alpha = 0°$ is along the direction of motion). In simulation, a long ($l = 31.3$ PD), thin (0.1 PD), flat plate of finite width $w = 7.94$ PD was dragged horizontally through the granular medium with its center 12.5 PD below the initial surface, and the average normal (σ) and shear stress (τ) on the leading side of the plate were measured as a function of α (Fig. 44A). The stresses were asymmetric about $\alpha = 90°$, and σ increased rapidly for small α, peaking at $\alpha \approx 50°$. At $\alpha \approx 60°$, τ changed sign, indicating
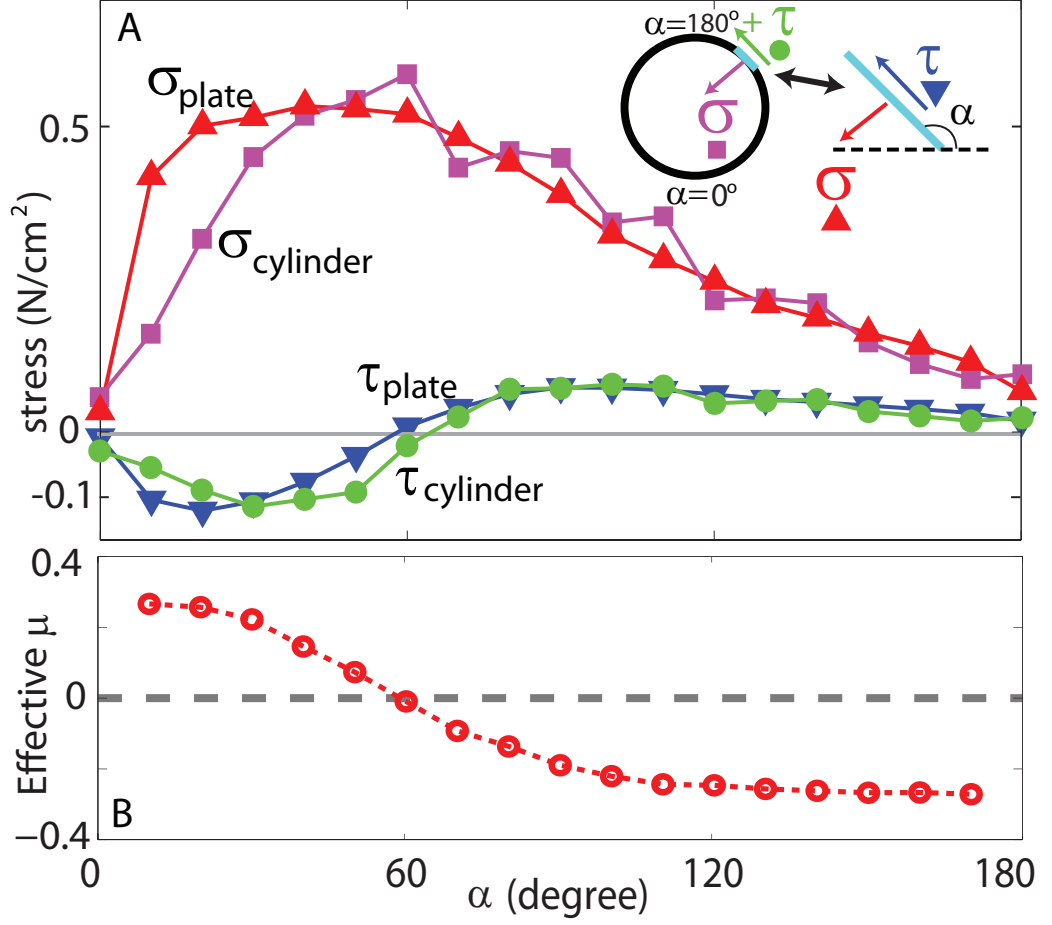
Figure 44: A: Normal stress (σ) and shear stress (τ) on the leading surface of the cylinder as functions of tangent angle α compared to the stresses on a plate with the same α. ■, ▲, ●, and ▼ represent $\sigma_{cylinder}$, σ_{plate}, $\tau_{cylinder}$ and τ_{plate} respectively. B: Effective friction coefficient on the leading surface of the cylinder as functions of α.

a reversal in grain flow along the surface. We define the effective friction ratio on the plate as $\mu_{peff}(\alpha) = \tau/\sigma$, which is zero at $\alpha \approx 60°$ and saturates to the expected magnitude of μ_{pi} for $\alpha > 135°$ and $\alpha \approx 0°$ with opposite signs (Fig. 44B). Remarkably, along the surface of the cylinder (half-cylinder and square rod as well), the stresses approximately matched the stresses on the plate oriented at the same angle α (Fig. 44A). The stresses on the intruders were corrected by considering that the depth of the differential element is different from the depth of the center of the cylinder and assuming linear dependence of the stress on depth.

The near equality between the stresses on plates and local surface regions of intruders with the same orientation implies that F_z and F_x for a translated rod can be approximated
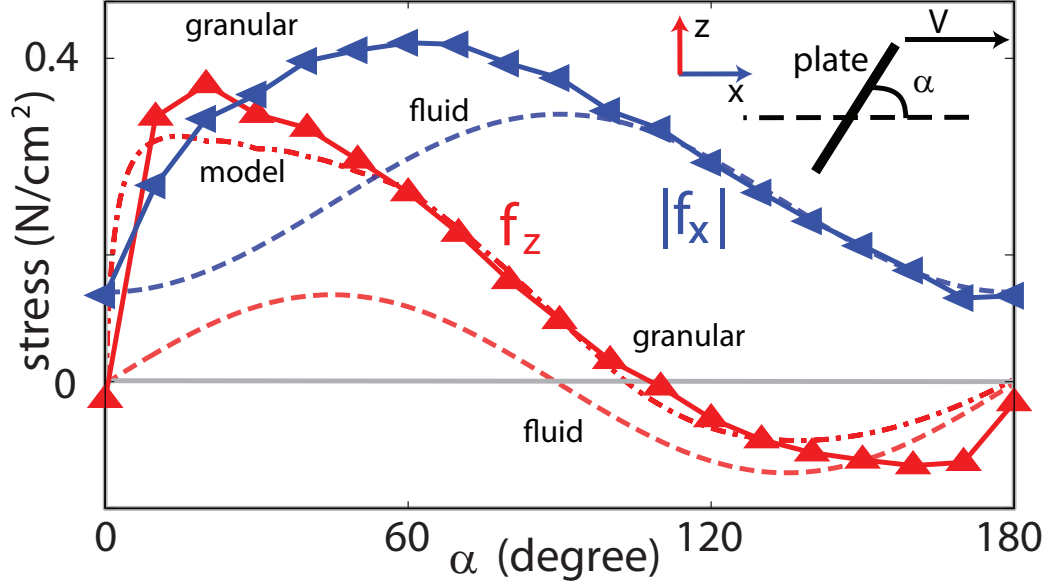
Figure 45: The drag ($|f_x|$, blue) and lift (f_z, red) components of the stress on a plate as a function of α in granular media (◀ and ▲) as compared to a fluid with with Re ≪ 1 (dashed lines) [50]. Dash-dot red line is granular wedge model (see section 4.5).

by the sum of forces from the corresponding shape built from infinitesimal plates. Resolving the stresses on the plate at orientation α into the lab frame (xyz) gives the local lift $f_z(\alpha)$ and local drag $f_x(\alpha)$ force contributions per unit area on the plate element (Fig. 45). F_z for different shaped rods results from the integration of $f_z(\alpha)$ contributions along the intruders leading surface, corrected by a linear depth term, over the intruders infinitesimal surface area dA, e.g. $F_z = \int f_z(\alpha)(z/d)dA$ (Fig. 46A). Comparison of this integration over the three rod shapes with the measured F_z from simulation and experiment (Fig. 46B) shows good agreement. The orientation of the leading surface of the cylindrical intruder varies from $0 \leq \alpha \leq 180°$ and the asymmetry of $f_z(\alpha)$ results in a net positive lift. Positive f_z at $\alpha = 90°$ is responsible for the small lift on the square rod. For the half-cylinder, $90 \leq \alpha \leq 180°$, and F_z is negative.

To gain insight into the nature of granular drag and lift we compare our results to those from low Reynolds number fluids where inertia is negligible and viscous forces dominate. f_x and f_z on a plate at angle α in low Re fluids are symmetric along the direction of motion $\alpha = 90°$ (Fig. 46, dashed curves) while the drag and lift forces on the plate in granular media are asymmetric about $\alpha = 90°$. This suggests that a granular model is required to
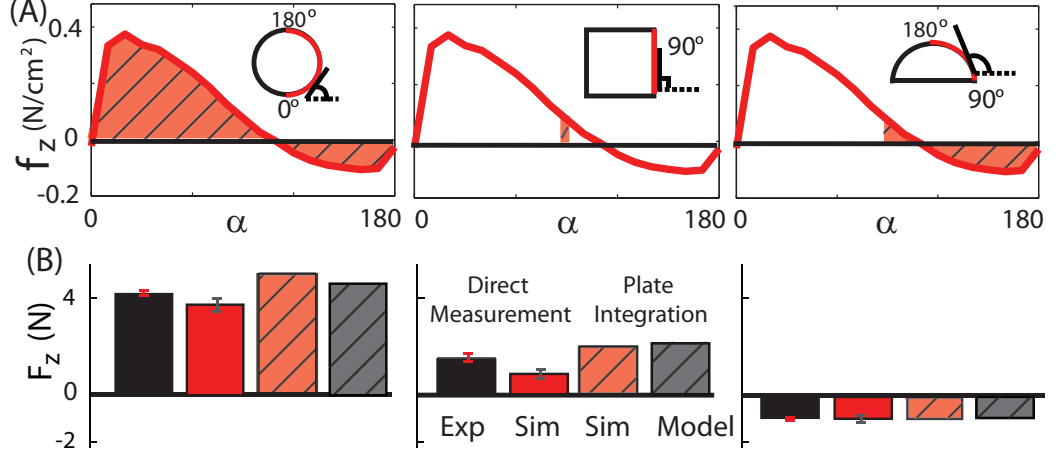
Figure 46: F_z on intruders calculated by integration of $f_z(\alpha)$. Red outlines on the shapes indicate the leading surface and the hatched area indicates the corresponding range of α and region of integration. (b) F_z calculated by integration of f_z from simulation (red hatched bar) and model (gray hatched bar) compared to direct measurement of F_z in experiment (black bar) and simulation (red bar).

understand the origin of lift in granular media.

4.5   Force model

In the quasi-static regime of granular flow, the moving volumes of grains in granular media can still be considered as in force balance. The force on an intruder can be determined by analyzing the force balance the moving volumes [126, 96]. With the plate acting as one flow boundary we can determine the normal and tangential components of stress (σ and τ) on the plate surface from these force balance equations. In practice this requires approximating the boundaries of the moving media as planes and computing the forces acting on them.

Examination of the motion of grains in the vertical plane (xz) reveals that the particles move upwards in front of the plate and flow along a lower boundary (see Fig. 47A), a slip plane. Finite yield stress in granular media results in flowing regions bounded by slip planes with upward flow direction due to increasing yield stress with depth [126]. The upper region of the flow is confined by a boundary starting from the top edge of the plate and approximately parallel to the lower boundary. We define the upwards flow area A as the region where average particle velocity $\vec{v}$ satisfies $v_x > 0.1V$ and $v_z > 0$. Velocity is averaged over 1.9 PD×1.9 PD cells along the central 90% length of the plate at four time

78
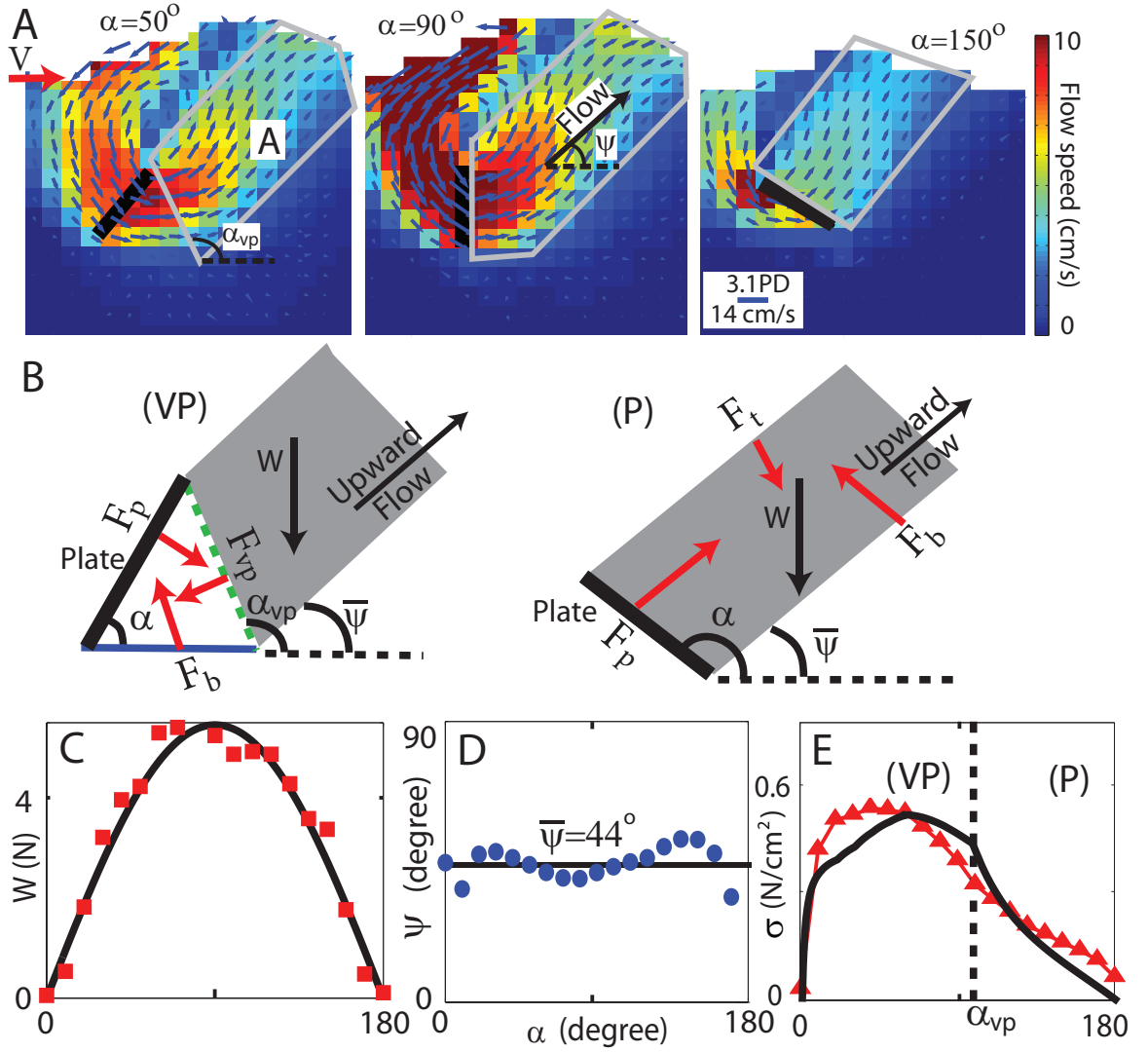
Figure 47: Flow of grains and force-balance model. A: Flow field in the vertical (xz) plane for three plate (solid black line) orientations. Gray boundary indicates regions with upward flow [18]. B: Forces on a wedge for $\alpha < \alpha_{vp}$ [regime (VP)] and on the band for $\alpha \geq \alpha_{vp}$ [regime (P)]. C: The weight of the upward-flow region as function of α calculated from simulation (■) and fit (black) to $W = c\sin(\alpha)$, where $c = 5.7$ N. D: The average flow velocity angle ψ in the upward-flow region vs. α (●). E: Normal component of the stress on the plate σ calculated from the model (black) and measured from simulation (▲). The black dashed line $\alpha = \alpha_{vp} = 97°$ indicates the boundary between the two regimes (VP) and (P).

instants with intruder position separated by 0.3 PD. W is calculated as $W = \rho_e g l A$, where $\rho_e = 1.53$ g/cm^3 is the effective media density including voids. The weight W of this up-flow region A is well fit by $W = c \sin \alpha$, and is thus proportional to the projected plate length normal to the direction of motion (see Fig. 47C). The direction of average velocity of the particles in the band ψ varies little (see Fig. 47D) and we approximate the angle of the flow boundaries as $\bar{\psi} = 44°$.

The plate defines one of the boundaries of A for large α (e.g. $\alpha = 150°$ in Fig. 47A) but for small α (e.g. $\alpha = 50°$ in Fig. 47A), the vertical velocity of the particles adjacent to the plate is negative and thus the upward flow boundary is described by a virtual plane intersecting the top of the plate and extending downwards at angle α_{vp}. We therefore consider two regimes of flow: for $\alpha \geq \alpha_{vp}$, we approximate A as bounded by the plate and two parallel surfaces with angle $\bar{\psi}$ [regime (P) in Fig. 47b]. For $\alpha < \alpha_{vp}$, the upwards flow region A is bounded by the virtual plane and two parallel surfaces with angle $\bar{\psi}$. The region adjacent to the plate is bounded by the plate, the virtual plane, and an approximately horizontal bottom surface [regime (VP) in Fig. 47b]. For regime (P), the forces on the flowing band are the forces from the top and bottom boundaries and its weight. On the plate surface, the friction coefficient $\mu_{peff}(\alpha)$ (Fig. 44) is used. Within the media, dynamic friction is assumed and the friction coefficient is $\tan \gamma$, determined by the angle of repose, $\gamma = 13 \pm 1°^{\ddagger}$, which is measured in separate simulations by tilting the initially horizontal container and recording the post avalanche surface orientation. Simulation indicates that the stress at the bottom surface dominates; therefore we neglect the force on the top of the flow band (F_t in Fig. 47B). The normal stress on the plate, σ, can be solved from the force balance on the band to obtain $\sigma(\alpha) = \frac{W}{lw} \frac{\cos \beta \sin(\bar{\psi} + \gamma)}{\sin(\alpha - \beta - \bar{\psi} - \gamma)}$, where $\beta(\alpha) \equiv \tan^{-1} \mu_{peff}$.

For regime (VP), the normal stress on the plate is calculated by considering the stress on the wedge adjacent to the plate. The stress on the virtual plane can be solved by the above equation with the corresponding weight of the band and a fixed angle $\alpha = \alpha_{vp}$. Solving the force balance equation for this triangular wedge we obtain $\sigma(\alpha) =$

$\frac{W}{wl} \frac{\cos\beta \sin(\bar{\psi}+\gamma)}{\sin(\alpha_{vp}-\beta'-\bar{\psi}-\gamma)} \frac{\sin(\alpha_{vp}-\beta'-\gamma)}{\sin(\alpha-\beta-\gamma)}$, where $\beta' = \beta(\alpha_{vp})$. The parameter $\alpha_{vp} = 97°$, determined from a best fit of $\sigma(\alpha)$ from simulation, is within the expected range from flow field observations (Fig. 47).

Comparison of σ calculated from the wedge model and σ measured directly in simulation demonstrates that the model captures the asymmetric shape of σ (Fig. 47E). Integration of f_x calculated from the model over the non-planer intruder surfaces yields net lift forces in agreement with those from other methods (Fig. 46B). The decrease in σ above $\alpha = 90°$ results from the decrease in W with increasing α. For $\alpha \leq 90°$, although W increases with α, the stress on A is transmitted by the wedge which induces extra resistance on the bottom plane; therefore σ peaks at α smaller than $90°$. The model assumes the up-flow area A (W) increases with depth which explains the monotonic increase of $|F_z|$ with depth. The discrepancy between σ in model and simulation may be due to the simplified description of the shape of the boundaries of the flowing media, approximation of ψ and α_{vp} as constants and W as a simple function, and neglecting F_t.

Decomposition of the force on the intruder into forces on differential elements assumes that the flowing region corresponding to each element is not disturbed by other elements. This may explain the difference we observe between the stress on the plate and the local stress along the intruder for small α (corresponding to elements on the bottom), where the upper flow boundary for these elements is obstructed by higher regions of the cylinder. For objects with concave leading surfaces, the use of differential surface elements may require consideration of material jamming in the concave region.

4.6 Lift control for the sand-swimming robot

In previous sections, we have shown that the magnitude and sign of lift in granular depends on the shape of the leading surface of the intruder and increase of yield stress with depth in granular media causes the asymmetric lift forces: the magnitudes of lift forces on plates facing downward are enhanced. To test if the shape dependent lift force is important in vertical motion of sand swimmer, we study the effect of the head shapes on the vertical trajectory of the robot. In our previous study [83], the robot with a square block head rises
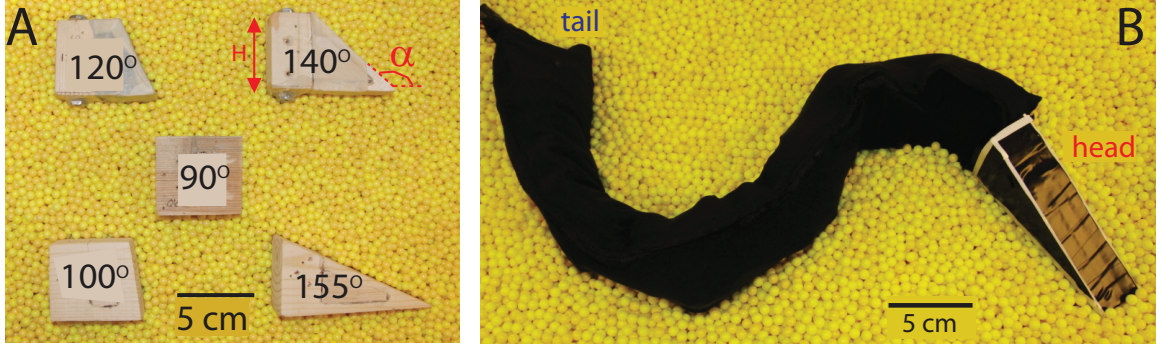
Figure 48: A: Side view of the wedges tested in robot and drag experiments resting on 6 mm plastic particles. All wedges have fixed height ($H = 5$ cm), transverse projected area $= 27.5$ cm^2. B: The robot with a representative wedge ($\alpha = 155°$) attached at the head.

to the surface of the media as it progressed forward. As this vertical motion appears only when the robot progresses forward, and the ratio of the density of the robot to the plastic particles was greater than one ($1.16 : 1$), the drag induced lift should be the dominant force.

4.6.1 Lift forces on wedges

Inspired by the head shape of the sandfish lizard (Fig. 40), we attached wedge shaped heads to the robot as shown in Figure 48A). These heads all have flat bottom surfaces, the same height and projected areas in front and lateral direction. The angle of the upper surface of the wedge (α) was varied. We flipped the wedges upside down to obtain a range of α from 25° to 155°. The weight of each wedge was kept the same as the weight of the block robot head (110 g).

To quantify the lift force on the wedges, we dragged the wedges by a robotic arm through a container ($40 \times 30 \times 24$ cm^3) filled with the same 6 mm plastic particles used in previous robot experiments [83]. In the experiment, wedges moved at a constant speed of 5 cm/s with their vertical mid-point at depth d=6.5 cm and its bottom surface parallel to the motion direction (see Fig. 49 inset). A 6 d.o.f. force sensor (ATI industrial) on the robotic arm was used to measure the drag and lift forces. The force on the connecting rod was measured separately and subtracted from the total forces to obtain the forces on the wedges.

Similar to the lift force on plates shown in Figure 45, we found that the magnitude of the positive lift force experienced by the wedges with small α are much larger than the
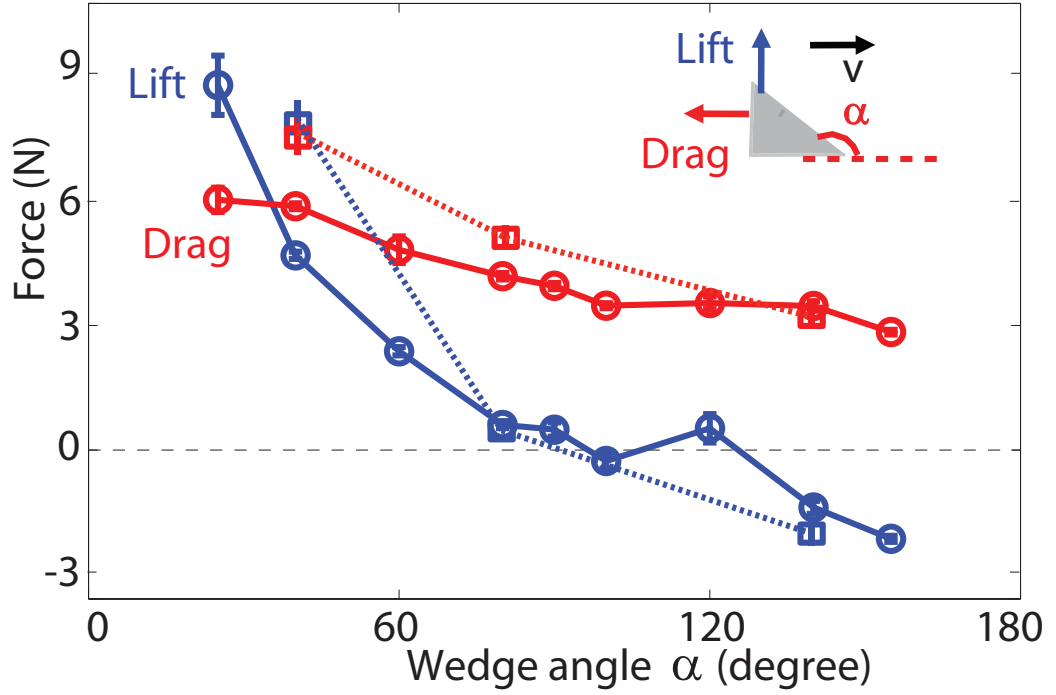
Figure 49: The drag and lift forces on the wedges dragged through 6 mm plastic particles at 5 cm/s with different angles shown in Figure 48A. Inset: schematics of the experiment.

magnitude of the negative lift forces experienced by the same wedges flipped (with angles $\pi - \alpha$). We also found the lift force is small but positive at $\alpha = 90°$ (block square head), which is consistent with the rising of the robot with block square head as it progress forward in previous experiments. The drag force is relatively less sensitive to the head shape; the drag reduction for a head shape with $\alpha = 90°$ (similar to the animal) is only about 20%, close to the head drag reduction observed on a tapered body shape in simulation (see Chapter III, section 3.4.5).

We investigate the flow field and the force distribution on the surface of the wedge to compare with those from plate drag simulation. As shown in Figure 50, the surfaces that are parallel to the motion direction or on the trailing side of the wedges contributed little to the drag or lift forces. The flow is also asymmetric such that for all shapes most particles in front of the intruder rise while moving forward, due to the increases of yield stress in granular media.
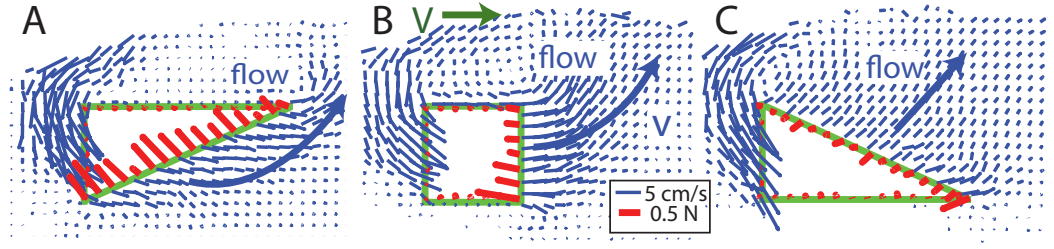
Figure 50: Flow field and force distribution on wedged dragged through experimentally validated 6 mm plastic particles in numerical simulation. (A), (B), and (C) correspond to $\alpha = 40°$, $90°$, and $140°$ respectively. Red and blue lines denote the magnitude and direction of force on the surface of the objects and the velocity of the particles respectively. The thick blue arrows indicate the average direction of flow. Velocity is averaged over 0.8 cm×0.8 cm cells along the thickness of the plate (into the page) and 2 time instants separated horizontally by 0.05 cm. The force is similarly averaged except the volume is replaced by a area on the surface of the intruder.

4.6.2 Lift control by varying robot head shape

To quantify how much the head shape affected the trajectory of the robot in the vertical plane, we tracked the position of the two balls at the top of masts at the head and tail(Fig. 51). The lift force on the head may affect the vertical motion in two ways: a net force in the vertical direction and a net torque in the vertical plane. We found the vertical motion of the robot is mainly from the torque effect as the vertical motion was lead by the head. The rate of vertical displacement of the CoM of the robot (cm/cycle) was measured by averaging the vertical displacement of the two masts. We found that the vertical motion of the robot is sensitive to the head shape. The direction and magnitude of the vertical motion resembles the lift force on the corresponding wedge as shown in Figure 51: The robot pitch and rise to the surface for head shapes with $\alpha < 90°$; the robot descended into the media for $\alpha > 120°$; for $100° < \alpha < 120°$, no significant vertical motion was observed until it encountered the end of the container. Our results support our hypothesis that the wedge-shaped head facilitate the burrow and swimming of the sandfish as it provides a negative lift and reduces head drag compared to a blunt head. For a wedge like the sandfish head ($\alpha = 140°$), tilting up the wedge a few degree may dramatically change the flat bottom become a leading surface with small α, which would generate a large lift force. Therefore

we hypothesis that the animal uses head tilting to aid its control of vertical motion. Initial investigation of the robot with a actuated head showed that head tilting is effective in controlling the vertical motion of the robot.

4.7   Summary

We have shown that the magnitude and sign of the drag induced lift force in granular media depends on the shape and depth of the intruder. Drag induced lift on non-planar intruders can be computed as the summation of lift forces from planar elements. The increase of yield stress with depth in granular media causes the asymmetric flow that the media move upward along a slip plane in the direction of motion regardless of the intruder shape or inline angle of the plate. Based the flow field and force balance of the flowing region, we developed a force model that quantitatively explain the observed forces such as the enhanced lift force on a plat facing downward. By attaching wedges with different angles to the previously developed sand-swimming robot, we verified that the vertical motion can be effectively controlled by head shape. Our results also suggest that the shape of the sandfish can facilitate the burrowing and swimming of the animal since the head provides a negative lift and reduced drag.
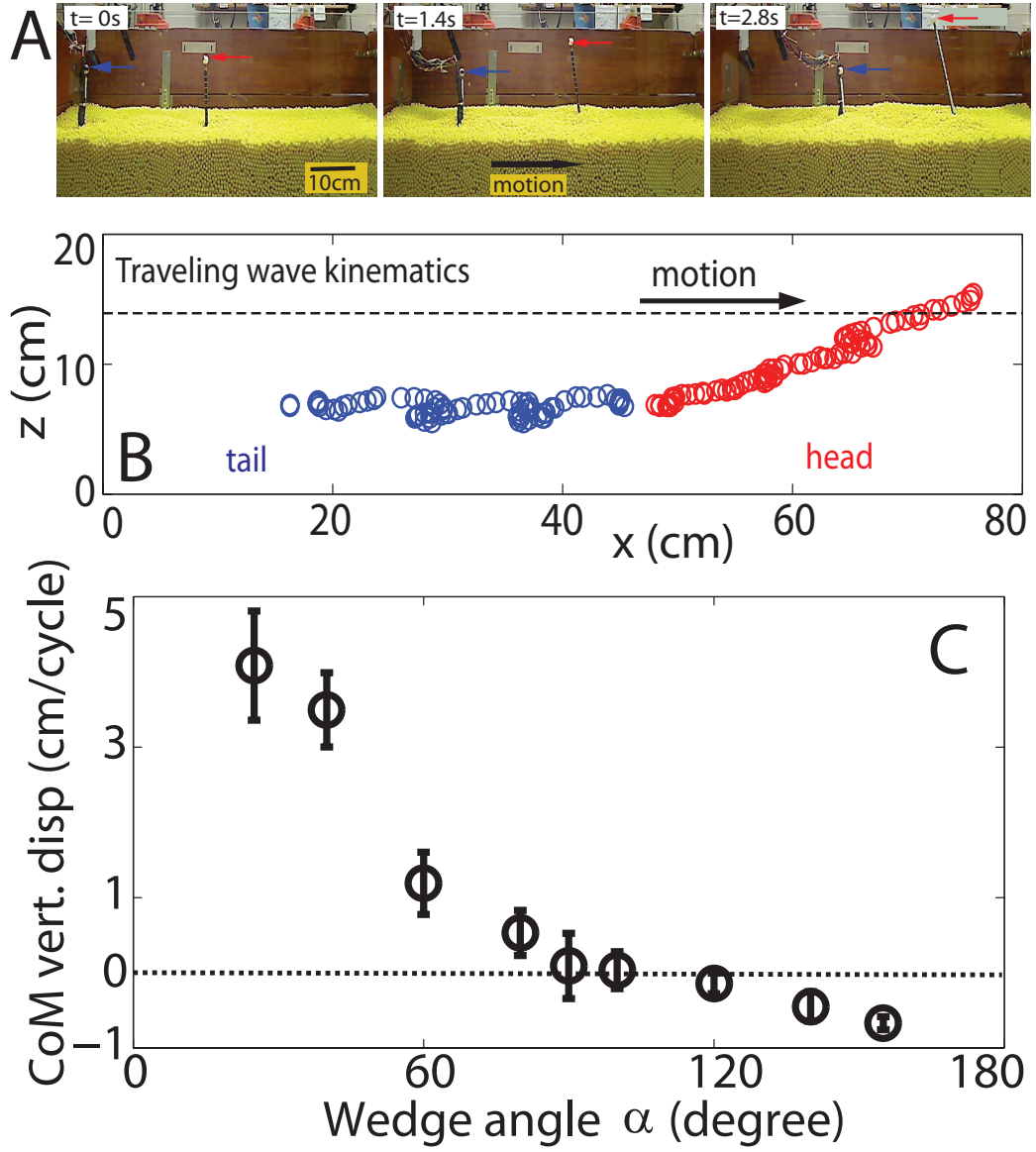
**Figure 51:** (A) Snapshots of the robot moving in 6 mm plastic spheres in vertical plane. The red and blue arrows point to the the two masts installed on the head and tail, respectively. (B) Trajectories of the head and tail masts from a representative run with wedge angle $\alpha = 90°$. (C) Average vertical displacement of the CoM per cycle as a function of head angle α. Average value and standard deviation are from 3 runs.

CHAPTER V

CONCLUSIONS AND FUTURE DIRECTIONS

In this dissertation, I described the study of subsurface locomotion and resistive forces on submerged intruders in granular media using numerical (DEM) and theoretical (RFT) models. These models, together with the physical model (robot) and biology experiments, explained the swimming speed within different materials and the stereotyped kinematics used by the sandfish lizard. The models revealed that the sandfish swims in a frictional fluid in which inertial effects are small, and that the swimming speed is determined by the balance of thrust and drag force from granular media. The models revealed how the resistive forces in granular media affect the sand-swimming performance and detailed mechanics of the sandfish. We found that the animal swims with an amplitude and number of period close to those that maximize the swimming speed. The models also generated biological hypotheses for locomotive constraints such as energy consumption and torque required from back muscles. These results aided the design of a 7-segment sand-swimming robot, and the robot in turn validated predictions of the models. Finally, I showed drag induced lift on an intruder in granular media was sensitive to the intruder shape. We deduced the lift forces on plates at varied inclination angle from the force balance on the flowing media near the plate and explained the force on a non-planar intruder as the sum of contributions from flat-plate elements of the intruder. Using the robot, we showed the drag induced lift force plays an important role in controlling the vertical motion of the robot and predicted that the head shape of the sandfish can facilitate the burrowing by generating negative lift with reduced head drag.

The animal models described in this dissertation provide a framework to develop and test hypotheses that address some central questions about the interactions between organisms and granular media, such as how the physics of granular media affects the kinematics and morphological adaptation of the organisms. The resistive forces and locomotion models in

granular media can provide guidance of the development and control strategy of robots or vehicles to enable effective locomotion within/on granular media. The resistive forces on rods observed in simple drag experiments, and the corresponding flow field and the force balance model may help the development of more accurate continuum models as well as serve as test cases. The model for the lift force on submerged intruders moving horizontally is an extension to the Coulomb wedge method and may be further developed to solve the resistive forces on intruders with different shapes and moving in arbitrary directions. The principles we learned for resistive forces may shed some light on the understanding of other phenomena in granular media. For example, the resistive forces may play an important role in the segregation of granular materials during avalanches as the larger particles might be considered as intruders. In the rest of this chapter, we discuss some questions that have arisen from our studies.

5.1 The models

In simulation, we focused on swimming in the horizontal plane; however, side-view x-ray video revealed that the animal swam at an angle between 20° and 30° to the horizontal. Simulating animal/robot motion out of the plane requires a 3D simulation. The multi-body software, Working Model, can only model 2D space and objects. 3D multi-body software (e.g. MBdyn) may replace Working Model so that the motion in the vertical direction can be modeled. Using 3D models, we may answer questions such as why the animal chose entry angles between 20° and 30°. The complex 3D geometry of the animal was not considered either. Although body geometries such as tapering on the head and tail were considered, we ignored the variation in the height of the sandfish body. To accurately and efficiently model the shape of the sandfish and other animal/robot/intruders with complex shapes, a more systematic method such the mesh grid method ([22]) and/or specialized software such as CAD tools might be necessary.

The animal motion is a result of the interaction among neuromechanical control and the external forces, muscle forces and (usually) flexible bodies. In our sandfish simulation, we controlled the deformation of the body (position in the body frame) without response

to external forces. Using different control strategies (e.g. control force or torque instead of position or angle) in the animal model and including body stiffness may lead to better understanding of the neuromechanical control of the animal. Study of different control strategies and body configuration of the swimmer may also provide solutions for a robot made of flexible material and other type of actuators (e.g. hydraulic and pneumatic actuators).

In the force model which described the lift force, we were able to calculate the force on a plate from the flow obtained from simulation in a quasi-2D scenario (rod cross section was much smaller than its length). This simulation-assisted force balance model may be extended to solve the forces on a rod in horizontal plane. However, the extension is not trivial, because the flow is in 3D and the slip planes are likely more complicated than the approximately flat planes observed in the 2D case. As shown in Chapter III, the resistive forces in granular media are affected by previous disturbance of the intruder, which is exemplified by the reduced thrust in the sandfish simulation. The history dependent effects need to be considered to accurately predict the forces on intruders and hence the locomotion performance of animals/robots interacting with granular media.

5.2 *Animal and robot experiment*

The simulation showed that the actuator power near the head and tail is nearly zero, which implies that it is possible to generate the same or nearly the same kinematics with passive element (e.g. tendons) near the two ends. Further study of the animal anatomy is required to determine if such elements exist and give insight into their properties. For robot design, adding passive elements such as springs, using a flexible body with tuned stiffness, or replacing the actuators with springs may result in a simpler design and simplify control in terms of fewer actuators. Such additions could also improve locomotion ability, and/or distribute the load of the actuators more evenly. The models also make prediction about energy consumption, which might be measured experimentally on the animal and the robot.

Robot experiments with a fixed head shape and a preliminary study of a robot with adjustable head orientation have shown that the head shape can be used to control the vertical motion. However, the mechanism by which the sandfish controls its vertical motion

is not clear due to difficulties in visualizing the head motion of the animal experimentally: since the lift force is very sensitive to the intruder orientation when the bottom surface is parallel to the direction of motion, head motion might be challenging to detect from high speed x-ray video alone. Another difficulty is recording the upward motion of the animal. The long time (many hours) that the animal can remain subsurface complicates x-ray data collection because of time limitations of the x-ray system..

5.3   Other modes of locomotion in granular media

Like swimming in fluids, animals may also use different modes for locomotion in granular media. Because of the existence of a finite yield stress, thrust can be obtained with nearly no deformation of the media. Our preliminary experiment using high speed x-ray imaging on another reptile, the ocellated skink (*Chalcides ocellatus*), showed that the body of the animal followed the trajectory of the head with little deformation of the media near the body*. This indicates that the yield stress was not reached for the media near the body but thrust was still generated. In our sandfish study, the speed of the intruder/locomoter was small such that the inertial forces could be neglected. Modes of subsurface locomotion that in the inertial regime of the granular media might also have biological relevance and application. For example, the Mojave fringe-toed lizard (*Uma scoparia*) uses small but high frequency (up to 21 Hz) oscillations to burrow into sand [66].

---

*The experiment was done by Sarah Sharpe, a bioengineering graduate student in the Goldman group.

REFERENCES

[1] http://www.engineeringtoolbox.com/young-modulus-d_417.html. [Online; accessed 7-November-2011].

[2] ALBERT, I., SAMPLE, J., MORSS, A., RAJAGOPALAN, S., BARABÁSI, A., and SCHIFFER, P., "Granular drag on a discrete object: Shape effects on jamming," *Physical Review E*, vol. 64, no. 6, p. 61303, 2001.

[3] ALBERT, R., PFEIFER, M. A., BARABASI, A. L., and SCHIFFER, P., "Slow drag in a granular medium," *Physical Review Letters*, vol. 82, no. 1, pp. 205–208, 1999.

[4] ALEXANDER, R. M., *Principles of Animal Locomotion*. Princeton University Press, 2003.

[5] ALEXANDER, R., *Principles of animal locomotion*. Princeton Univ Pr, 2003.

[6] ARENA, P., DI GIAMBERARDINO, P., FORTUNA, L., LA GALA, F., MONACO, S., MUSCATO, G., RIZZO, A., and RONCHINI, R., "Toward a mobile autonomous robotic system for Mars exploration," *Planetary and Space Science*, vol. 52, no. 1-3, pp. 23–30, 2004.

[7] ARNOLD, E., "Identifying the effects of history on adaptation: origins of different sand-diving techniques in lizards," *Journal of Zoology*, vol. 235, no. 3, pp. 351–388, 1995.

[8] ASHCHEULOV, A., GUTSUL, I., and MAEVSKI, V., "Device for monitoring the radiation temperature in coal mines," *Journal of Optical Technology*, vol. 67, no. 3, p. 281, 2000.

[9] AVRON, J., GAT, O., and KENNETH, O., "Optimal swimming at low reynolds numbers," *Physical Review Letters*, vol. 93, no. 18, p. 186001, 2004.

[10] BAUMGARTNER, W., FIDLER, F., WETH, A., HABBECKE, M., JAKOB, P., BUTENWEG, C., and BÖHME, W., "Investigating the locomotion of the sandfish in desert sand using nmr-imaging," *PLoS ONE*, vol. 3, no. 10, pp. e3309:1–10, 2008.

[11] BAUMGARTNER, W., SAXE, F., WETH, A., HAJAS, D., SIGUMONRONG, D., EMMERLICH, J., SINGHEISER, M., BOEHME, W., and SCHNEIDER, J., "The Sandfish's Skin: Morphology, Chemistry and Reconstruction," *Journal of Bionic Engineering*, vol. 4, no. 1, pp. 1–9, 2007.

[12] BEJAN, A. and MARDEN, J., "Unifying constructal theory for scale effects in running, swimming and flying," *Journal of Experimental Biology*, vol. 209, no. 2, p. 238, 2006.

[13] BIEWENER, A., "Biomechanics of mammalian terrestrial locomotion," *Science*, vol. 250, no. 4984, p. 1097, 1990.

[14] BREED, C., GROLIER, M., and McCAULEY, J., "Morphology and distribution of common sanddunes on mars: comparison with the earth," *Journal of Geophysical Research*, vol. 84, no. B14, pp. 8183–8204, 1979.

[15] CAMPBELL, C., "Rapid granular flows," *Annual Review of Fluid Mechanics*, vol. 22, no. 1, pp. 57–90, 1990.

[16] CARLING, J., WILLIAMS, T., and BOWTELL, G., "Self-propelled anguilliform swimming: simultaneous solution of the two-dimensional navier-stokes equations and newton's laws of motion," *Journal of Experimental Biology*, vol. 201, pp. 3143–3166, 1998.

[17] CHEHATA, D., ZENIT, R., and WASSGREN, C., "Dense granular flow around an immersed cylinder," *Physics of Fluids*, vol. 15, p. 1622, 2003.

[18] CHEN, J., FRIESEN, W., and IWASAKI, T., "Mechanisms underlying rhythmic locomotion: body–fluid interaction in undulatory swimming," *Journal of Experimental Biology*, vol. 214, no. 4, p. 561, 2011.

[19] CHIRIKJIAN, G. and BURDICK, J., "The kinematics of hyper-redundant robot locomotion," *IEEE Transactions on Robotics and Automation*, vol. 11, no. 6, pp. 781–793, 1995.

[20] CHOSET, H., LUNTZ, J., SHAMMAS, E., RACHED, T., HULL, D., and DENT, C., "Design and motion planning for serpentine robots," in *Proceedings of SPIE*, vol. 3990, p. 148, 2000.

[21] CIAMARRA, M. P., LARA, A. H., LEE, A. T., GOLDMAN, D. I., VISHIK, I., and SWINNEY, H. L., "Dynamics of drag and force distributions for projectile impact in a granular medium," *Phys. Rev. Lett*, vol. 92, p. 194301, 2004.

[22] Citeseer, *A survey of unstructured mesh generation technology*, vol. 3, 1998.

[23] COHEN, N. and BOYLE, J., "Swimming at low reynolds number: a beginners guide to undulatory locomotion," *Contemporary Physics*, vol. 51, no. 2, pp. 103–123, 2010.

[24] CONIGLIO, A. and NICODEMI, M., "A statistical mechanics approach to the inherent states of granular media," *Physica A: Statistical Mechanics and its Applications*, vol. 296, no. 3-4, pp. 451–459, 2001.

[25] CRESPI, A., BADERTSCHER, A., GUIGNARD, A., and IJSPEERT, A., "Swimming and crawling with an amphibious snake robot," in *IEEE International Conference on Robotics and Automation*, vol. 3, p. 3024, Citeseer, 2005.

[26] CRESPI, A. and IJSPEERT, A., "Online optimization of swimming and crawling in an amphibious snake robot," *IEEE Transactions on Robotics*, vol. 24, no. 1, pp. 75–87, 2008.

[27] DABIRI, J., COLIN, S., COSTELLO, J., and GHARIB, M., "Flow patterns generated by oblate medusan jellyfish: field measurements and laboratory analyses," *Journal of experimental biology*, vol. 208, no. 7, p. 1257, 2005.

[28] DARWIN, C., *The Formation of Vegetable Mould, Through the Action of Worms: with Observations on Their Habits*. D. Appleton & Company, 1882.

[29] DESAI, R., ROSENBERG, C., JONES, J., and INC, I., "Kaa: an autonomous serpentine robot utilizes behavior control," in *Proceedings of the 1995 International Conference on Intelligent Robots and Systems, Pittsburgh*, Citeseer, 1995.

[30] DICKINSON, M. and GOTZ, K., "Unsteady aerodynamic performance of model wings at low reynolds numbers," *Journal of Experimental Biology*, vol. 174, no. 1, p. 45, 1993.

[31] DICKINSON, W. W. and WARD, J. D., "Low depositional porosity in eolian sands and sandstones, namib desert," *Journal of Sedimentary Research Section A–Sedimentary Petrology and Processes*, vol. 64, no. 2, pp. 226–232, 1994.

[32] DING, Y., GRAVISH, N., and GOLDMAN, D., "Drag induced lift in granular media," *Physical Review Letters*, vol. 106, no. 2, p. 28001, 2011.

[33] DIPPEL, S. and WOLF, D., "Force schemes in simulations of granular materials," *Journal de physique I*, vol. 6, no. 1, pp. 5–20, 1996.

[34] DORGAN, K., ARWADE, S., and JUMARS, P., "Burrowing in marine muds by crack propagation: kinematics and forces," *Journal of Experimental Biology*, vol. 210, no. 23, p. 4198, 2007.

[35] DOWLING, K., "Limbless locomotion: learning to crawl," in *1999 IEEE International Conference on Robotics and Automation, 1999. Proceedings*, vol. 4, 1999.

[36] DOWLING, K., *Limbless locomotion: learning to crawl with a snake robot*. PhD thesis, Citeseer, 1996.

[37] DRUCKER, E. and LAUDER, G., "Locomotor forces on a swimming fish: three-dimensional vortex wake dynamics quantified using digital particle image velocimetry," *Journal of Experimental Biology*, vol. 202, no. 18, p. 2393, 1999.

[38] DURAN, J., *Sands, powders, and grains*. Springer, 2000.

[39] ELDREDGE, J., "Numerical simulations of undulatory swimming at moderate Reynolds number," *Bioinspiration & Biomimetics*, vol. 1, pp. S19–S24, 2006.

[40] ELLINGTON, C., "The novel aerodynamics of insect flight: applications to micro-air vehicles," *Journal of Experimental Biology*, vol. 202, no. 23, pp. 3439–3448, 1999.

[41] EZCURRA, E., *Global Deserts Outlook*. United Nations Educational, 2006.

[42] FISCHER-CRIPPS, A., *Introduction to contact mechanics*. Springer Verlag, 2000.

[43] FONTAINE, E., ZABALA, F., DICKINSON, M., and BURDICK, J., "Wing and body motion during flight initiation in Drosophila revealed by automated visual tracking," *Journal of Experimental Biology*, vol. 212, no. 9, p. 1307, 2009.

[44] FORTERRE, Y. and POULIQUEN, O., "Flows of dense granular media," *Annual Review of Fluid Mechanics*, vol. 40, pp. 1–24, 2008.

[45] GIDMARK, N., STROTHER, J., HORTON, J., SUMMERS, A., and BRAINERD, E., "Locomotory transition from water to sand and its effects on undulatory kinematics in sand lances (ammodytidae)," *Journal of Experimental Biology*, vol. 214, no. 4, p. 657, 2011.

[46] GILLIS, G., "Undulatory locomotion in elongate aquatic vertebrates: Anguilliform swimming since Sir James Gray," *Integrative and Comparative Biology*, vol. 36, no. 6, p. 656, 1996.

[47] GILLIS, G., "Neuromuscular control of anguilliform locomotion: patterns of red and white muscle activity during swimming in the american eel anguilla rostrata," *Journal of Experimental Biology*, vol. 201, pp. 3245–3256, 1998.

[48] GOLDMAN, D. and UMBANHOWAR, P., "Scaling and dynamics of sphere and disk impact into granular media," *Physical Review E*, vol. 77, no. 2, p. 21308, 2008.

[49] GOLDMAN, R. M., DING, Y., UMBANHOWAR, P., KAMOR, A., and D., "Biophysically inspired development of a sand-swimming robot," in *Proceedings of Robotics: Science and Systems*, (Zaragoza, Spain), June 2010.

[50] GOMBOSI, T., *Gaskinetic Theory.* Cambridge University Press, 1994.

[51] GRAVISH, N., UMBANHOWAR, P., and GOLDMAN, D., "Force and flow transition in plowed granular media," *Physical Review Letters*, vol. 105, no. 12, p. 128301, 2010.

[52] GRAY, J. and HANCOCK, G., "The propulsion of sea-urchin spermatozoa," *Journal of Experimental Biology*, vol. 32, no. 4, p. 802, 1955.

[53] GRAY, J. and LISSMANN, H., "The locomotion of nematodes," *Journal of Experimental Biology*, vol. 41, no. 1, p. 135, 1964.

[54] GUO, Z. and MAHADEVAN, L., "Limbless undulatory propulsion on land," *Proceedings of the National Academy of Sciences*, vol. 105, no. 9, p. 3179, 2008.

[55] HEDENSTROM, A., VAN GRIETHUIJSEN, L., ROSÉN, M., and SPEDDING, G., "Vortex wakes of birds: recent developments using digital particle image velocimetry in a wind tunnel," *Animal Biology*, vol. 56, no. 4, pp. 535–549, 2006.

[56] HEIKEN, G., VANIMAN, D., and FRENCH, B., *Lunar sourcebook: a user's guide to the moon.* Cambridge Univ Pr, 1991.

[57] HIROSE, S. and MORISHIMA, A., "Design and control of a mobile robot with an articulated body," *The International Journal of Robotics Research*, vol. 9, no. 2, p. 99, 1990.

[58] HOLMES, P., FULL, R. J., KODITSCHEK, D., and GUCKENHEIMER, J., "The dynamics of legged locomotion: Models, analyses, and challenges," *Siam Review*, vol. 48, no. 2, pp. 207–304, 2006.

[59] HOOVER, A. M., STELTZ, E., and FEARING, R. S., "Roach: An autonomous 2.4 g crawling hexapod robot," 2008.

[60] HU, D., CHAN, B., and BUSH, J., "The hydrodynamics of water strider locomotion," *Nature*, vol. 424, no. 6949, pp. 663–666, 2003.

[61] HU, D., NIRODY, J., SCOTT, T., and SHELLEY, M., "The mechanics of slithering locomotion," *Proceedings of the National Academy of Sciences*, vol. 106, no. 25, p. 10081, 2009.

[62] HUANG, N., OVARLEZ, G., BERTRAND, F., RODTS, S., COUSSOT, P., and BONN, D., "Flow of wet granular materials," *Physical Review Letters*, vol. 94, no. 2, p. 28301, 2005.

[63] HUMPHREY, C. and ADAMS, J., "Robotic Tasks for Chemical, Biological, Radiological, Nuclear and Explosive Incident Response," *Advanced Robotics*, vol. 23, no. 9, pp. 1217–1232, 2009.

[64] JACKSON, R., *The dynamics of fluidized particles*. Cambridge Univ Pr, 2000.

[65] JAEGER, H. M., NAGEL, S. R., and BEHRINGER, R. P., "Granular solids, liquids, and gases," *Reviews of Modern Physics*, vol. 68, no. 4, pp. 1259–1273, 1996.

[66] JAYNE, B. and DAGGY, M., "The effects of temperature on the burial performance and axial motor pattern of the sand-swimming of the mojave fringe-toed lizard uma scoparia," *Journal of Experimental Biology*, vol. 203, no. 7, p. 1241, 2000.

[67] JAYNE, B. and LAUDER, G., "Speed effects on midline kinematics during steady undulatory swimming of largemouth bass, micropterus salmoides," *Journal of Experimental Biology*, vol. 198, pp. 585–585, 1995.

[68] KATO, N. and KAMIMURA, S., *Bio-mechanisms of swimming and flying: fluid dynamics, biomimetic robots, and sports science*. Springer Verlag, 2007.

[69] KIM, S., CLARK, J. E., and CUTKOSKY, M. R., "isprawl: Design and tuning for high-speed autonomous open-loop running," *International Journal of Robotics Research*, vol. 25, no. 9, 2006.

[70] KLAASSEN, B. and PAAP, K., "GMD-SNAKE 2: a snake-like robot driven by wheels and a method for motion control," in *Proceedings of the IEEE International Conference on Robotics and Automation*, vol. 4, pp. 3014–3019, 1999.

[71] KRUGGEL-EMDEN, H., SIMSEK, E., RICKELT, S., WIRTZ, S., and SCHERER, V., "Review and extension of normal force models for the discrete element method," *Powder Technology*, vol. 171, no. 3, pp. 157–173, 2007.

[72] LAUDER, G. and DRUCKER, E., "Forces, Fishes, and Fluids: Hydrodynamic Mechanisms of Aquatic Locomotion," *Physiology*, vol. 17, no. 6, pp. 235–240, 2002.

[73] LEE, J. and HERRMANN, H., "Angle of repose and angle of marginal stability: molecular dynamics of granular particles," *Journal of Physics A: Mathematical and General*, vol. 26, pp. 373–383, 1993.

[74] LEHMANN, F., "Aerial locomotion in flies and robots: kinematic control and aerodynamics of oscillating wings," *Arthropod Structure & Development*, vol. 33, no. 3, pp. 331–345, 2004.

[75] LI, C., UMBANHOWAR, P., KOMSUOGLU, H., KODITSCHEK, D., and GOLDMAN, D., "Sensitive dependence of the motion of a legged robot on granular media," *Proceedings of the National Academy of Sciences*, vol. 106, no. 9, p. 3029, 2009.

[76] LI, C., UMBANHOWAR, P. B., KOMSUOGLU, H., and GOLDMAN, D. I., "The effect of limb kinematics on the speed of a legged robot on granular media," *Journal of Experimental Mechanics, in review*, 2010.

[77] Lighthill, M., "Large-amplitude elongated-body theory of fish locomotion," *Proceedings of the Royal Society of London. Series B, Biological Sciences*, vol. 179, no. 1055, pp. 125–138, 1971.

[78] Liu, H. and Kawachi, K., "A numerical study of undulatory swimming," *Journal of Computational Physics*, vol. 155, no. 2, pp. 223–247, 1999.

[79] Long, J., "Muscles, elastic energy, and the dynamics of body stiffness in swimming eels," *American zoologist*, vol. 38, no. 4, p. 771, 1998.

[80] Long, J. and others, "Force transmission via axial tendons in undulating fish: a dynamic analysis* 1," *Comparative Biochemistry and Physiology-Part A: Molecular & Integrative Physiology*, vol. 133, no. 4, pp. 911–929, 2002.

[81] Maladen, R., Ding, Y., Li, C., and Goldman, D., "Undulatory Swimming in Sand: Subsurface Locomotion of the Sandfish Lizard," *Science*, vol. 325, no. 5938, p. 314, 2009.

[82] Maladen, R., Ding, Y., Umbanhowar, P., and Goldman, D., "Undulatory swimming in sand: experimental and simulation studies of a robotic sandfish," *The International Journal of Robotics Research*, vol. 30, no. 7, p. 793, 2011.

[83] Maladen, R., Ding, Y., Umbanhowar, P., and Goldman, D., "Undulatory swimming in sand: experimental and simulation studies of a robotic sandfish.," *International Journal of Robotics Research*, in review.

[84] Maladen, R., Ding, Y., Umbanhowar, P., Kamor, A., and Goldman, D., "Mechanical models of sandfish locomotion reveal principles of high performance subsurface sand-swimming," *Journal of The Royal Society Interface*, vol. 8, pp. 1332–1345, 2011.

[85] Marcus, W., Legleiter, C., Aspinall, R., Boardman, J., and Crabtree, R., "High spatial resolution hyperspectral mapping of in-stream habitats, depths, and woody debris in mountain streams," *Geomorphology*, vol. 55, no. 1-4, pp. 363–380, 2003.

[86] Metternicht, G., Hurni, L., and Gogu, R., "Remote sensing of landslides: An analysis of the potential contribution to geo-spatial systems for hazard assessment in mountainous environments," *Remote Sensing of Environment*, vol. 98, no. 2-3, pp. 284–303, 2005.

[87] Meysman, F., Middelburg, J., and Heip, C., "Bioturbation: a fresh look at Darwin's last idea," *Trends in Ecology & Evolution*, vol. 21, no. 12, pp. 688–695, 2006.

[88] Mittal, R., Dong, H., Bozkurttas, M., Lauder, G., and Madden, P., "Locomotion with flexible propulsors: II. Computational modeling of pectoral fin swimming in sunfish," *Bioinspiration & Biomimetics*, vol. 1, p. S35, 2006.

[89] Miyamoto, H., Yano, H., Scheeres, D., Abe, S., Barnouin-Jha, O., Cheng, A., Demura, H., Gaskell, R., Hirata, N., Ishiguro, M., and others, "Regolith migration and sorting on asteroid itokawa," *Science*, vol. 316, no. 5827, p. 1011, 2007.

[90] MOSAUER, W., "Adaptive convergence in the sand reptiles of the Sahara and of California: a study in structure and behavior," *Copeia*, pp. 72–78, 1932.

[91] NAUEN, J. and LAUDER, G., "Quantification of the wake of rainbow trout (Oncorhynchus mykiss) using three-dimensional stereoscopic digital particle image velocimetry," *Journal of Experimental Biology*, vol. 205, no. 21, p. 3271, 2002.

[92] NEDDERMAN, R., *Statics and kinematics of granular materials*. Cambridge Univ Pr, 1992.

[93] NELSON, E., KATSURAGI, H., MAYOR, P., and DURIAN, D., "Projectile interactions in granular impact cratering," *Physical Review Letters*, vol. 101, no. 6, p. 68001, 2008.

[94] NORRIS, K. and KAVANAU, J., "The burrowing of the western shovel-nosed snake, Chionactis occipitalis Hallowell, and the undersand environment," *Copeia*, vol. 1966, no. 4, pp. 650–664, 1966.

[95] O'HERN, C., LANGER, S., LIU, A., and NAGEL, S., "Random packings of frictionless particles," *Physical Review Letters*, vol. 88, no. 7, p. 75507, 2002.

[96] ONWUALU, A. and WATTS, K., "Draught and vertical forces obtained from dynamic soil cutting by plane tillage tools," *Soil and Tillage Research*, vol. 48, no. 4, pp. 239–253, 1998.

[97] PANAITESCU, A. and KUDROLLI, A., "Experimental investigation of cyclically sheared granular particles with direct particle tracking," *Progress of Theoretical Physics Supplement*, p. 1, 2009.

[98] PFEIFER, R., LUNGARELLA, M., and IIDA, F., "Self-organization, embodiment, and biologically inspired robotics," *Science*, vol. 318, no. 5853, p. 1088, 2007.

[99] PLAYTER, R., BUEHLER, M., and RAIBERT, M., "Bigdog," in *Unmanned Ground Vehicle Technology VIII* (GRANT R. GERHART, CHARLES M. SHOEMAKER, D. W. G., ed.), vol. 6230 of *Proceedings of SPIE*, pp. 62302O1–62302O6, 2006.

[100] RAPAPORT, D. C., *The art of molecular dynamics simulation*. Cambridge University Press, 2nd ed., 2004.

[101] RAPAPORT, D., *The art of molecular dynamics simulation*. Cambridge Univ Pr, 2004.

[102] RICHARD, P., NICODEMI, M., DELANNAY, R., RIBIÈRE, P., and BIDEAU, D., "Slow relaxation and compaction of granular systems," *Nature Materials*, vol. 4, no. 2, pp. 121–128, 2005.

[103] RITZMANN, R., QUINN, R., and FISCHER, M., "Convergent evolution and locomotion through complex terrain by insects, vertebrates and robots," *Arthropod structure and development*, vol. 33, no. 3, pp. 361–379, 2004.

[104] ROSATO, A., STRANDBURG, K., PRINZ, F., and SWENDSEN, R., "Why the Brazil nuts are on top: Size segregation of particulate matter by shaking," *Physical Review Letters*, vol. 58, no. 10, pp. 1038–1040, 1987.

[105] SARANLI, U., BUEHLER, M., and KODITSCHEK, D., "Rhex: A simple and highly mobile hexapod robot," *The International Journal of Robotics Research*, vol. 20, no. 7, p. 616, 2001.

[106] SAUNDERS, A., GOLDMAN, D. I., FULL, R. J., and BUEHLER, M., "The rise climbing robot: body and leg design," in *Unmanned Systems Technology VIII* (GERHART, G. R., SHOEMAKER, C. M., and GAGE, D. W., eds.), vol. 6230, p. 623017, SPIE, 2006.

[107] SCHRÖTER, M., GOLDMAN, D., and SWINNEY, H., "Stationary state volume fluctuations in a granular medium," *Physical Review E*, vol. 71, no. 3, p. 030301, 2005.

[108] SCHRÖTER, M., NÄGLE, S., RADIN, C., and SWINNEY, H., "Phase transition in a static granular system," *Europhysics Letters*, vol. 78, p. 44004, 2007.

[109] SHAN, Y. and KOREN, Y., "Obstacle accommodation motion planning," in *Intelligent autonomous systems, IAS–3: proceedings of the international conference, Pittsburgh, Pennsylvania, February 15-18, 1993*, p. 94, Ios Pr Inc, 1993.

[110] SHARPE, S. S., DING, Y., and GOLDMAN, D. I., "Interaction with granular media influences muscle activation strategy during sand-swimming," *The Journal of Experimental Biology (In Prep)*, 2011.

[111] SHIMADA, T., KADAU, D., SHINBROT, T., and HERRMANN, H., "Swimming in granular media," *Physical Review E*, vol. 80, no. 2, p. 20301, 2009.

[112] SHYY, W., AONO, H., CHIMAKURTHI, S., TRIZILA, P., KANG, C., CESNIK, C., and LIU, H., "Recent progress in flapping wing aerodynamics and aeroelasticity," *Progress in Aerospace Sciences*, vol. 46, no. 7, pp. 284–327, 2010.

[113] SIEGWART, R., LAMON, P., ESTIER, T., LAURIA, M., and PIGUET, R., "Innovative design for wheeled locomotion in rough terrain," *Robotics and Autonomous systems*, vol. 40, no. 2-3, pp. 151–162, 2002.

[114] SOLLER, R. and KOEHLER, S., "Drag and lift on rotating vanes in granular beds," *Physical Review E*, vol. 74, no. 2, p. 21305, 2006.

[115] SQUYRES, S., ARVIDSON, R., BOLLEN, D., BELL III, J., BRÜCKNER, J., CABROL, N., CALVIN, W., CARR, M., CHRISTENSEN, P., CLARK, B., and OTHERS, "Overview of the opportunity mars exploration rover mission to meridiani planum: Eagle crater to purgatory ripple," *J. Geophys. Res*, vol. 111, 2006.

[116] STEEVES III, C., *Design and behavioural control of a dynamic quadruped with active wheels*. PhD thesis, Citeseer, 2002.

[117] SWOAP, S., JOHNSON, T., JOSEPHSON, R., and BENNETT, A., "Temperature, muscle power output and limitations on burst locomotor performance of the lizard dipsosaurus dorsalis," *Journal of Experimental Biology*, vol. 174, no. 1, p. 185, 1993.

[118] TAYLOR, G., "The action of waving cylindrical tails in propelling microscopic organisms," *Proceedings of the Royal Society of London. Series A. Mathematical and Physical Sciences*, vol. 211, no. 1105, p. 225, 1952.

[119] TIAN, Y., PESIKA, N., ZENG, H., ROSENBERG, K., ZHAO, B., MCGUIGGAN, P., AUTUMN, K., and ISRAELACHVILI, J., "Adhesion and friction in gecko toe attachment and detachment," *Proceedings of the National Academy of Sciences*, vol. 103, no. 51, p. 19320, 2006.

[120] TOIYA, M., STAMBAUGH, J., and LOSERT, W., "Transient and oscillatory granular shear flow," *Physical Review Letters*, vol. 93, no. 8, p. 88001, 2004.

[121] TYTELL, E. D. and LAUDER, G. V., "The hydrodynamics of eel swimming - i. wake structure," *Journal of Experimental Biology*, vol. 207, no. 11, pp. 1825–1841, 2004.

[122] TYTELL, E., HSU, C., WILLIAMS, T., COHEN, A., and FAUCI, L., "Interactions between internal forces, body stiffness, and fluid environment in a neuromechanical model of lamprey swimming," *Proceedings of the National Academy of Sciences*, vol. 107, no. 46, p. 19832, 2010.

[123] VOGEL, S., *Life in moving fluids: the physical biology of flow.* Princeton University Press, 1996.

[124] WHITE, C., "The energetics of burrow excavation by the inland robust scorpion, Urodacus yaschenkoi (Birula, 1903)," *Australian Journal of Zoology*, vol. 49, no. 6, pp. 663–674, 2001.

[125] WIEGHARDT, K., "Forces in granular flow," *Mechanics Research Communications*, vol. 1, no. 1, pp. 3–7, 1974.

[126] WIEGHARDT, K., "Experiments in granular flow," *Annual Review of Fluid Mechanics*, vol. 7, no. 1, pp. 89–114, 1975.

[127] WOLFGANG, M., ANDERSON, J., GROSENBAUGH, M., YUE, D., and TRIANTAFYLLOU, M., "Near-body flow dynamics in swimming fish," *Journal of Experimental Biology*, vol. 202, no. 17, p. 2303, 1999.

[128] WONG, J., "On the study of wheel-soil interaction," *Journal of Terramechanics*, vol. 21, no. 2, pp. 117–131, 1984.

VITA

Yang Ding was born and grew up in Beitun, Xinjiang, China. He attended Xinjiang Experimental High School at the capital Urumqi of Xinjiang. He went to Hefei in Anhui province and he got his Bachelor of physics degree in theoretical physics from the University of Science and Technology of China. In 2005, he was admitted to Georgia Institute of Technology, School of Physics as Phd student. Yang's research resulted in a several peer-reviewed publications including prestigious journal Science and Physical Review Letters and was also featured in the popular press. He was awarded the Amelio Fellowship for Excellence in Graduate Research in 2011.